3D Modeling and Inversion of Airborne Gravity Gradiometry and Aeromagnetic Data from Budgell Harbour, North-Central Newfoundland

by

© Onur Totoş

A thesis submitted to the School of Graduate
Studies in partial fulfillment of the requirements
for the degree of Master of Science

Department of Earth Sciences

Memorial University of Newfoundland

January 2021

St. John's, Newfoundland and Labrador

Abstract

Airborne gravity surveys have been become a popular tool for mineral exploration in the past three decades, mostly because of considerable improvements in equipment. Airborne methods make the data acquisition process rapid, more straightforward, and potentially cheaper than ground surveys. 3D modeling and inversion of gravity gradiometry and aeromagnetic datasets from Budgell Harbour, located in north-central Newfoundland, are carried out. Reef-type platinum group mineralization is present in the area, as well as a large scale, deep igneous intrusion (the Budgell Harbour Stock). The intrusion is thought to be related to the same tectonic activity that resulted in the formation of the basins off-shore Newfoundland that are now being actively explored for hydrocarbons. 3D modeling and inversion, specifically taking into account topography, are done for the gravity gradiometry and magnetic data-sets. The inversions are typical unconstrained, minimum-structure inversions. Joint inversion of the gravity gradiometry and magnetic data-sets is also considered. The Earth model is parameterized in terms of an unstructured tetrahedral mesh, which allows the topography to be modeled to the same accuracy with which it is known. The goal is to develop 3D density and susceptibility models of the area, thus further assessing the mineral potential of the area and better delineating the Budgell Harbour Stock.

General Summary

Geophysical science applies the principles of physics to the study of the Earth. Geophysical surveys of the Earth's interior involve making measurements, at or near the Earth's surface, of quantities such as gravity and magnetic field that are affected by the internal distribution of the physical properties of the rocks such as density and magnetic susceptibility. Analysis of these measurements helps to reveal how the physical properties of the Earth's interior change vertically and laterally. Geophysical exploration methods use measurements within geographically restricted areas to determine the distributions of physical properties at depths that reflect the local subsurface geology. Geophysical methods are usually used in combination. Two commonly used geophysical exploration methods, *gravity* and *magnetics,* are investigated in this project for the understanding of the subsurface of the Budgell Harbour property, located in north-central Newfoundland. The reasons that the Budgell Harbour area is studied are the exploration for ore deposits and the study of a large deep igneous intrusive feature in the area.

Acknowledgments

I would like to express my gratitude to my supervisor Prof. Colin G. Farquharson, for his advice, guidance, and encouragement throughout this project and the COVID-19 pandemic. I would also like to thank my committee member Dr. Charles Hurich for his advice and support. I am also grateful to Dr. Peter Lelièvre for access to his modeling programs, as well as his support.

I am also grateful to be part of Prof. Colin G. Farquharson's Research Group and would like to acknowledge everyone in this group who helped me throughout my research. Also, I would like to thank Mert Karanfil for his friendship and support since 2012.

I would like to acknowledge the Republic of Turkey Ministry of National Education for financial support, which enabled me to focus on thesis work and to thank the Republic of Turkey Toronto Education Attaché for their moral support, especially during the COVID-19 pandemic.

Finally, my deep and sincere gratitude to my family for their continuous and unparalleled love, help, and support.

Table of Contents

vii

List of Tables

List of Figures

1. Introduction

The Budgell Harbour area is located in north-central Newfoundland (Figures 1.1 and 1.2). Previous geological and geophysical studies in this area have indicated the potential for platinum group element mineralization in the area. Also, the area contains a large, deep intrusive feature thought to be associated with processes involved with the formation of the basins offshore Newfoundland. The purpose of this M.Sc. project is to model, invert and interpret airborne gravity gradiometry data and aeromagnetic data that have previously been collected in the Budgell Harbour area.
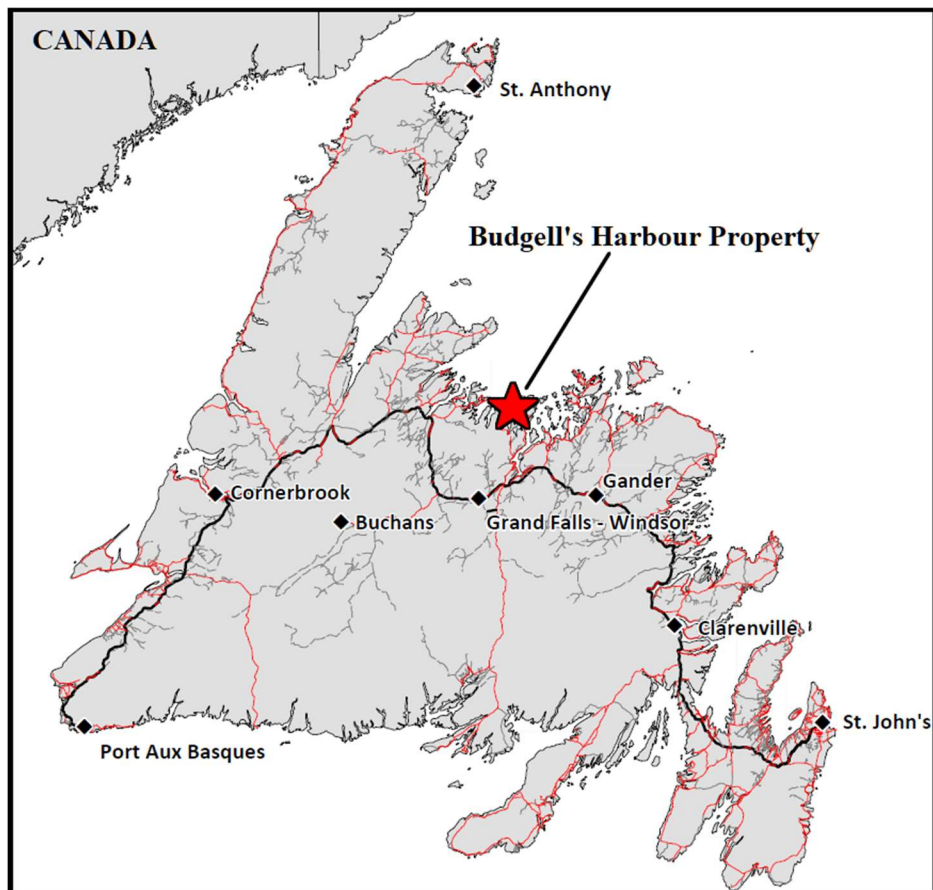
Figure 1.1 A map of the island of Newfoundland. The red star indicates the Budgell Harbour Property (modified from Stuckless, 2008).
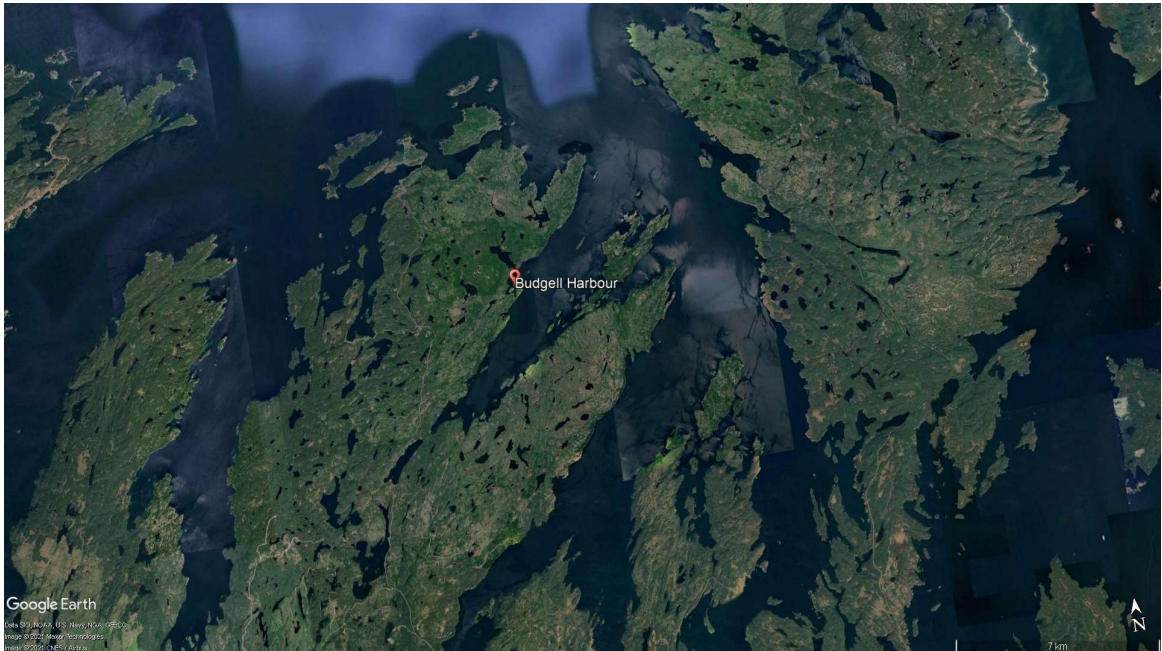
Figure 1.2: The local satellite image of the Budgell Harbour property (UTM zone 21N; modified from Google Earth, 2020).

Previous geological and geophysical surveys in the Budgell Harbour area have indicated that the Budgell Harbour property contains lamprophyre dykes and a deep gabbro intrusion known as Budgell Harbour Stock (Peace et al., 2018). Also, the susceptibility model for the Budgell Harbour Stock intrusion constructed by Miller (1976) suggests that its general shape is a vertical prism having a maximum depth of approximately 5.5 km to the bottom of the intrusion. Moreover, an airborne gravity gradiometry survey conducted in the area (the one considered in this thesis) also delineated strong, wide gravity anomalies over the Budgell Harbour Stock (Mataragio and Kieley, 2009).

Airborne gravity gradiometry and aeromagnetic surveys were conducted over the Budgell Harbour property in 2007 by Celtic Minerals Ltd. using the Bell Geospace Air Full Tensor

Gradiometry system. The advantage of using gravity gradiometry and magnetic methods is that these two methods can directly delineate the anomalies related to subsurface geology, such as gravity and magnetic anomalies in the given area, especially targeting the mineral potential and deeper igneous structures. An overview of principles of the gravity and magnetic methods, as well as a description of airborne gravity gradiometry and aeromagnetics, is presented in Chapter 3. The description of the techniques and measured quantities are given, along with historical reviews and recent developments.

Three-dimensional Earth modeling and inversion are described, including applications and background information in Chapter 4. The aim of developing 3D density and susceptibility models is explained as well as the use of unstructured meshes. The software packages used in this project for forward modeling and inversion are presented.

The real data-sets are analyzed and modeled three-dimensionally in terms of unstructured tetrahedral meshes. Also, a typical minimum structure inversion algorithm is applied in order to further assess the mineral potential and better delineate the Budgell Harbour Stock. The inversion results for airborne gravity gradiometry data and total magnetic field data are presented in Chapter 5. The comparison of inversion results for single-component data-sets and different combinations of gravity gradient tensor components, and how each one gives different information about the subsurface geology, are discussed.

The efficiency of using airborne total magnetic field data inversion for the interpretation is described in Chapter 6. Joint inversion of airborne gravity gradiometry data and total magnetic field data is also carried out for the area of interest. The inversion results are

highly consistent when compared with observed airborne gravity gradiometry and total magnetic field datasets.

A summary of this study is provided in Chapter 7. The significance of building a proper Earth model for the area of interest, particularly in terms of unstructured meshes, is given. The utility of each component of the airborne gravity gradient tensor and the inversion results are described. The benefit of inverting airborne total field magnetic data and how it can be useful for the interpretation of the subsurface geology are described. The advantages of inverting two different physical properties data-sets (joint inversion) over the study area are also considered.

2. Geological Setting of the Study Area: Budgell Harbour, North-Central Newfoundland

2.1 Regional geology

The island of Newfoundland forms the northern end of the Appalachian Orogen. The onshore geology of Newfoundland is shown in Figure 2.1. The geological subdivisions of the island are based on stratigraphic and structural contrasts related to the formation and later destruction of a late Precambrian terrain (Cooper et al., 2001). The Humber Zone is comprised of Paleozoic shelf facies units (sedimentary rocks) deposited on the crystalline Precambrian (Grenville) basement. The Humber Zone records multiphase deformation of the Cambrian–Ordovician passive margin and the Ordovician to Devonian foreland basins by the Taconian, Salinian, and Acadian orogenic events.

The Dunnage Zone, in which the Budgell Harbour is located, is represented by the Ordovician ophiolitic and arc complexes that are formed outside of the Laurentian Margin. The boundary between the Humber and Dunnage zones, the Baie Verte Line, corresponds to a long-lived and composite fault zone (Castonguay et al., 2009). The Gander zone is formed mainly from deep-water sedimentary rocks deposited in the eastern part of the Paleozoic Ocean. The southeastern margin of the Gander zone is in tectonic contact with the Avalon zone, which has a Gondwanan affinity and preserves a subduction zone stratigraphy (Schofield and D'Lemos, 2000). The Avalon Zone comprises early Paleozoic platform sedimentary rocks that form part of the European continent, late Precambrian volcanic, and plutonic rocks (Evans, 1996).
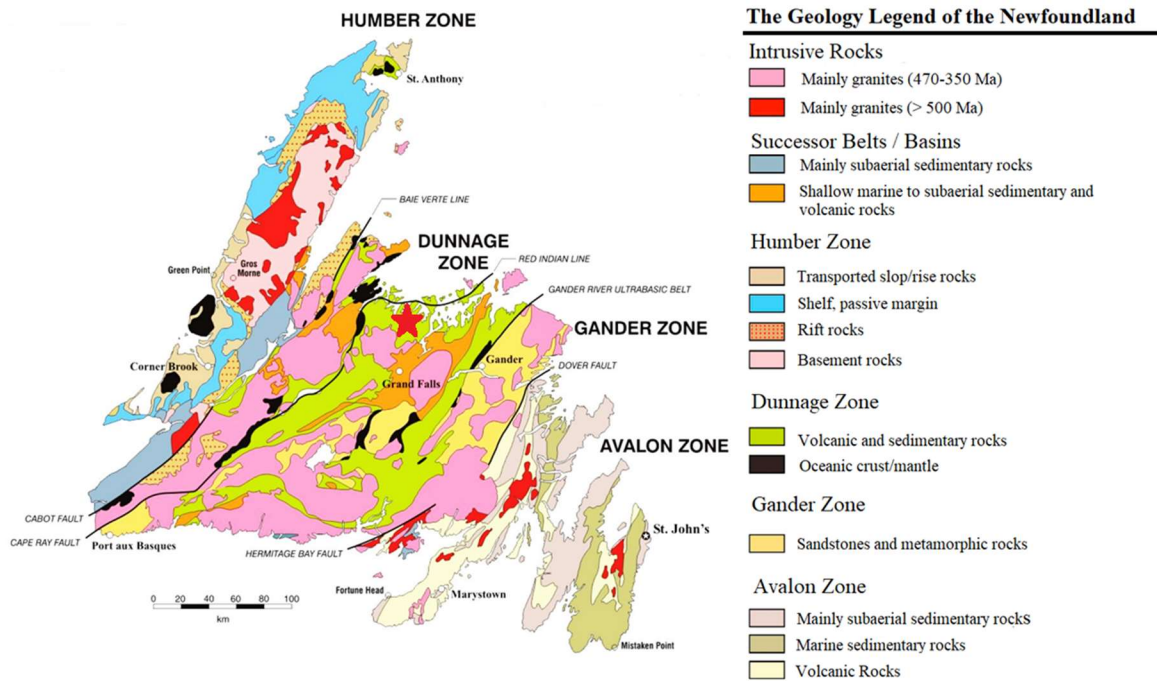
Figure 2.1: The onshore geology map of Newfoundland. The red star in the Dunnage Zone indicates the Budgell Harbour property (modified from Peace et al., 2018, and the original from the Government of Newfoundland and Labrador Department of Natural Resources).

2.2 Local geology

The Budgell Harbour Stock (BHS), located in north-central Newfoundland, is an mafic intrusive feature. The BHS is within the Dunnage Zone, and is composed of olivine gabbro, hornblende gabbro, biotite-hornblende peridotite, diorite, diatreme breccias, and lamprophyre dykes. The dykes are proposed to be radial around the BHS, and these dykes radiated outward into the country rock from the stock during magmatic intrusion of the stock (Peace et al., 2018). The BHS is a discriminated alkaline ultramafic intrusion that is probably related to a major fault system, which is related to the formation of the basins in offshore Newfoundland that are being explored for hydrocarbons (Stuckless, 2008).

6

Most of the world's largest platinum and palladium deposits are hosted in well-defined reefs occurring within layered intrusions or near the contact between mafic and ultramafic rocks (Stuckless, 2008). Due to the potentially high concentrations of platinum group metals that are found in the kind of geology found in this area, the Budgell Harbour area is significant from the economic geology point of view. The local geology of the Budgell Harbour area is shown in Figure 2.2. The BHS is an ideal target for magnetic and gravity methods because it is anticipated to have higher density and magnetic susceptibility compared to the surrounding host rocks (Miller, 1976; Geng et al., 2020).
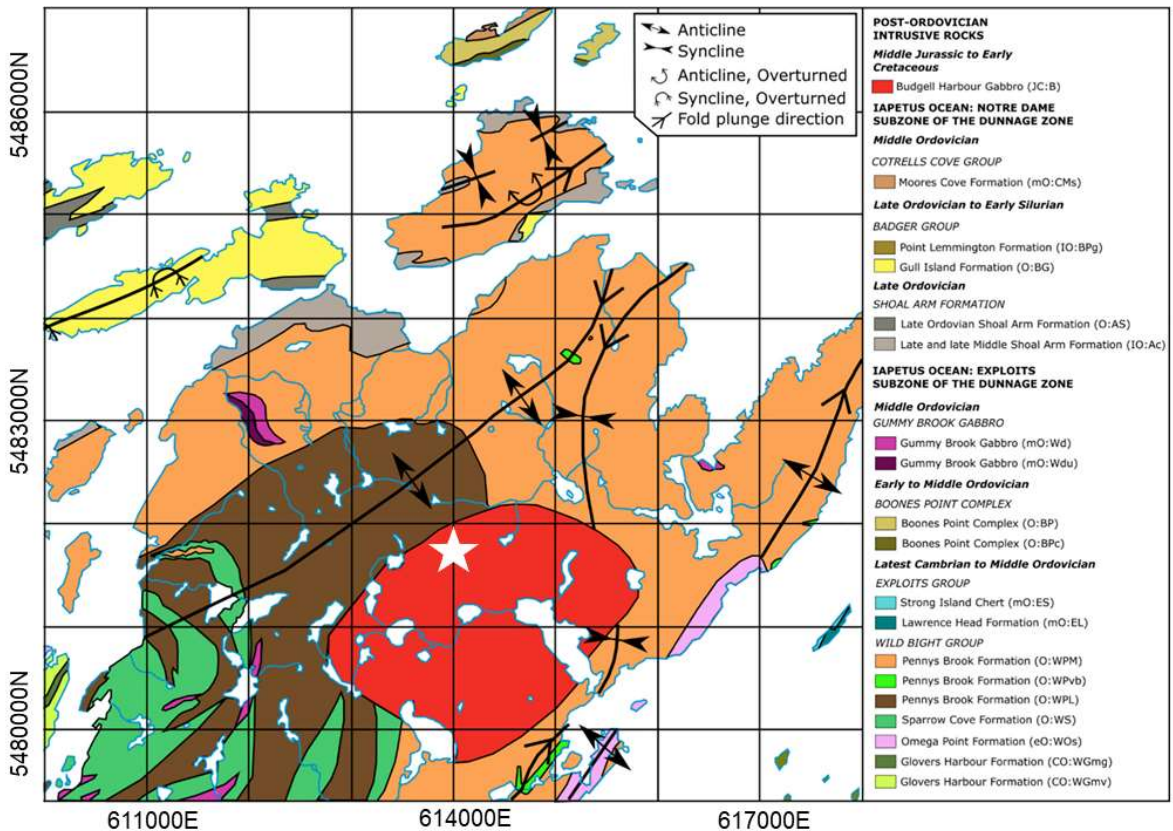
Figure 2.2: The geological map of the region surrounding the Budgell Harbour Stock area. The red area (where the white star is) is the estimated extent of the BHS based on (sparse) geological mapping (simplified from Peace et al., 2018).

The BHS has a relatively high topographic expression (Figure 2.3). The surrounding mature forest doubtless contributes to limited accessibility, therefore making field studies more problematic. Also, the weathering makes it difficult to collect fresh samples for geochemical and petrological studies. Therefore, its deeper structure is poorly exposed due to the weathering and the limited accessibility (Helwig et al., 1974; Peace et al., 2018).
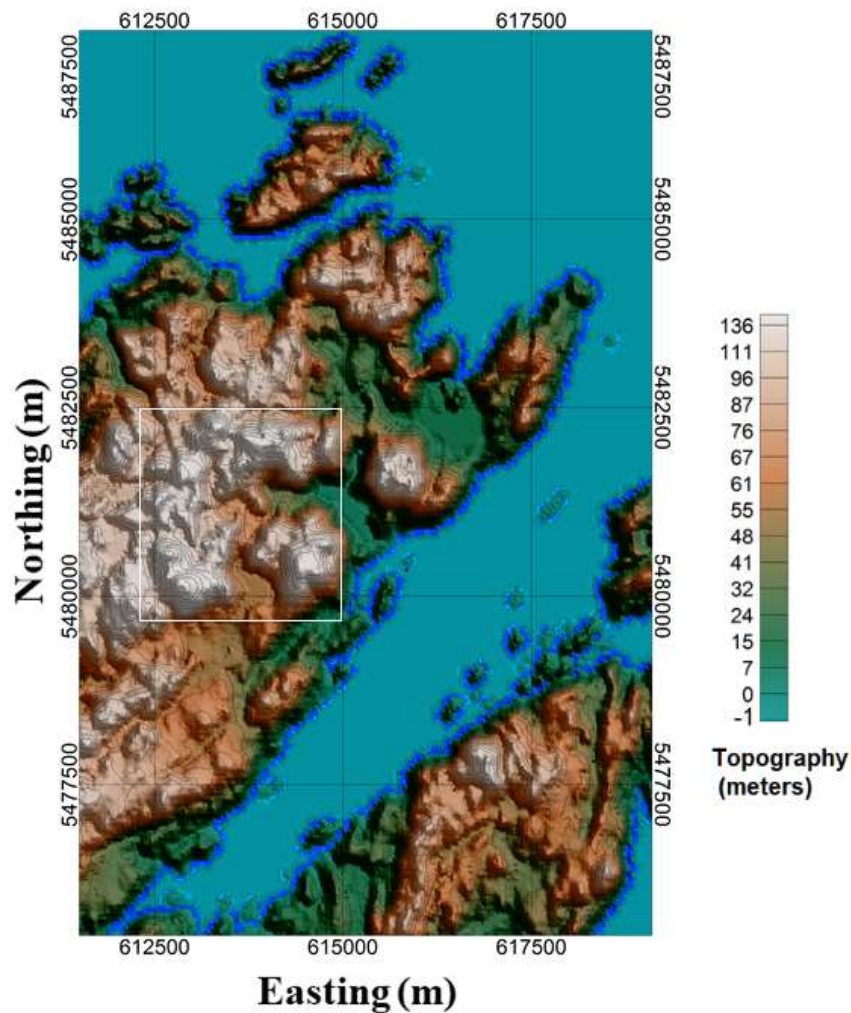
Figure 2.3: Topography map of the Budgell Harbour area generated by using the Canadian Digital Elevation Model data. The white square indicates the extent of the BHS.

2.3 Previous studies

There have been several geological and geophysical surveys carried out in the Budgell Harbour Stock (BHS) area, and different modeling and inversion approaches have been applied to the geophysics data.

Copper soil anomalies were detected over a large area within the Budgell Harbour area with values up to 1500-ppm copper (Mataragio and Kieley, 2009). The lake sediment sampling from the BHS area by the Newfoundland government reported high Cu, Ni, Co, Cr, Au, Ag, and PGE anomalies. This means that there is the potential to find mineralization and even ore deposits in the area.

Structural analysis shows that the placement of dykes was controlled by pre-existing geological structures. Potential-field studies, including analysis of observed dyke margin lineations from the structural analysis, indicate additional dykes and larger bodies similar to the BHS might present (Peace et al., 2018).

A multi-parameter geophysical survey (airborne radiometric; magnetic; VLF-EM) over the BHS was conducted in 1987 by the Geological Survey of Canada. The line spacing was 1000 m and the nominal flight altitude was 120 m. Previous aeromagnetic data that was collected by the Geological Survey of Canada (Aeromagnetic Map, 4461; Helwig et al., 1974) over the BHS was modeled as a vertical prism having a depth to the bottom of approximately 5.5 km (Figure 2.4; Miller, 1976). The susceptibility needed for the prism model in order to reproduce the data was larger than the susceptibilities that were measured on samples. The chosen susceptibility for the model was 5.5×10^{-2} G/Oe. The susceptibility

values of three samples were respectively 1.43×10^{-2}, 1.58×10^{-2}, and 1.77×10^{-2} G/Oe (Miller, 1976).
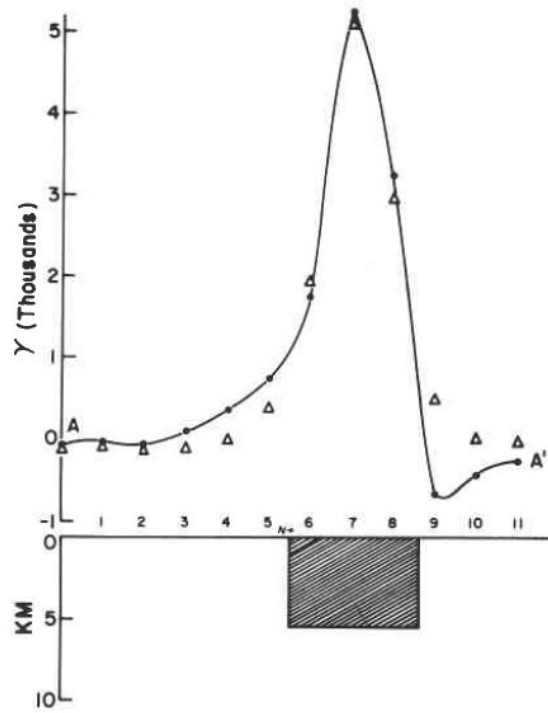
Figure 2.4: The model of the BHS constructed by Miller (1976) and the corresponding calculated and observed magnetic data. Black circles show the observed anomalies, and triangles represent the calculated anomalies.

An airborne gravity gradiometry survey was flown by Bell Geospace (their Air-Full Tensor Gradiometry, "Air-FTG" system) for Celtic Minerals Ltd. over the BHS in 2007. The line spacing was 200 m. The planned flight altitude was 80 m above sea level; however, due to sharp variation in the topography, the actual altitude varied from 70-265 m. Joint inversion of this airborne full tensor gradiometry data-set and the aeromagnetic data using a probabilistic method was presented by Geng et al. (2020).

The physical properties for the BHS determined by the joint inversion (Figure 2.5) were in good agreement with field measurements of the physical properties of lamprophyre dykes in the proximity to the BHS. The geometry of the main intrusion of the BHS constructed by the inversion resembles a steeply dipping or plunging, approximately cylindrical body with a depth extent of about 5 km. This is in contrast to the cone-shaped body produced by the independent inversion of the magnetic data by Geng et al. (2020).
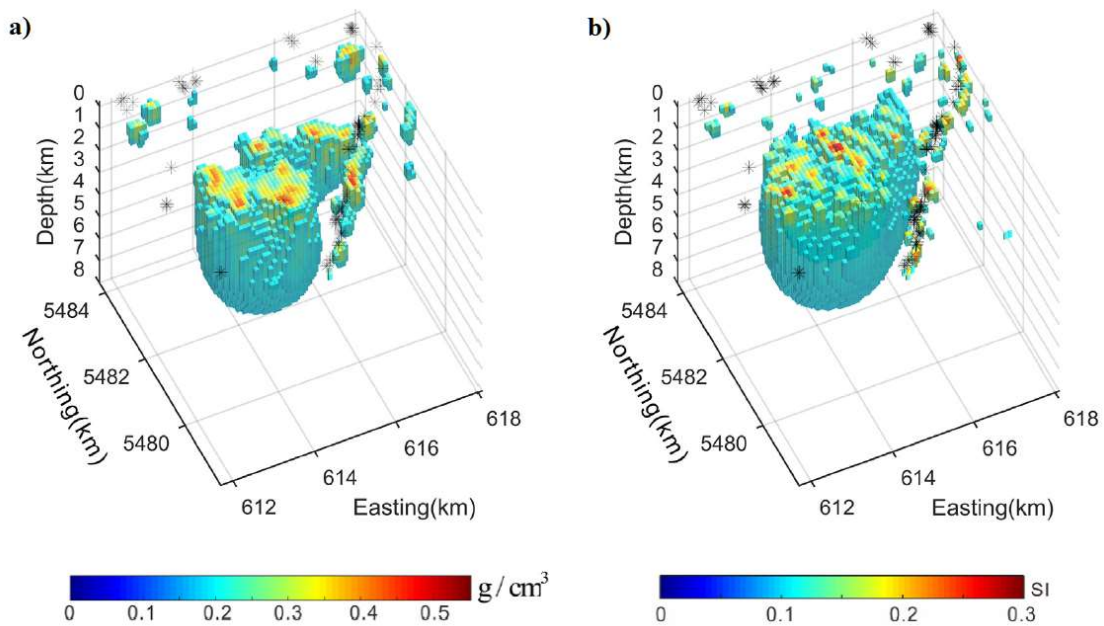
Figure 2.5: The joint inversion results of the (a) airborne gravity gradiometry and (b) aeromagnetic data for the BHS that was presented by Geng et al. (2020).

3. Theory and Methodology of the Gravity and Magnetic Methods

3.1 The gravity method

The gravity method involves the very small variations in the Earth's gravitational field that are caused by variations of subsurface rock densities. The Earth's ellipsoidal shape, rotation, and internal mass distribution also cause gravity to vary over its surface, and these must be taken into account before the variations in gravity due to local density variations can be considered (Telford et al., 1990). The gravity method is applied on land, in boreholes, from marine and airborne platforms, and using data derived from satellites (Hinze et al., 2013). Most observations are made with highly sensitive specialized devices, called gravimeters or gravity meters, which measure the acceleration of gravity. Gravimeters can discriminate variations in the value of gravity acceleration with an accuracy of one part in 10^8 or 10^9 (Blakely, 1996). Also, gravity gradiometry systems, which measure the spatial rate of change in the gravity field, have been developed for use in moving platform surveys.

3.1.1 Gravitational attraction and gravitational potential

Gravity variations are described by Newton's universal law of gravitation, which states that the force of attraction between two-point masses is inversely proportional to the square of the distance between the two masses and proportional to the product of the two masses (Telford et al., 1990; Blakely, 1996; Hinze et al., 2013):

$$\vec{F} = G\frac{m_1 m_2}{r^2} \tag{3.1}$$

where F is the force between the two masses m_1 to m_2, G is the Universal Gravitational

constant, which is equal to $6.672 \times 10^{-11} \frac{m^3}{kg} \cdot s^2$ in SI units, m_1 is the mass at $Q_1(x, y, z)$

and m_2 is the mass at $Q_2(x', y', z')$, and the two masses are separated by the distance $r =$

$[(x - x')^2 + (y - y')^2 + (z - z')^2]^{\frac{1}{2}}$ in the Cartesian coordinate system (Figure 3.1).
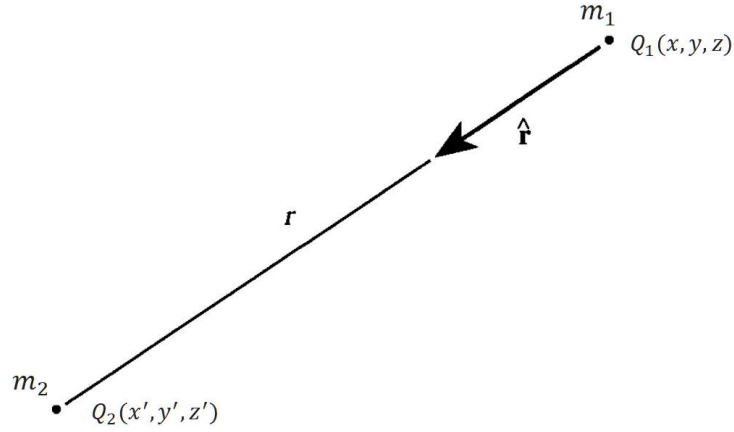
Figure 3.1: The geometry for Newton's law of gravitational attraction between two-point masses (m_1 and m_2) (modified from Blakely, 1996).

The acceleration (a) of a freely falling mass in the Earth's gravitational field is related to

the gravitational force (F) through Newton's second law:

$$\vec{F} = m_1 \vec{a} \tag{3.2}$$

which gives the force acting on the mass m_1. Comparing equation (3.2) with the formula

for the gravitational force between two point masses (equation 3.1), the gravitational

acceleration due to point mass m_2 is (Hinze et al., 2013):

$$\vec{g} = G\frac{m_2}{r^2} \qquad . \tag{3.3}$$

Gravitational acceleration is a conservative field and so the work done in moving a mass from Q_1 to Q_2 is independent of the path taken between the points (Telford et al., 1990). Therefore, it can be represented as the gradient of a scalar potential U, which is also known as Newtonian potential:

$$g(Q_1) = \nabla U(Q_1) \tag{3.4}$$

and hence, for a point mass,

$$U(Q_1) = G\frac{m_2}{r} \quad . \tag{3.5}$$

The gravitational potential of a collection of masses obeys the principle of superposition, that is, it is the sum of the gravitational potentials of the individual masses (Blakely, 1996). For a continuous distribution of mass m_1, Eq. (3.5) becomes:

$$U(Q_1) = G\int_v \frac{dm_2}{r} = G\int_v \frac{\rho(Q_2)}{r} dv \tag{3.6}$$

where v is the volume and ρ is the density within this volume (Figure 3.2).
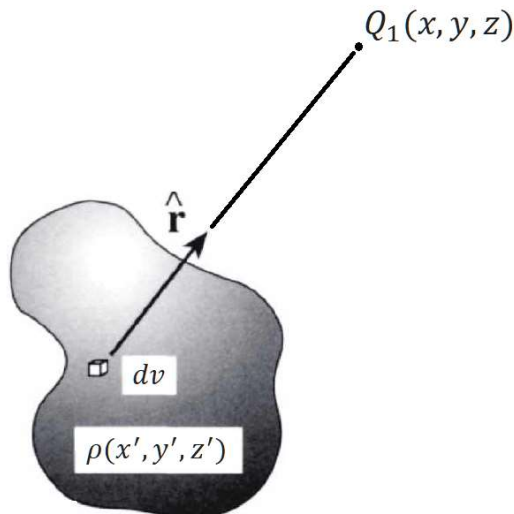
Figure 3.2: Gravitational attraction at point Q_1 due to an object of possibly variable density (modified from Blakely, 1996).

3.1.2 Gravity gradient

Gravity gradient is the second spatial derivative of the gravity potential thus quantifying the change in gravitational acceleration components, usually expressed within a Cartesian reference frame with x along-line, y across-line, and z down. The full gravity gradient tensor is comprised of nine components. This is because each of the three components of the gravity vector has a variation in each of the three mutually perpendicular coordinate axes (Murphy, 2004; Oruc and Keskinsezer, 2008):

$$T = \begin{bmatrix} \frac{\partial^2 U}{\partial x^2} & \frac{\partial^2 U}{\partial x \partial y} & \frac{\partial^2 U}{\partial x \partial z} \\ \frac{\partial^2 U}{\partial y \partial x} & \frac{\partial^2 U}{\partial y^2} & \frac{\partial^2 U}{\partial y \partial z} \\ \frac{\partial^2 U}{\partial z \partial x} & \frac{\partial^2 U}{\partial z \partial y} & \frac{\partial^2 U}{\partial z^2} \end{bmatrix} = \begin{bmatrix} T_{xx} & T_{xy} & T_{xz} \\ T_{yx} & T_{yy} & T_{yz} \\ T_{zx} & T_{zy} & T_{zz} \end{bmatrix} \tag{3.7}$$

where U is the gravity potential, and for all components (α,β) in $\{x,y,z\}$ $T_{\alpha\beta} = \frac{\partial^2 U}{\partial\alpha\partial\beta}$ (Murphy, 2004; Oruc and Keskinsezer, 2008). The gradient tensor is symmetric as the gravity is a conservative field ($T_{\alpha\beta} = T_{\beta\alpha}$). Furthermore, for measurements made above the surface of the Earth (i.e., in a density-free space, gravitational potential obeys Laplace's equation):

$$\nabla^2 U(Q_1) = \frac{\partial^2 U}{\partial x^2} + \frac{\partial^2 U}{\partial y^2} + \frac{\partial^2 U}{\partial z^2} = 0 \qquad . \tag{3.8}$$

This means that the diagonal element T_{zz} is equal to the negative sum of T_{xx} and T_{yy}. Therefore, only five components of the gradient tensor are independent *i.e.* T_{xy}, T_{xz}, T_{yz}, and any two components of T_{xx}, T_{yy}, T_{zz}. If both T_{xx} and T_{yy} are given, T_{zz} can be calculated

using Eq. (3.8). However, in practice, the T_{zz} component is usually given as the subsurface geology can be more readily interpreted from T_{zz} (Murphy, 2004).

3.1.3 Units and nomenclature

The mean value of acceleration due to gravity at the Earth's surface is about 9.80 $\frac{m}{s^2}$ or 980$\frac{cm}{s^2}$. The normal acceleration due to gravity was first measured by Galileo; and in honor of his name, the unit of acceleration due to gravity commonly used in geophysics is called the *Gal*, where 1 *Gal* is equal to 1 $\frac{cm}{s^2}$. However, the changes in the gravitational acceleration caused by variations in the density of the Earth's crust are generally small compared to the normal surface gravity value of 980 $\frac{cm}{s^2}$. Therefore, the unit milliGal (1 mGal=0.001 Gal) is often used in geophysical exploration (Hinze et al., 2013). The first gradiometer, developed in 1886 by Baron Loránd Eötvös, was a torsion balance, capable of measuring both the horizontal gradient of the vertical component of gravity and the horizontal gradient of the horizontal component. Hence, gravity gradients are measured in units called Eötvös (*E*), with 1 *E* is equal to 0.1 *mGal/km* (LaFehr and Nabighian, 2012).

3.1.4 Density

Gravity anomalies result from the density contrast between a rock mass and its surroundings. Moreover, the sign of the density contrast determines the sign of the gravity anomaly. One of the least varying parameters among all geophysical parameters is the density of rocks in the Earth's crust. The density of the most common rock types is between 1.60 and 3.20 g/cm³. The density of a rock is dependent on both its mineral composition

and porosity. The variation in porosity is the primary cause of the change in density in sedimentary rocks. Therefore, in sedimentary rock sequences, the density tends to increase with depth due to compression and with age due to progressive cementation (Hinze et al., 2013). Most metamorphic and igneous rocks have negligible porosity, and so their densities are mostly dependent on their composition. Since density generally increases as acidity decreases, there is a progression of density increase from acid through basic to ultrabasic igneous rock types (Kearey et al., 2013). Density ranges for common rock types and ores are presented in Table 3.1. For the densities of the main rock types in the Budgell Harbour area based on the Table 3.1, which is gabbro (igneous rocks), ranges from 2.70 to 3.50 g/cm^3.

Table 3.1: Densities for some common rock types and minerals (modified from Telford et al., 1990).

Material	Density Range (g/cm^3)	Material	Density Range (g/cm^3)
Sedimentary Rocks		*Metamorphic Rocks*	
Clay	1.63-2.60	Schists	2.39-2.90
Gravel	1.70-2.40	Quartzite	2.50-2.70
Limestone	1.93-2.90	Slate	2.70-2.90
Soil	1.20-2.40	Gneiss	2.59-3.00
Sand	1.70-2.30	Eclogite	3.20-3.54
Sandstone	1.61-2.76	Amphibolite	2.90-3.04
Shale	1.77-3.20	Marble	2.60-2.90
Igneous Rocks		*Metallic Minerals*	
Rhyolite	2.35-2.70	Cobaltite	5.80-6.30
Granite	2.50-2.81	Galena	7.40-7.60
Andesite	2.40-2.80	Chalcopyrite	4.10-4.30
Lavas	2.80-3.00	Hematite	4.90-5.30
Basalt	2.70-3.30	Chromite	4.30-4.60
Gabbro	2.70-3.50	Pyrite	4.90-5.20

3.1.5 Gravity corrections

From the perspective of determining density variations in the Earth's crust from gravity measurements, there are some undesirable impacts on gravity measurements caused by the rotation and shape of the Earth. As the Earth is not perfectly spherical or homogeneous, gravitational acceleration is not constant over its surface. To obtain more accurate information and make a better interpretation of a gravity surveys, it is essential to correct for all variations in the gravitational field measurements that are not caused by the differences of density in the subsurface. The location and elevation of the gravimeter during a gravity survey should be precisely known to apply the corrections accurately. Corrections for gravity and gravity gradiometry are as follows (Kearey et al., 2013).

Tidal Correction: Measured gravity at a fixed location changes over time due to the periodic change in gravitational effects associated with the orbital movements of the Sun and Moon, and this alteration must be corrected for in high-precision surveys. In comparison to other corrections to gravity measurement, the tidal effect is a small quantity and never exceeds 0.3 *mGal*. (Telford et al., 1990; Blakely 1996).

The corrections that are mentioned above would involve adding or subtracting the same correction value to closely spaced in location of two gravity measurements. For airborne gravity, in addition to the Eötvös correction, the **vertical (heave)** correction needs to be added. This is because the aircraft does not fly at a constant level, so there is additional acceleration due to the aircraft motion. However, in the gradient measurement, those two closely spaced in location of gravity gradient components are subtracted from one another so that the corrections that have been done to both these components will cancel out.

18

Therefore, in order to enhance the data clarity for interpretation purposes of the airborne gravity gradiometry data, only terrain corrections.

Drift Correction: Gravimeters are highly sensitive instruments. The elastic feature of springs in the most common type of gravimeters varies with time. This also causes the measurement recorded by a gravimeter to change with time as well. The solution is to repeat readings at a base station several times throughout the day and plot the readings against time (Figure 3.3). For the drift correction, these readings' values should be subtracted from the observed values.
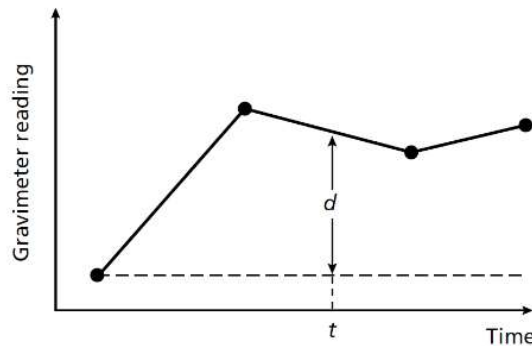
Figure 3.3: A gravimeter drift curve plotted from repeated readings at a fixed location, and the drift correction value (d) to be subtracted for a reading taken at time (t) (Kearey et al., 2013).

Latitude Correction: Gravity varies with latitude for two reasons. The angular velocity of a point on the Earth's surface due to the rotation of the Earth decreases when moving from the equator to the poles. Centripetal acceleration generates a rotation, which has a negative radial component which increases from the poles to the equator. Also, the shape of the Earth is an oblate spheroid or polar flattened ellipsoid, whose difference in equatorial and polar radii is about 21 km (Figure 3.4). Therefore, points near to the equator are farther

from the Earth's center of mass than the poles, also causing gravity to increase from the equator towards the poles (Kearey et al., 2013).
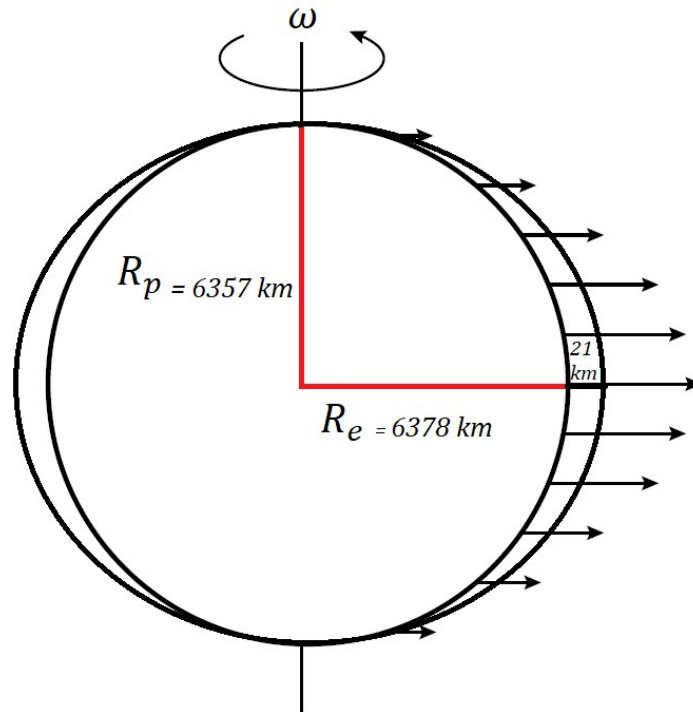
Figure 3.4: The variation in angular velocity (ω) with latitude over the Earth indicated by vectors and the exaggerated representation of the shape of the Earth in which R_p is the radius at the poles, and R_e is the radius at the equator (modified from Kearey et al., 2013).

Gravity prospecting developed from the analysis of the Earth's gravitational field for ascertaining the shape of the Earth. Modern analyses of the Earth's shape are based on precise observations of the orbits of artificial earth satellites. These data are used to define a best-fitting oblate ellipsoid, called the *International Reference Ellipsoid* (Telford et al., 1990). If the interior of the earth were uniform, the value of gravity on the international reference ellipsoid would alter with latitude according to the following formula known as theoretical gravity or normal gravity (Blakely, 1996):

$$g_0 = 978031.846 \left(1 + 0.0053024 \sin^2 \varphi - 0.0000058 \sin^2 2\,\varphi\right) mGal \quad . \qquad (3.9)$$

where φ is latitude (in degrees). For a small scale area, the station locations are not referenced to global latitude but are determined by assuming a linear variation as a function of north-south distance; the formula for latitude correction becomes (LaFehr and Nabighian, 2012):

$$\Delta g_L = 0.812 \sin (2\varphi) mGal)/km \qquad . \qquad (3.10)$$

The correction values have their maximum value at 45° latitude and are added to g as the measurement moves toward the equator (Telford et al., 1990).

Free-air correction (FAC): According to Newton's law, as gravity decreases with height above the surface of the Earth (reference ellipsoid) in the free air, a free-air correction (FAC) should be applied to the data. To acquire the change in gravity acceleration with the height (h), Eq. (3.4) can be differentiated:

$$FAC = \Delta g_{FA} = \frac{\partial g_{FA}}{\partial R} = 2G \frac{M_e}{R_{e3}} = 0.3086 \times h\, mGal \qquad . \qquad (3.11)$$

where h is the elevation (metres in SI units) of each gravity station above the datum; M_e is the mass of the Earth, and R_e is the radius of the Earth (Figure 3.5a). The FAC does not take account of the gravitational effect of any rock present between the observation point and datum. The FAC is added to the field reading for an observation point above datum to correct for the decrease in gravity with elevation (Kearey et al., 2013).

Bouguer correction (BC): The Bouguer correction (BC) attempts to eliminate the gravitational effect of the rock present between the observation point and datum by

approximating the rock layer below the observation point with an infinite horizontal slab

with a thickness equal to the height of the observation point above the datum (Figure 3.5b).

Assuming a constant density, ρ, of the rock, the Bouguer correction (BC) is calculated from

the following equation (Kearey et al., 2013):

$$BC = \Delta g_B = 2\pi G \rho h = 0.0419 \rho h \; mGal \qquad . \qquad (3.12)$$

where G is the gravitational constant, ρ is the average density of the underlying rocks in

g/cm^3 (the average density value is usually assumed 2.67 g/cm^3), and h is the elevation in

metres. The BC must be subtracted from the measurements that take place on land as the

gravitational attraction of the rock must be removed from the observed gravity value. For

sea surface observations, the BC must be added due to the absence of rock between the sea

surface and sea bed (Kearey et al., 2013). The Bouguer and free-air corrections are often

combined into an *elevation correction* (Telford et al., 1990):

$$\Delta g_E = \Delta g_{FA} - \Delta g_B$$

$$\Delta g_E = (0.3086 - 0.0419\rho) \times h \; mGal \qquad (3.13)$$

where Δg_E is the elevation correction, which is the first step in removing topography effects

from observed gravity values.

Terrain correction (TC): The Bouguer correction assumes that the topography around

the gravity station is flat; however, this is seldom the case in reality. Therefore, an

additional correction should be made to account for the topographic relief near the gravity

station, which is called the terrain correction. Terrain correction is always positive in

ground gravity surveys whether the topography consists of a mountain or a valley (Figure 3.5c). In airborne surveys, the terrain correction is also positive and added for the measurements (Hinze et al., 2013).
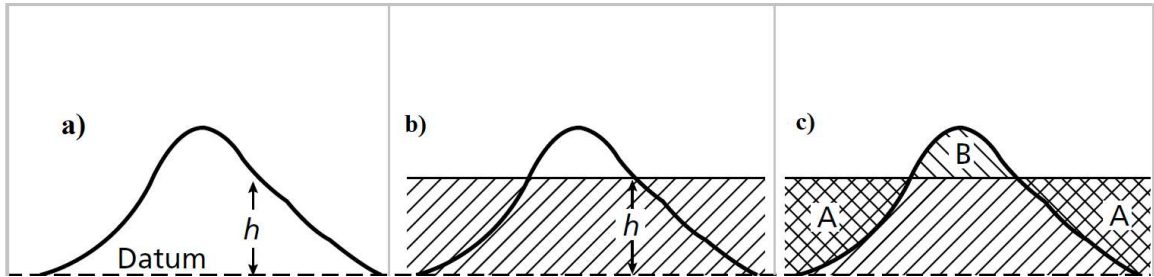
Figure 3.5 : (a) The free-air correction for the observation at a height h above datum, (b) the Bouguer correction, and (c) the terrain correction (modified from Kearey et al., 2013).

Eötvös correction: The observation platform will have an angular velocity different from that predicted by the Earth model for that particular latitude when the gravity measurements are made on a moving vehicle, for instance, a ship or an aircraft. The vehicular motion will generate a centripetal acceleration, which will either strengthen or oppose gravity, depending on the direction of the measurement. Therefore, a correction is required, which is known as the Eötvös correction (Chapin, 1996; Kearey et al., 2013):

$$E = 7.503\, V \sin(a) \cos(\varphi) + 0.004154\, V^2\, mGal \qquad (3.14)$$

where the speed of the vehicle is V in knots, a is the platform heading in degrees from North, and φ is the latitude in degrees.

3.1.6 Anomalies

3.1.6.1 Gravity anomalies

The main goal of the gravity method is to improve and contribute to the understanding of the subsurface. Therefore, any effects that are not related to subsurface geology must be removed in the data correction (or reduction) process. (See the section above for descriptions of these corrections.) A gravity anomaly is the difference between the measured gravity and the theoretical gravity based on a defined Earth model (LaFehr and Nabighian, 2012). The calculation of the free-air anomaly (FAA) and the complete Bouguer anomaly (CBA) are as follows (Kearey et al., 2013):

$$FAA = g_{obs} - g_L + g_{FA} \; (\pm E) \tag{3.15}$$

$$CBA = g_{obs} - g_L + g_{FA} \pm g_B + TC \; (\pm E) \tag{3.16}$$

where g_{obs} is the observed gravity value, TC represents the terrain correction, and E is the Eötvös correction.

The Bouguer anomaly underlies the interpretation of gravity data on land (Kearey et al., 2013). If the subsurface, all the way up to the surface interface, had a density equal to the value used in the Bouguer correction, then the Bouguer anomaly would be zero. Bouguer anomalies are traditionally calculated for inshore and shallow water areas, as the Bouguer correction eliminates local gravity effects associated with local changes in water depth. However, the Bouguer anomaly is not appropriate for deeper water surveys. Therefore, the free-air anomaly is often used to interpret deep-water surveys. An example of free-air and

complete Bouguer anomaly maps of the whole of planet Earth are shown respectively in

Figures 3.6 and 3.7 (Bonvalot et al., 2012).
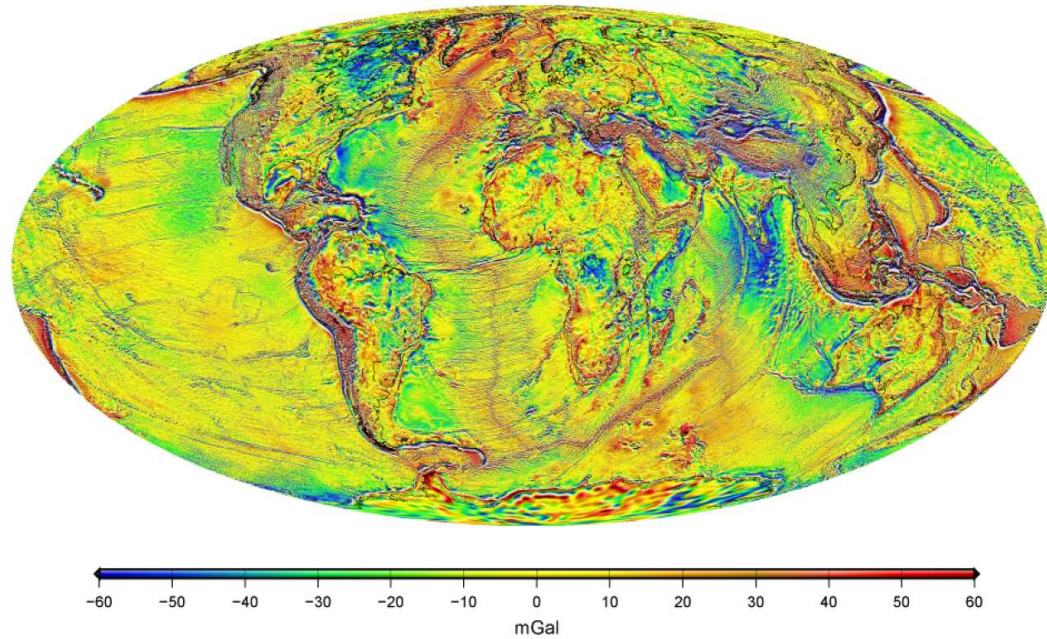
Figure 3.6: The global free-air gravity anomaly (modified from Bonvalot et al., 2012).
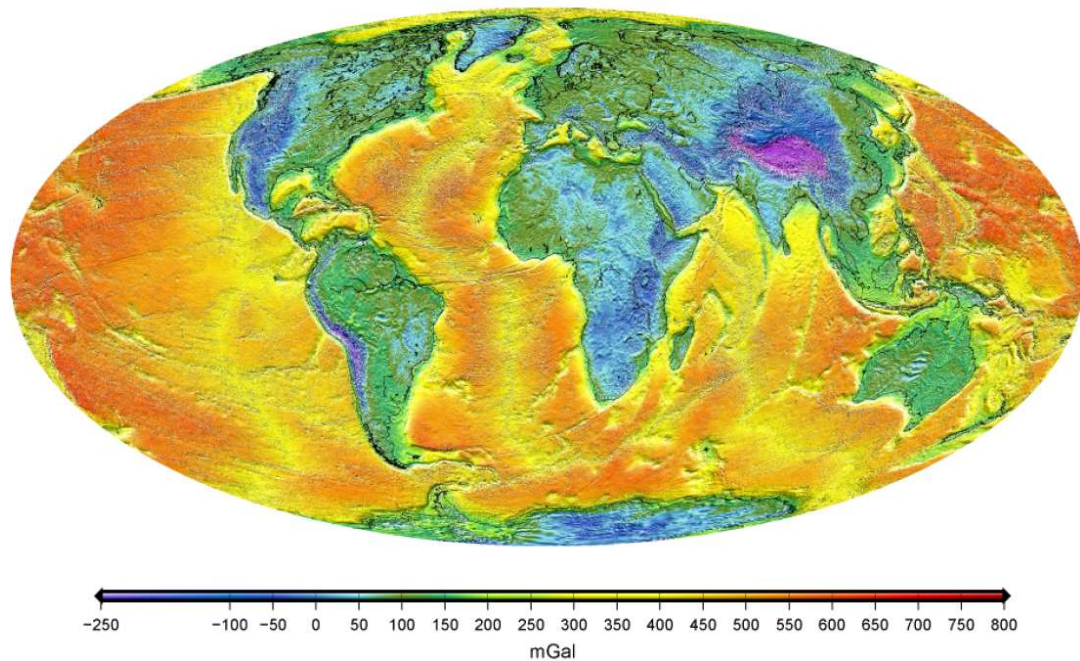
Figure 3.7: The global Complete Bouguer gravity anomaly (modified from Bonvalot et al., 2012).

3.1.6.2 Gravity gradient anomalies

The use of gravity gradient data in geophysical exploration has become more common since the development of airborne systems. Gravity gradiometry measurements are often made in the air as the measurements are barely impacted by the large accelerations associated with the movement of the aircraft compared with measurements of normal gravity from a plane. However, the interpretation of gravity gradient data is not as simple as that for the vertical component of gravity data. For a given source, gravity gradients usually produce a complex pattern of anomalies as compared to normal gravity anomalies (Saad, 2006).

A pattern of gravity gradients and the vertical component of gravity for a simple dense block in a zero-density half-space is shown in Figure 3.8. This figure uses a left-hand coordinate system where x is East, y is North, and positive z points are upwards. This is because the measurements considered later in this thesis were made by the Bell Geospace Air-FTG system and the measured data were provided in a left-hand coordinate system. The dense block is 100 m by 100 m by 100 m and is centered at 250 m East and 250 m North. The top surface of the block is located at a depth of 100 m.

As can be seen from Figure 3.8, the T_{xx} component indicates the western and eastern edges of the block. Similarly, the T_{yy} component emphasizes the north and south edges. The T_{xz} component separates the block into east and west halves along a north-south zero line that passes over the centre of the block. The T_{yz} component similarly divides the block into north and south halves. The T_{xy} component shows opposite highs and lows that point to the center of mass and highlight the corners of the block. The vertical component (T_{zz}), which

is the first vertical derivative of "normal" gravity (G_z), is the gradient component most similar to the vertical component of gravity (G_z). This component maps density variations, as the signal occurs over the density anomaly, and can be used to predict the depth and estimate the composition of a target (Murphy 2004).
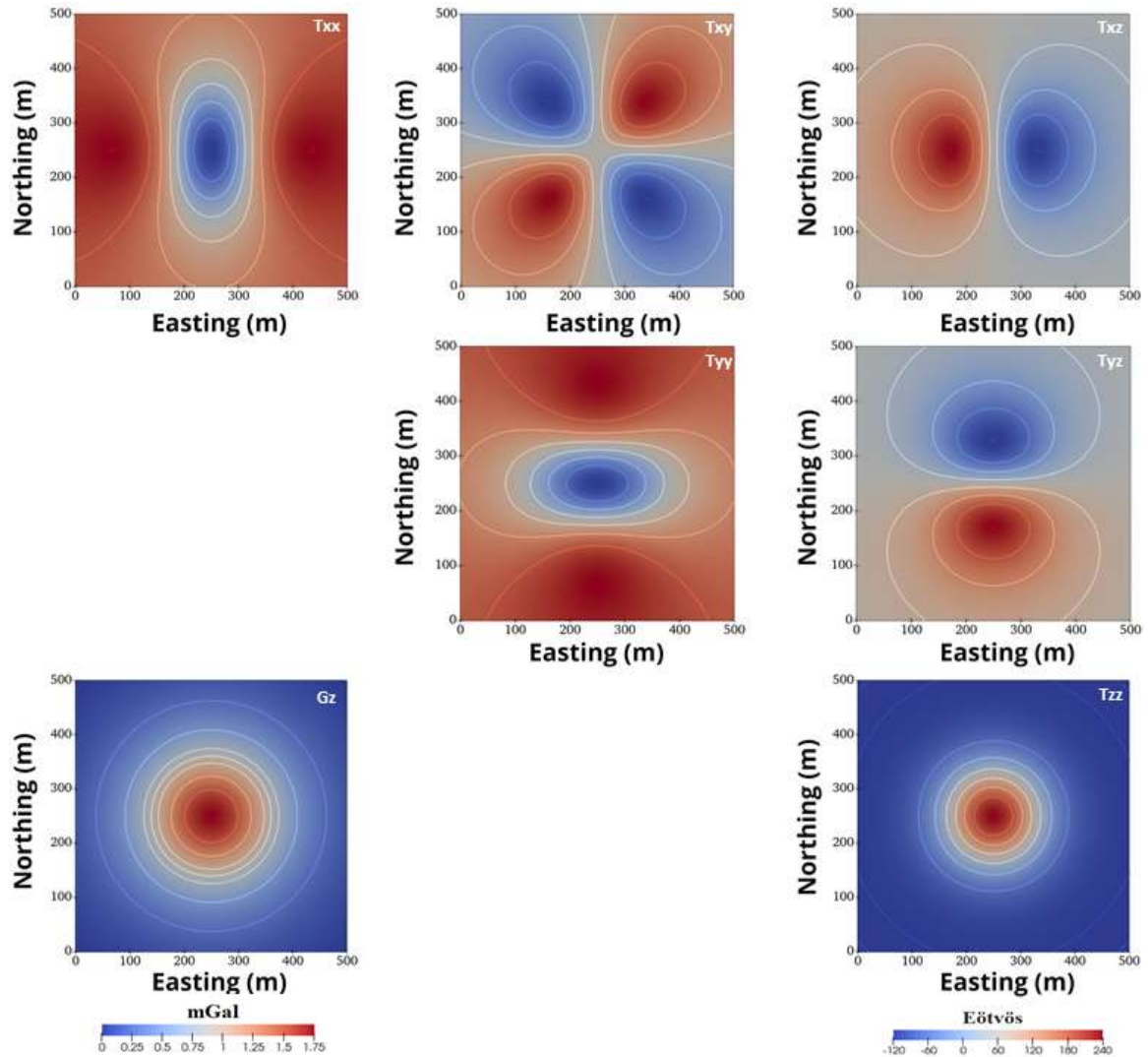
Figure 3.8: Gravity gradient component patterns ($T_{xx}, T_{xy}, T_{xz}, T_{yy}, T_{yz}, T_{zz}$ respectively from left-top to right bottom) and the vertical component of gravity (G_z) for a dense cube in a zero-density half-space using a left-hand coordinate system where x is East, y is North, and positive z is upwards.

3.1.7 Airborne gravity gradiometry

The use of the gravity gradiometry method in geophysical exploration has grown since the 1980s due to the technological development in the instruments. Airborne measurements are accomplished by taking gradiometers into airplanes and helicopters. Two significant advantages of using airborne measurements are the ability to cover large areas rapidly and to access remote areas that were previously inaccessible (Nabighian et al., 2005).

Airborne gravity systems have been developed as well as gradiometry systems. Airborne gravity systems provide rapid data acquisition, high resolution and accuracy below 1 *mGal* (Fairhead et al., 2017). Moreover, as its increased resolution handles air turbulence better, it is now routinely integrated on a single platform with magnetic sensors to ensure an ideal survey option for both regional and targeted resource evaluation studies. However, extra corrections need to be applied to the airborne gravity data compared to airborne gravity gradiometry, such as Eötvös and vertical (heave) correction (see section 3.1.5). Overall, airborne instrumentation, data acquisition, processing, interpretation methodologies, and techniques have gradually decreased survey noise and enhanced overall survey resolution.

The Falcon system is considered the first airborne gravity gradiometer, tested in 1997, and used for an airborne survey in 1999 (Carlos et al., 2013). In general, the main processing steps for gravity gradiometry data are terrain correction (see above) and flight line correction. The two systems that are currently and most commonly used for airborne gravity gradiometry measurements are called "Air-FTG" (Bell Geospace) and "Falcon" (CGG) gradiometry systems. The main difference between these two systems is that Air-FTG measures the five independent components of gravity gradient whereas the Falcon

system measures two components, and then the vertical gradient component *(Tzz)* is calculated. A comparison of the error levels of the noise for the Air-FTG and the Falcon system is provided by Dransfield (2007) and shown in Figure 3.9. The subsurface geological features of most interest in exploration geophysics range in size from tens of metres to tens of kilometres. The decreasing strength of the signal with distance from the density anomaly means that it is preferable to fly at a height determined by the minimum size and depth of the features sought. Additionally, the measurement spacing should be sufficiently small to be able to detect such features. Ideally, an airborne geophysical system should collect data at altitudes of less than a hundred metres, spaced at a few tens of metres. These requirements are very challenging for airborne gravity or gravity gradiometry surveys (Carlos et al., 2013).
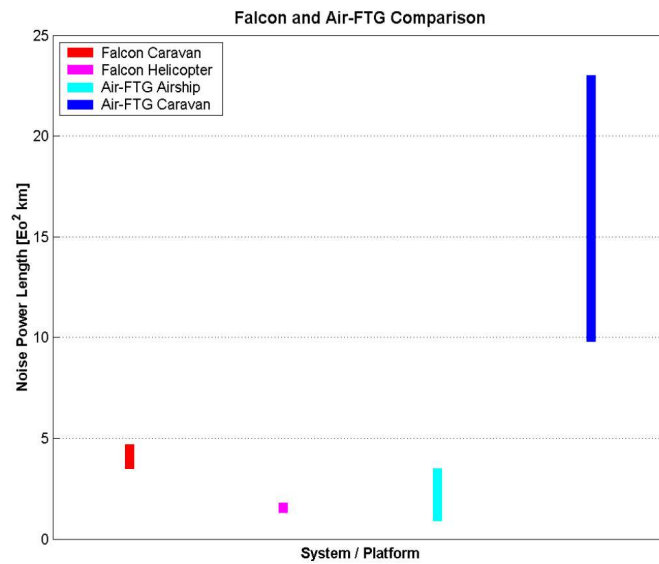
Figure 3.9: The comparison of error levels from four different airborne gravity gradiometry installations. The comparison is given in noise power density, where the lowest noise power density corresponds to better sensitivity and resolution (Dransfield, 2007).

3.2 The magnetic method

The purpose of a magnetic survey is to investigate underground geology based on anomalies in the Earth's magnetic field caused by the magnetic properties of the underlying rocks (Kearey et al., 2013). Although most rock-forming minerals are not magnetic, some rocks contain enough magnetic minerals to produce significant variations in the Earth's magnetic field. Magnetic measurement, therefore, has a wide range of applications, from small-scale engineering or archaeological research, to detecting buried metal objects, to mineral exploration, and to large-scale surveys conducted to investigate regional geological structure. Magnetic surveys can be done on land, sea, and air. As a result, the technique is widely used. Also, an aeromagnetic survey is very attractive for the exploration of types of ore deposits containing magnetic minerals as it is able to delineate the target of interest effectively.

3.2.1 Magnetic force and field attraction

"Following is the description of the fundamentals of the magnetics method. It is done by using magnetic charges. I realize that there are other ways to think about the fundamentals of magnetic fields. However, I am more comfortable with the description below (For other ways to think about it, please see Blakely,1995)."

The magnetic field due to two monopoles is given by Coulomb's law, which states that the magnetic force is inversely proportional to the square of the distance between two magnetic poles and proportionate to the product of their strengths (Hinze et al., 2013; Kearey et al., 2013):

$$F_m = \frac{1}{\mu} \frac{P_1 P_2}{r^2} \tag{3.18}$$

where F_m is the magnetic force; μ is a constant of proportionality known as the magnetic permeability that is approximately equal to $4\pi \times 10^{-7}$ N·A^{-2} in free space; P_1 and P_2 are the strengths of the two fictitious magnetic poles, and r is the distance between the two poles. If the poles are of opposite sign, the force is attractive and therefore moves them towards each other, whereas if the poles are of the same sign, the force is repulsive and operates to separate them apart.

The magnetic element comprises two magnetic monopoles, including one positive and one negative within some distance that is called a magnetic dipole in which a magnetic flux exists around a bar (Figure 3.10; Kearey et al., 2013). The pole of the magnet that indicates the direction of the Earth's north pole is called the positive pole (or the north-seeking) which is equalized by a negative pole (or the south-seeking) at the opposite end of the magnet.
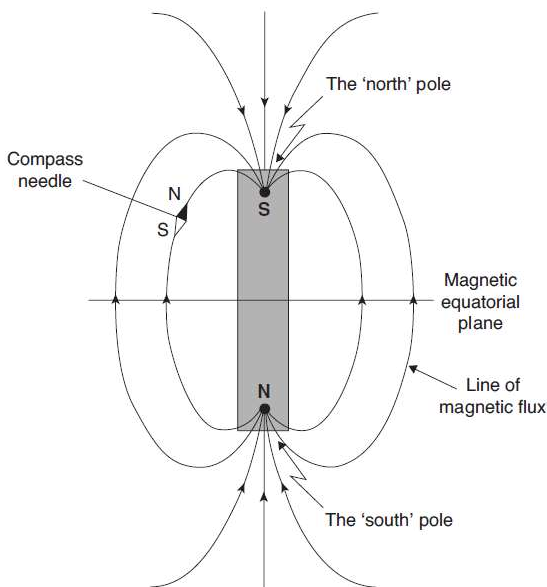
Figure 3.10: The magnetic flux around a bar magnet (Reynolds, 2011).

The magnetic force cannot be identified independently of the fundamental property of the pole strength as in gravitational fields. Therefore, the magnetic field (**B**) due to a pole of strength (P_2) at a distance from the pole is defined as the force on a unit positive pole:

$$B = \frac{F_m}{P_1} = \frac{1}{\mu} \frac{P_2}{r^2} \qquad (3.19)$$

where P_1 is an imaginary unit pole at a point in space where B is specified. It is assumed that P_2 is much greater than P_1; hence P_1 does not disturb field B. The units of the magnetic field strength (B) are Tesla. The units of magnetization force (H) are measured in Ampères per metre (A/m) in SI units and in Oersteds (Oe) in c.g.s. units where 1 A/m is equal to $4\pi \times 10^{-3}$ Oe or 0.0126 Oe. However, in geophysics, the SI unit used is nanoTesla (nT) as the Tesla is a too-large unit to express the small magnetic anomalies (1 nT=10^{-9} T). Also, the c.g.s. system employs the numerically equivalent gamma (γ), which is equal to 10^{-5} Gauss (1 Gauss = 10^{-4} T) (Kearey et al., 2013).

Once a material is placed in a magnetic field, it might obtain a magnetization in the direction of the field that is lost when the material is removed from the magnetic field. This is known as induced magnetization or magnetic polarization and is caused by the fundamental dipoles in the material aligning in the field direction. Due to this alignment, the material has magnetic poles distributed on its surface corresponding to the ends of the dipoles (Figure 3.11). The intensity of induced magnetization is proportional to the strength of the magnetizing force of the inducing field (Hinze et al., 2013; Kearey et al., 2013):

$$J_i = kH \qquad (3.20)$$

where J_i is the intensity of induced magnetization, k is the magnetic susceptibility of the material, and H is the magnetization force. The units of J_i and H are both measured in A/m; hence, susceptibility (k) is dimensionless in SI units.
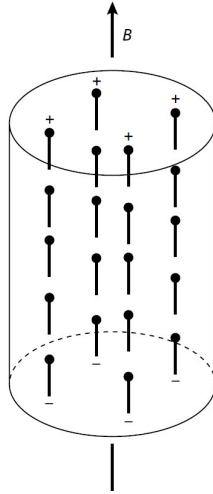
Figure 3.11: The illustration of an element of material in which elementary magnetic dipoles align in the direction of an external magnetic field (B) to produce an overall induced magnetization (modified from Kearey et al., 2013).

In a vacuum, the magnetic field strength B and the magnetization force H are related through $B = \mu_0 H$, where μ_0 is the permeability of the vacuum. Air and water have very similar permeabilities to μ_0. Therefore, this relationship can be used to represent the magnetic field of the Earth when not disturbed by magnetic materials. When a magnetic material is placed in this field, the resulting magnetization leads to an additional magnetic field whose strength is given by $\mu_0 J_i$ in the region occupied by the material. Total magnetic field or magnetic induction B within the body is given as:

$$B = \mu_0 H + \mu_0 J_i \qquad (3.21)$$

and substituting equation 3.20, equation 3.21 becomes:

$$B = \mu_0 H + \mu_0 kH = (1 + k)\mu_0 H \qquad (3.22)$$

where B is the total magnetic field, including the effect of magnetization. There is this other kind of magnetization, which is different from induced magnetization that is called *remanent magnetization*. If the magnetic material has large susceptibilities, the magnetic material will reserve a part of its induced magnetization. The remanent magnetization is challenging to deal with as the direction of the remanent magnetization cannot be known (Kearey et al., 2013).

3.2.2 The geomagnetic field

Magnetic anomalies generated by rocks within the crust are localized effects superimposed on the Earth's geodynamic magnetic field (i.e., the geomagnetic field). As a result, knowing the behavior of the geomagnetic field is necessary both in reducing the magnetic data to a suitable anomaly and in determining the direction of the induced magnetization of a rock. The geomagnetic field is geometrically more complex than the Earth's gravitational field, mostly because it is a dipolar field and demonstrates irregular changes in both orientation and magnitude with latitude, longitude, and time.

On the Earth's surface at any given point, a freely hanging magnetic needle will take an orientation in space in the direction of the surrounding geomagnetic field. This will usually be at an angle to both vertical and horizontal. Descriptors, known as geomagnetic elements, are used to describe the magnetic field vector (Figure 3.12). The total field vector ($\vec{B}$) has a horizontal component ($\vec{H}$) in the magnetic north direction and a vertical component (Z).

The dip of *B* is the inclination of the field (*I*), and the declination (*D*) is the horizontal angle between geographic and magnetic north. The value of declination is positive to the east and varies from 0 to 360 degrees. The total field vector (*B*) strengths vary from 25,000 nT in the equatorial regions to about 70,000 nT at the poles (Kearey et al., 2013). For Budgell Harbour Stock (BHS) on the date of September 1,2020, the declination is -20.23; the inclination 72.07, and the field strength is 53,646 nT (Government of Canada, Magnetic Calculator, 2020).
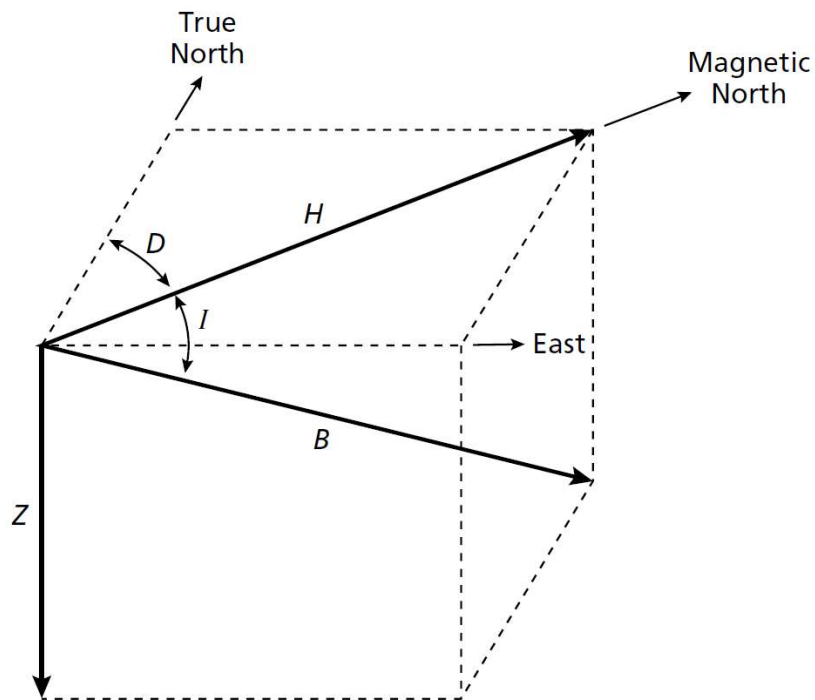
Figure 3.12: The geomagnetic elements. D is declination, I is inclination, Z is the vertical component, and H is the horizontal component of the total field vector (modified from Kearey et al., 2013).

In the northern hemisphere, the magnetic field usually dips northward and becomes vertical at the north magnetic pole (Figure 3.13). In the southern hemisphere, the dip is usually

northward and upward. The zero-inclination line comes close to the geographic equator and is known as the magnetic equator.
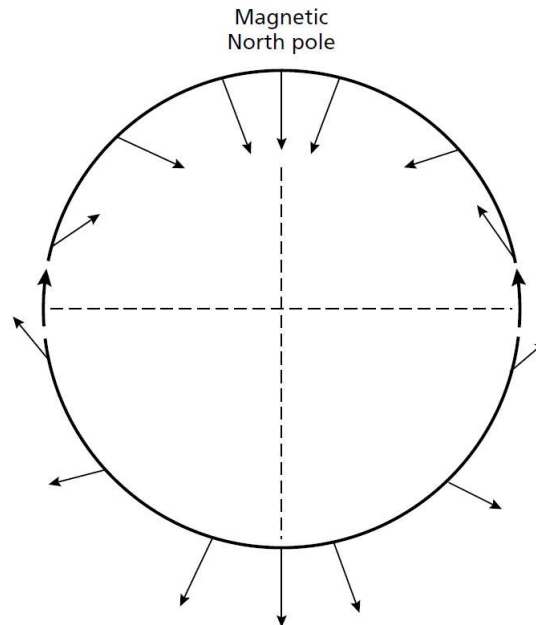
Figure 3.13: The changes in the inclination of the total magnetic field with latitude based on a simple dipole approximation of the geomagnetic field (modified from Kearey et al., 2013).

3.2.3 Susceptibility

Most common rock-forming minerals present a very low magnetic susceptibility, and rocks owe their magnetic properties to the mostly small proportion of magnetic minerals that they contain. The most widespread magnetic mineral is magnetite, with a Curie temperature of about 600 ° C. Although the size, shape, and distribution of magnetite grains in a rock affect its magnetic character, it is reasonable to classify the magnetic behavior of rocks according to their general magnetite content (Kearey et al., 2013).

Mafic igneous rocks can be highly magnetic due to their relatively high magnetite content. The ratio of magnetite in igneous rocks tends to decrease with increasing felsic rock, usually being less magnetic than basic rocks. Metamorphic rocks are variable in their magnetic character as well. Magnetite is reabsorbed, and iron and oxygen are incorporated into other mineral phases as the degree of metamorphism increases if the partial pressure of oxygen is relatively low. The relatively high oxygen partial pressure, however, may cause the formation of magnetite as an accessory mineral in metamorphic reactions (Reynolds, 2011). The susceptibility ranges for common rock types are presented in Table 3.2.

Table 3.2: The susceptibility ranges for common rock types (simplified from Telford et al., 1990).

Material	Susceptibility Range x 10^3 [SI]	Material	Susceptibility Range x 10^3 [SI]
Sedimentary Rocks		*Metamorphic Rocks*	
Dolomite	0-0.9	Schists	0.3-3
Shale	0.01-15	Serpentine	3-17
Limestone	0-3	Slate	0-35
Sandstone	0-20	Gneiss	0.1-25
Igneous Rocks		*Minerals*	
Gabbro	1-90	Magnetite	1200-19200
Basalt	0.2-175	Hematite	0.5-35
Rhyolite	0.2-35	Chromite	3-110
Granite	0-50	Pyrrhotite	1-6000

3.2.4 Magnetic data reductions

The reduction of magnetic data is required to eliminate all causes of magnetic variations from the observations other than those deriving from the magnetic effects of the subsurface. Since the Earth's magnetic field strength varies from 25,000 nT at the magnetic equator to 70,000 nT at the poles, the increase in magnitude with latitude needs to be taken into account. A survey datum at any location can be corrected using the International Geomagnetic Reference Field (IGRF), which expresses the undisturbed geomagnetic field in terms of multiple spherical harmonics and contains temporal terms to correct for secular variation. Subtracting the IGRF value from the observed data removes the large fields generated by electric currents in the outer core: this is known as the *geomagnetic correction*. The IGRF derives the spherical harmonics from observatory data. As a result, the IGRF in areas remote from observatories can be signifanctly in error (Hinze et al., 2013).

The magnetic effects of external sources cause the geomagnetic field to change daily and produce *diurnal variations*. The diurnal variation is generally smooth and regular and has an amplitude of about 20-80nT. This variation is due to the magnetic field caused by the flow of charged particles in the ionosphere both their circulation patterns and diurnal variations differ in sympathy with the tidal effects of the Sun and Moon. Some days (D or disturbed days) are distinguished by much less regular daily variations and include short-term disturbances in the geomagnetic field with an amplitude of up to 1000 nT, known as *magnetic storms* (Reynolds, 2011). Such days are often associated with intense solar activity and are due to the arrival of charged solar particles into the ionosphere. Magnetic

measurements should be discontinued during such storms because the data collected for rapid and high amplitude changes in the magnetic field cannot be corrected. Therefore, the measurements should be repeated at a particular point (a base station) throughout the duration of a survey so that variations with time can be measured and observed for determining whether these are diurnal variations. For airborne surveys, tie lines are used to get some repeat measurements at a set of locations.

The effect of topography might be important in ground magnetic surveys; however, it is not always the case as it depends on the magnetic properties of topographic features. Thus, *terrain corrections* are seldom applied in a magnetic survey. After applying diurnal and geomagnetic corrections, the remaining magnetic field variations should be solely caused by spatial changes in the magnetic properties of the subsurface and are called *residual data* or *magnetic anomalies* (Kearey et al., 2013).

3.2.5 Magnetic anomalies

All magnetic anomalies caused by rocks are superimposed on the geomagnetic field, just as gravity anomalies are superimposed on the Earth's gravitational field. If the normal geomagnetic field is described by a vector diagram (Figure 3.14a), the geomagnetic elements are related as follows:

$$B^2 = H^2 + Z^2 \qquad (3.23)$$

where B is the total field, H is the horizontal component, and Z is the vertical component of the total field vector. A magnetic anomaly causes a change (ΔB) in the strength of the total field vector (B). If the anomaly has a vertical component ΔZ and a horizontal

component ΔH at an angle α (Figure 3.14b), the anomaly will contribute to H only the part of ΔH in the direction of H, that is due to the difference in magnitude of H and ΔH:

$$\Delta H' = \Delta H cos\alpha \tag{3.24}$$

By using a similar vector diagram (Figure 3.14c) to incorporate the magnetic anomaly:

$$(B + \Delta B)^2 = (H + \Delta H)^2 + (Z + \Delta Z)^2 \tag{3.25}$$

and expanding equation 3.25, substituting in equation 3.23, and ignoring the negligible terms in Δ^2, the equation reduces to:

$$\Delta B = \Delta Z \frac{Z}{B} + \Delta H \frac{H}{B} \tag{3.26}$$

Finally, substituting equation 3.24 and the angular descriptions of the geomagnetic element in equation 3.26, the change in the magnetic field is given to a good approximation by Kearey et al. (2013):

$$\Delta B = \Delta Z sinI + \Delta H cosI cos\alpha \tag{3.27}$$

where I is the inclination of the geomagnetic field.
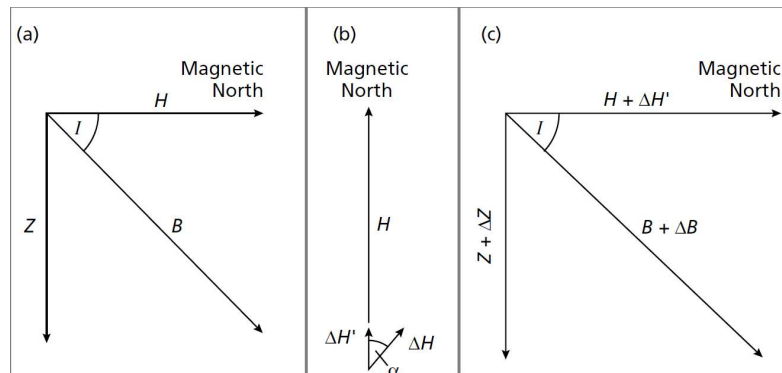
Figure 3.14: The vector presentation of the geomagnetic field (modified from Kearey et al., 2013).

An example of different scenarios for magnetic responses observed on a horizontal surface above a single magnetic dipole source are shown in Figure 3.15. The same scenarios are shown in a profile form in Figure 3.16. The scale of the anomalies depends on the depth z of the dipoles.
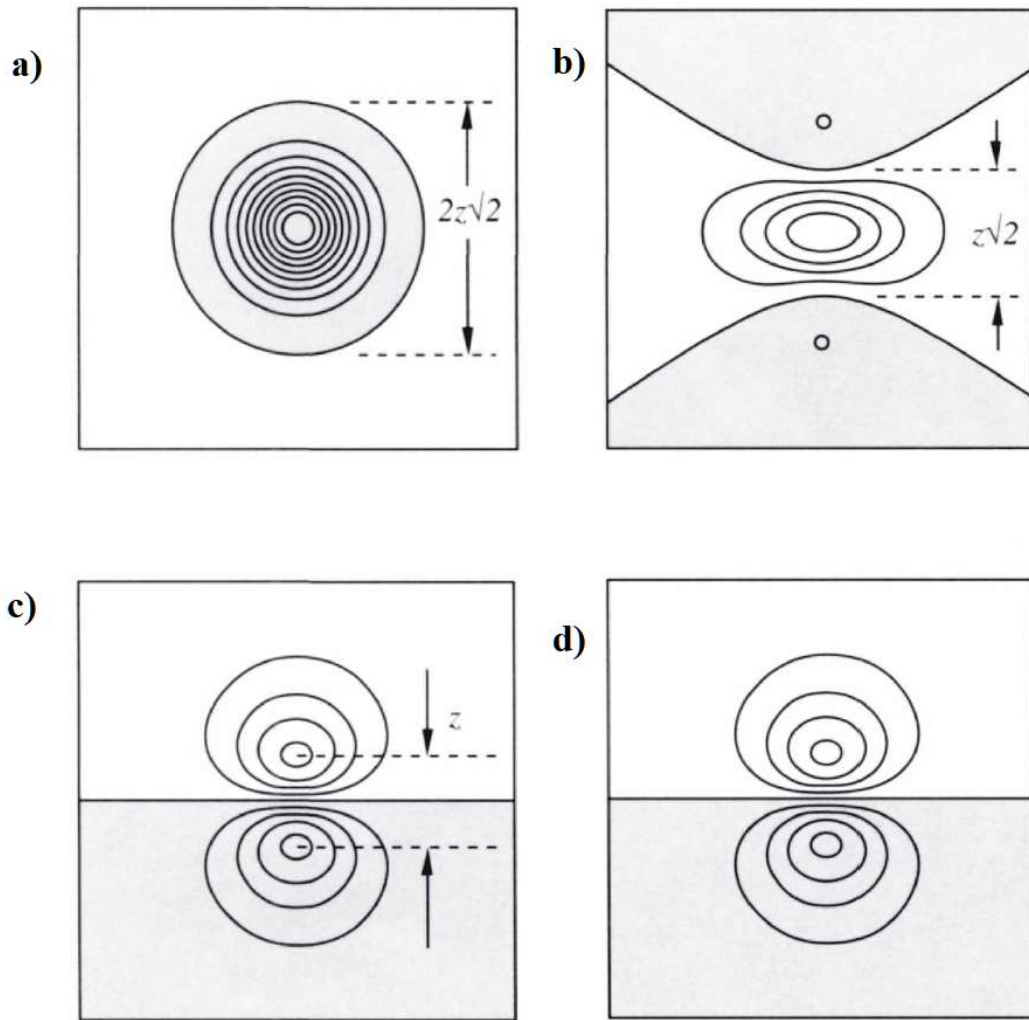
Figure 3.15: The horizontal and vertical components of the anomalous magnetic field measured above horizontal and vertical dipoles. a) Vertical component of B due to vertical dipole; b) horizontal component of B due to horizontal dipole; c) horizontal component of B due to vertical dipole; and d) vertical component of B due to horizontal dipole (Blakely, 1996).
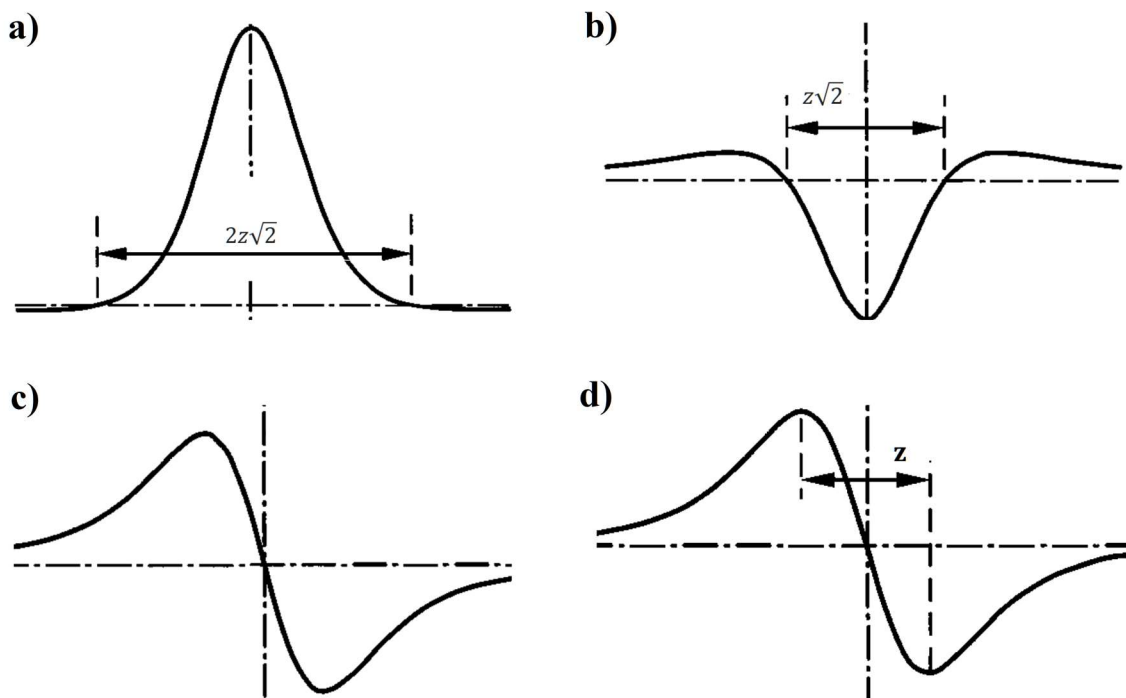
Figure 3.16: The profile form of the magnetic anomaly due to horizontal and vertical dipoles for the scenarios as in panels a-d in Figure 3.15 (modified from Blakely, 1996).

3.2.6 Airborne magnetic surveys

The airborne magnetic survey method is one of the most commonly used airborne geophysical survey methods. This is because magnetic sensors and recording equipment are small and light, thereby easily incorporated into an EM or a gravity gradiometry survey. There are many airborne magnetic survey applications in the oil and mineral exploration fields. Applications of airborne magnetic surveys include near-surface geological mapping, structural geology mapping, aiding 3D geological modeling, groundwater survey, environmental survey, geological hazard assessment, and mineral exploration. However, useful data are achieved only with great care in planning and conducting the survey (Bobrowsky and Marker, 2018).

The preference of a survey aircraft is a trade-off between multiple factors, including flight time, speed, stability, cost-effectiveness, measurement distance from airports, instrumentation, the terrain of the area, and required power characteristics of the aircraft. The latter is particularly significant in situations where the flight altitude is fixed above average terrain to achieve consistency at the altitude above near-surface magnetic sources (Hinze et al., 2013).

Other advancements have been in the increasing load that a drone can carry and the length of time for which it can fly, and in the reduced weight of the sensors and measuring equipment (Walter et al., 2020). The coverage and resolution achieved using unmanned aerial vehicle aeromagnetic surveys, manned airborne, and terrestrial magnetic surveys can provide an advanced data product between the two end-members (Figure 3.17). This is a new development that will prove promising for geophysical and mineral exploration applications, especially in variable terrains.
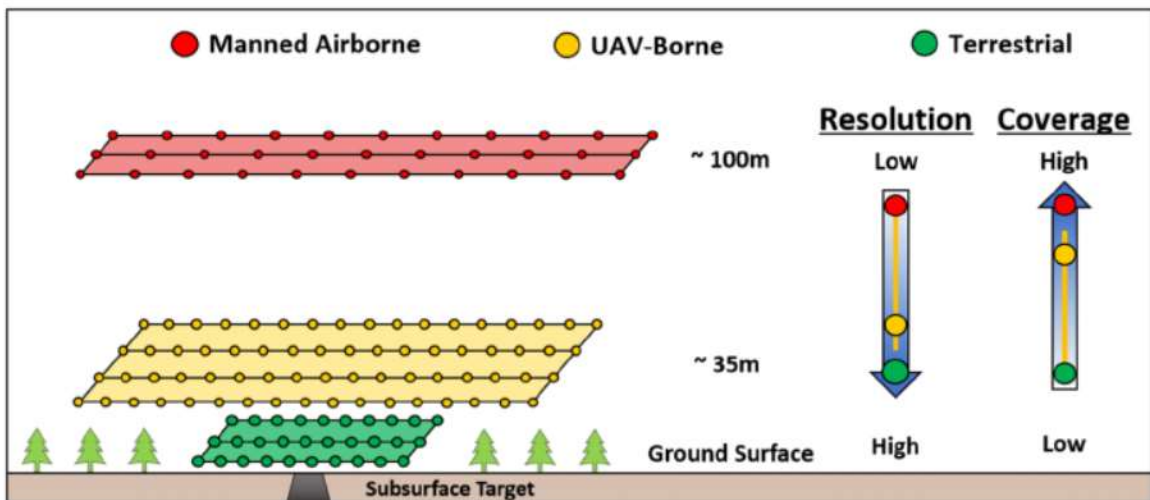
Figure 3.17: The illustration shows the resolution and coverage capabilities of airborne and terrestrial magnetic surveys with a comparison with unmanned aerial surveys (Walter et al., 2020).

4. Geophysical Earth Modeling and Inversion

Three-dimensional Earth models that are mostly used in current geophysical numerical modeling and inversion methods are built on rectilinear meshes due to the ease of computing data responses. In most cases, if an adequately fine discretization is used, arbitrary spatial variations can be represented. However, even though the discretization of the rectilinear mesh may be fine, this type of mesh is always incompatible with geological models involving wireframe surfaces. In order to eliminate this problem for specifying 3D geophysical Earth models, so-called unstructured tetrahedral meshes are used here (Lelièvre et al., 2012). Unstructured tetrahedral meshes can precisely fit the tessellated surfaces in terms of triangles in geological Earth models, which means that a single model is parameterized to allow both geological and geophysical modeling. However, working with unstructured tetrahedral meshes is much more complicated than rectilinear meshes and requires specialized software for generating and manipulating the meshes (Farquharson and Lelièvre, 2017). An example of rectilinear and unstructured meshes is shown in Figure 4.1.
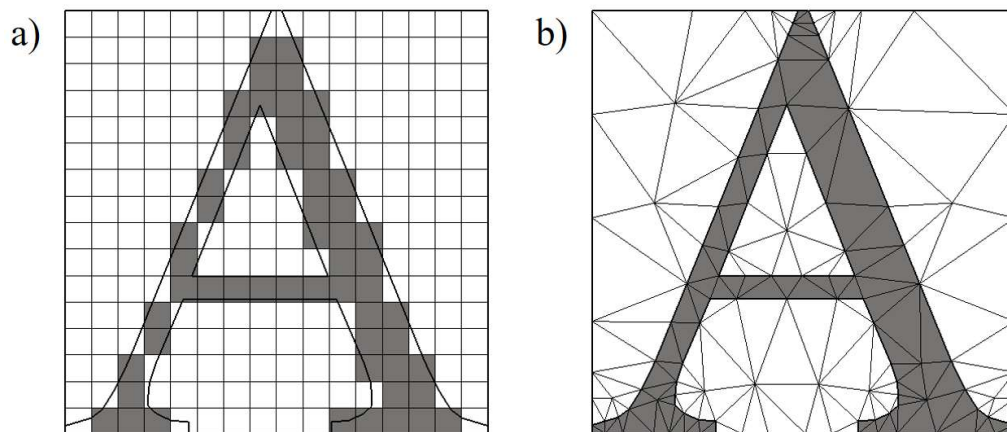
Figure 4.1: An example of (a) a rectilinear mesh, and (b) an unstructured triangular mesh (modified from Lelièvre et al., 2012).

4.1 Generating unstructured tetrahedral meshes

There are several software packages for generating unstructured meshes that are publicly available. In this project, Triangle (Shewchuk, 1996, 2002) was used to generate triangular 2D meshes, and TetGen (Si, 2015) was utilized for generating 3D tetrahedral meshes.

TetGen generates tetrahedral meshes from piecewise linear complexes (PLC). A PLC contains interconnected planar polygonal faces. The meshing algorithm divides these faces into triangles that become the faces of the tetrahedra in the next volumetric mesh. In an exploration geophysics context, a PLC would include the boundary of the modeling volume, the topography surface, any previously known subsurface geological interfaces, and other elements required to divide the modeling volume into different regions (Lelièvre et al., 2012). A PLC is kept in a *poly* file. The poly file is formed of four parts: a list of nodes, a list of facets, a list of holes, and a list of region attributes. The node list contains the minimum number of nodes necessary to identify a PLC. The information about how nodes are combined to create faces, that is facets, is kept in the list of facets. The region attribute list designates different regions in the PPC and can be used to give a numerical identifier to different rock units in a model.

Creating a PLC for a simple model, such as a block, is a straightforward process. For this case, the PLC would comprise of eight nodes defining the corners of the block and six rectangular facets. However, PLCs are difficult to create for geologically realistic models. Therefore, *FacetModeller* can be used. FacetModeller is a Java application designed for efficient manual creation, modification, and analysis of 3D surface-based models for use in numerical modeling. It was developed by Dr. Peter Lelièvre while at Memorial

University of Newfoundland (Dr. Lelièvre is now at Mount Allison University). The application can be publicly obtained (via https://github.com/pglelievre/facetmodeller; Lelièvre et al., 2018).

FacetModeller comprises a 2D working window and a 3D viewer window. Nodes are generated and edited from cross-sections in the 2D working window, and the cross-sections can be in the x, y, or z planes or in arbitrary planes. Also, the nodes on different cross-sections can be connected into triangular facets. The 3D viewer window allows the user to visualize all or part of the model being created (Figure 4.2). The PLC created in FacetModeller can be output in a form that is ready to go into the unstructured tetrahedral mesh generation software.
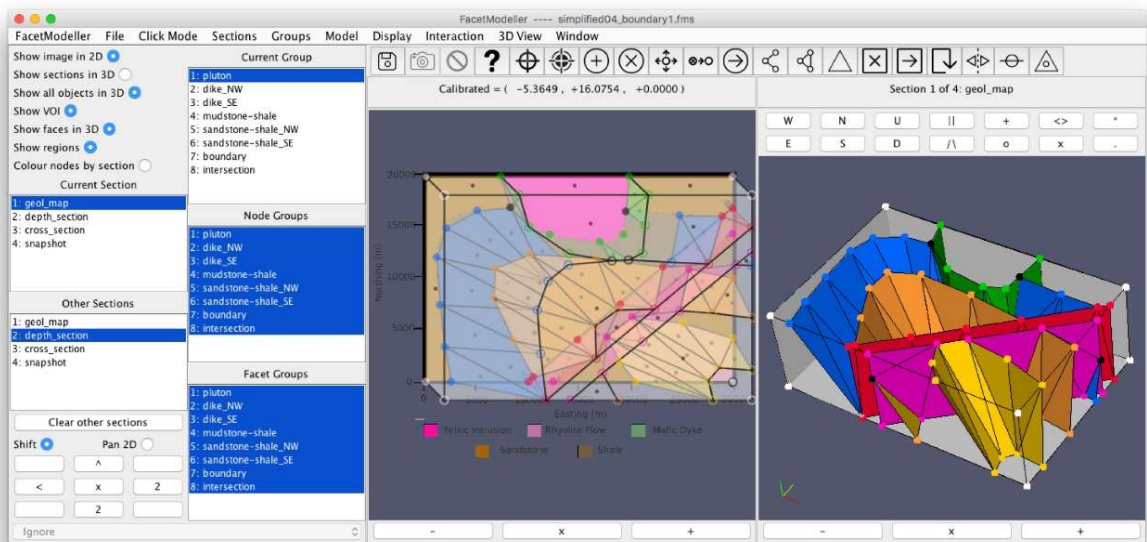
Figure 4.2: A screen capture of the Facetmodeller program for manual creation and modification of the 3D PLC for a geological model (Lelièvre et al., 2018).

TetGen provides several command line switches to generate a mesh depending on the demands of the users (Si, 2015). The *-p* flag is used with the combination of the *-q* or *-a*

flags to generate a quality tetrahedral mesh. The *-q* flag that generates a quality tetrahedral mesh is used for refining the meshes, which increases the quality of meshes and accuracy for the resulting models. Also, the *-q* flag is used for applying a minimum radius edge ratio in the meshes, and the *-a* flag can be applied to assign a maximum tetrahedron volume.

Several authors have developed methods for forward modeling of gravity (Jahandari and Farquharson, 2011), magnetic, seismic (Lelièvre et al., 2011a), DC/IP (Rücker et al., 2006), and EM data (Ansari and Farquharson, 2011) on unstructured tetrahedral meshes. For this project, in addition to Triangle and TetGen, the *PODIUM* software suite is used to prepare data for forward and inversion modeling (see Appendix A) while the *MAGNUM* package is used for running forward modeling and inversion (Lelièvre and Farquharson, 2015; see Appendix B).

4.2 Forward modeling

Geophysical methods are used to study different physical areas affected by the interior of the Earth. Traditional geophysical data interpretation is performed by constructing various geological models and comparing the geophysical data calculated for these models with the observed data. A critical component of this interpretation approach is the process of computing the data for an Earth model. This numerical modeling of geophysical data is usually referred to as *forward modelling* for given model parameters. Forward modeling is used to predict geophysical data for specific geological structures (Zhdanov, 2002).

In order to solve the forward problem, it is presumed that a distribution of the relevant physical property (density for gravity and gravity gradiometry data, susceptibility for

47

magnetic data) within a volume V is the source of the measured physical field (gravity, gravity gradient, or magnetic) above the surface of the earth. The analytical expressions for the gravity gradient for a uniform polyhedral body are given by Okabe (1979). Li and Chouteau, (1998) presented a review of available analytical algorithms for calculating the gravity gradients due to a rectangular prism, polygonal prism, and polyhedron. Also, there are corresponding expressions for the magnetic field due to polyhedron of uniform susceptibility. In this research, the program *FOGO*, which uses the formula for a polyhedron to calculate the gravity gradients or magnetic field due to a tetrahedron, is used to solve the forward problem (Lelièvre and Farquharson, 2015; see Appendix B).

4.3 Minimum-structure inversion

It is a well-known fact that the geophysical inverse problem is non-unique (Farquharson and Oldenburg, 2003). Earth models established by inversion procedures should be consistent with any given a priori information and produce the observations to an admissible degree.

Considering the standard minimum-structure approach to solve an inverse problem: it aims to find the model (m) that minimizes an objective function that comprises a measure of how well the observations are reproduced and a measure of how complicated the model is (Farquharson, 2008):

$$\Phi = \phi_d + \beta \phi_m \tag{4.1}$$

where β is the trade-off parameter that controls the relative importance of the data misfit term (ϕ_d) and the regularization term (ϕ_m) during the minimization process. The data misfit can be defined as a function of:

$$\phi_d = \sum_{i=1}^{N} \frac{(d_i^{cal} - d_i^{obs})^2}{\sigma_i^2} \qquad (4.2)$$

where d_i^{cal} is the ith datum calculated by the inversion, d_i^{obs} is the ith datum from the observed dataset that is provided for the inversion, and σ_i is the uncertainty on the ith datum. ϕ_m is a measure of the structural complexity of the model. The general form of ϕ_m can be written as:

$$\phi_m = \alpha_s \phi_s \left(W_s \left(m - m_k^{ref} \right) \right) + \alpha_t \phi_t (W_t m) \qquad (4.3)$$

where W_s consists of the cell volume information, W_t calculates the model differences between adjacent grid cells; α_s and α_t are constant values that are used to adjust the relative amount of structure in the physical property model during the inversion; ϕ_s is the smallness term, and ϕ_t is the final smoothness term, and m_k^{ref} is a reference model.

The sensitivity of gravity and magnetic data decay with depth, that is, as the distance to the dense or susceptible source in the subsurface increases (Li and Oldenburg, 1996, 1998). There is no inherent depth resolution for either gravity or magnetic data. This problem can be mitigated by presenting a depth or distance weighting. A depth weighting function is appropriate for a situation where the topography is comparatively flat, and only considers the situation that the distance below the observed geophysical data (Li and Oldenburg, 1996):

$$w(z) = \frac{1}{(z_j + z_0)^\beta} \qquad (4.4)$$

where z_j is the depth to the jth cell below the surface, z_0 is the average survey height, and β is a parameter that is used to pair the weighting function to the decay of the signal with depth. Good values of β are typically 2 for gravity and gravity gradiometry data; and for magnetic data β is typically chosen to be 3 (Williams, 2008). A distance weighting function that overcomes the problem where there is a range in topography, and reconciles both lateral and vertical variations in data sensitivity is (Li and Oldenburg, 2000):

$$w(z) = \sqrt{\Sigma \left(\frac{1}{(r_{ij} + r_0)^\beta} \right)^2} \qquad (4.5)$$

where r_{ij} is the distance between cell j and observation i, and r_0 is a small value, such as half the smallest cell dimension (Lelièvre and Farquharson, 2015). The weighting functions are defined in the cell volume information (W_s) which is a diagonal matrix that contains user-defined smallness weights such as depth, distance or sensitivity.

The iteration procedure of the inversion code, which attempts to solve the inversion using different values of the trade-off parameter (β), will be completed when a good fit is obtained between the observed and calculated data. This means that "omega (w)", which is equal to data misfit (ϕ_d) divided by target misfit (ϕ_d^*), would be between 0.95-1.05. Therefore, *normalized data residual* should ideally be close to zero on average:

$$\text{Normalized data residual} = \frac{d_i^{cal} - d_i^{obs}}{\sigma_i} \qquad (4.6)$$

As well as the normalized residuals being close to zero, the desired range for them lies between -1 and +1. In order to obtain a better fit, the value of "*chifact*" can be adjusted by a user before running an inversion (Lelièvre and Farquharson, 2015):

$$\text{chifact} = \frac{target\ misfit\ (\phi_d^*)}{number\ of\ data\ (N)} \tag{4.7}$$

4.4 Joint inversion

An inversion for a single physical property from a single data-set may encounter difficulties if the geology is complicated. Thus, inverting two different data-sets for two different physical properties (e.g., density, susceptibility, etc.) can assist and improve the solution of a single, common Earth model. This process is known as *joint inversion*. The objective function for joint inversion with two data-sets can be written as (Lelièvre et al., 2012; Lelièvre and Farquharson, 2015):

$$\Phi(m_1, m_2) = \lambda_1 \phi_{d1}(m_1) + \lambda_2 \phi_{d2}(m_2) + \alpha_1 \phi_{m1}(m_1) + \alpha_2 \phi_{m2}(m_2) + \Phi_j(m_1, m_2) \tag{4.8}$$

where λ_1 and λ_2 are the trade-off parameters that multiply the data misfit terms (ϕ_{d1}, ϕ_{d2}) and try to fit both data-sets, each to a good target value, during the inversion, and Φ_j is the joint coupling term. The coupling term Φ_j is a quantity that measures the dissimilarity between the models, and it gets larger when the models are not similar to each other (Lelièvre et al., 2012).

There are several measures of model similarity that can be chosen for joint inversion to couple the recovered models. For this study, correlation coupling and fuzzy coupling are considered.

Correlation coupling evaluates the linearity of the relationship between two sets of values. It does not require a knowledge of the anticipated range for the physical properties being considered, and is commonly used for image matching (Lelièvre et al., 2012):

$$\Psi_2(r,s) = \left(\frac{\sum_{i=1}^{M}(r_i-\mu_r)(s_i-\mu_s)}{M\sigma_r\sigma_s} \pm 1\right)^2 \tag{4.9}$$

where μ_r and σ_r denote the mean and standard deviation of r (similar definitions for μ_s and σ_s). It can be defined either a positive or negative linear correlation between the physical properties by choosing the negative or positive sign in equation.

Fuzzy coupling, on the other hand, is used to specify different clusters in physical property space, rather than along a process as assumed by the two measures above. Fuzzy coupling might suffer from multiple local minima, hence should be utilized carefully. The resulting joint measure is given by Lelièvre et al. (2012):

$$\Psi_3(r,s) = \left(\sum_{i=1}^{C}\sum_{k=1}^{M}\omega_{ik}^{f}z_{ik}^{2}\right) \tag{4.10}$$

where C is the number of clusters and the exponent f is usually set to a value of 2.0. The membership weight (ω_{ik}) interrelates the model parameter set for the kth cell to the ith cluster (Lelièvre et al., 2012).

There are several steps required to prepare data and mesh for an inversion. These steps are as follows (Williams, 2008):

- Defining the problem;
- Determining the depth, width, and length of the desired mesh;
- Specifying the data area;

- Generating a tetrahedral mesh to match the resolution of the data, the desired resolution of the recovered model, and available computing power;

- Padding the mesh with a buffer of additional cells to avoid boundary effects where anomalies are located near the edge of the mesh;

- Calculating and removing the regional data trend that accounts for the contributions to the response from all sources located outside the region of interest.

For this project, the VIDI inversion program, written based on a minimum structure inversion algorithm, is used to perform both single and joint inversion problems. (Lelièvre and Farquharson, 2015; Appendix B).

5. Inversion of Budgell Harbour Gravity Gradiometry Data

The main goal of this project was to perform typical unconstrained, minimum-structure inversion on the airborne gravity gradiometry data over the Budgell Harbour area, with secondary goals of inverting the aeromagnetic data and jointly inverting these two data-sets (Figure 2.2). The Earth model was parameterized in terms of unstructured tetrahedral meshes (Section 4.1; see Appendix A), which allowed the topography information (Figure 2.4) from the survey area to be modeled accurately. The 3D density and susceptibility models of the area constructed by these inversions offer the possibility to assess further the mineral potential of the area and to better delineate the Budgell Harbour gabbro intrusion.

5.1 The airborne gravity gradiometry data

The data acquisition was contracted by Celtic Minerals Ltd. and flown by Bell Geospace Inc. in 2007 using their Air-Full Tensor gradiometry (FTG) system over the Budgell Harbour property. For this thesis, the data-set was obtained from the Newfoundland and Labrador Geological Survey. The line spacing was 200 m, and a total of 407 km of survey lines were flown roughly in the north-south direction. The planned flight height was at 80 m altitude; however, due to topography variations, the flight altitude varied from approximately 70 m to 265 m. Tie lines were flown in an east-west direction at a line spacing of 2000 m (Figure 5.1). A left-handed coordinate system was used during the acquisition (x-Easting, y-Northing, z+ upward). The data processing was completed by Bell Geospace using their processing routines and corrections (Stuckless, 2008). The dataset was

de-noised, leveled, and terrain corrected using a density of 2.70 g/cm^3. Maps of the components available in the data-set (*Txx, Txy, Txz, Tyy, Tyz and Tzz*) are shown in Figure 5.2.

As previously discussed (Section 3.1.6.2), different information about the geological features of the subsurface is given by the different tensor components (Figure 5.3). The vertical component of the gravity gradient, *Tzz*, is most obviously related to subsurface geology, and in this case delineates approximately the 4km wide Budgell Harbour Stock (BHS) intrusion. The *Txx* and *Tyy* components indicate the edges of the intrusion in the east-west and north-south directions. The *Txy* component indicates the BHS with two positive and two negative lobes (positive to the NE and SW, negative to the NW and SE). The *Tyz* and *Txz* components show the central axes of the BHS intrusion in the north-south and east-west directions (Mataragio and Kieley, 2009).

Figure 5.1: The observation points along the flight lines over the Budgell Harbour Stock. The blue dots show the locations at which data were available, and the black horizontal lines in the east-west direction indicate the tie lines.
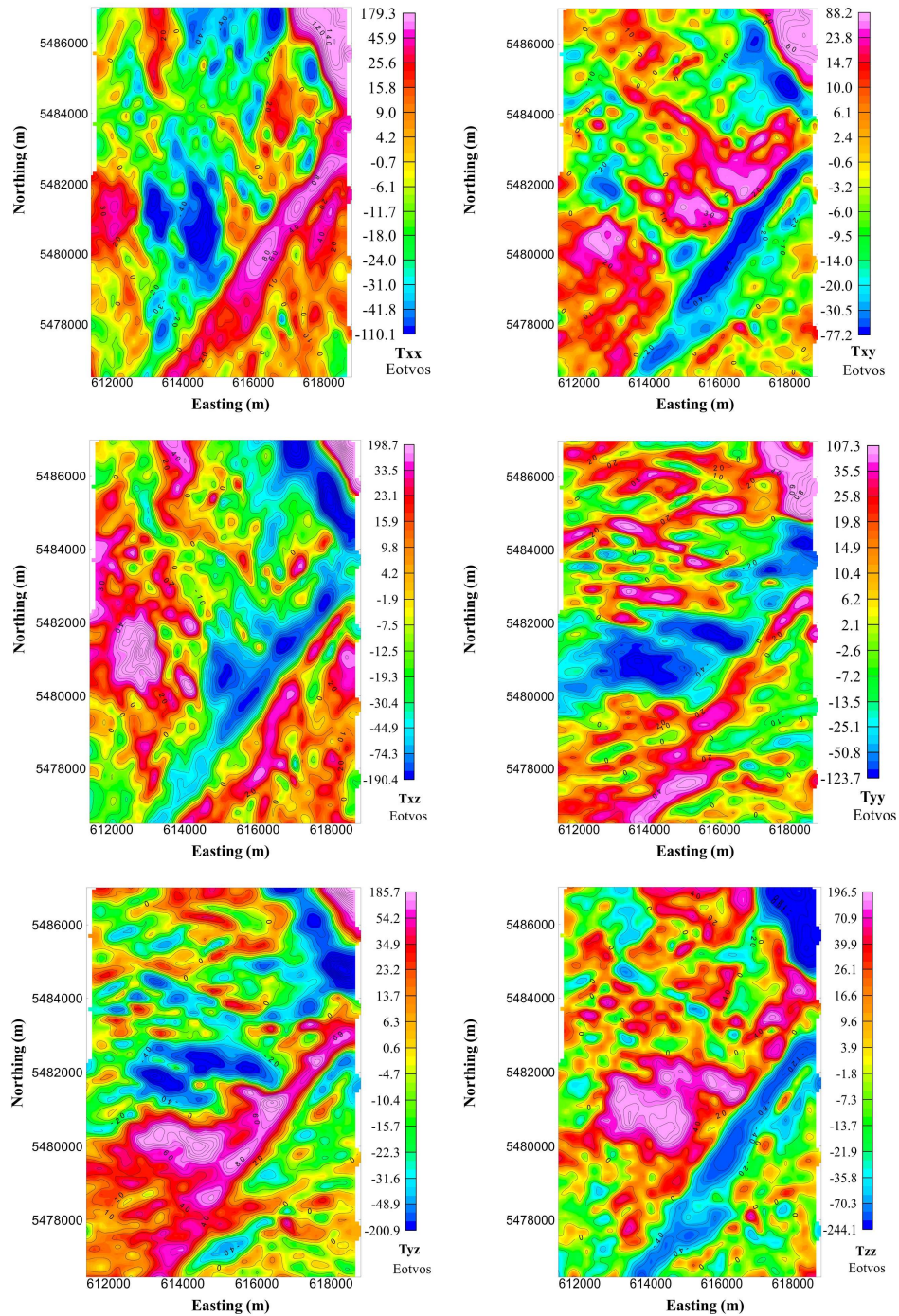
Figure 5.2: The terrain corrected airborne gravity gradiometer data observed above the Budgell Harbour Stock. These maps were generated using Oasis Montaj with a grid cell size of 200 m. The contour interval is 10 E for *Txx, Txy, Txz, Tyy, Tyz,* and 20 E for *Tzz*.
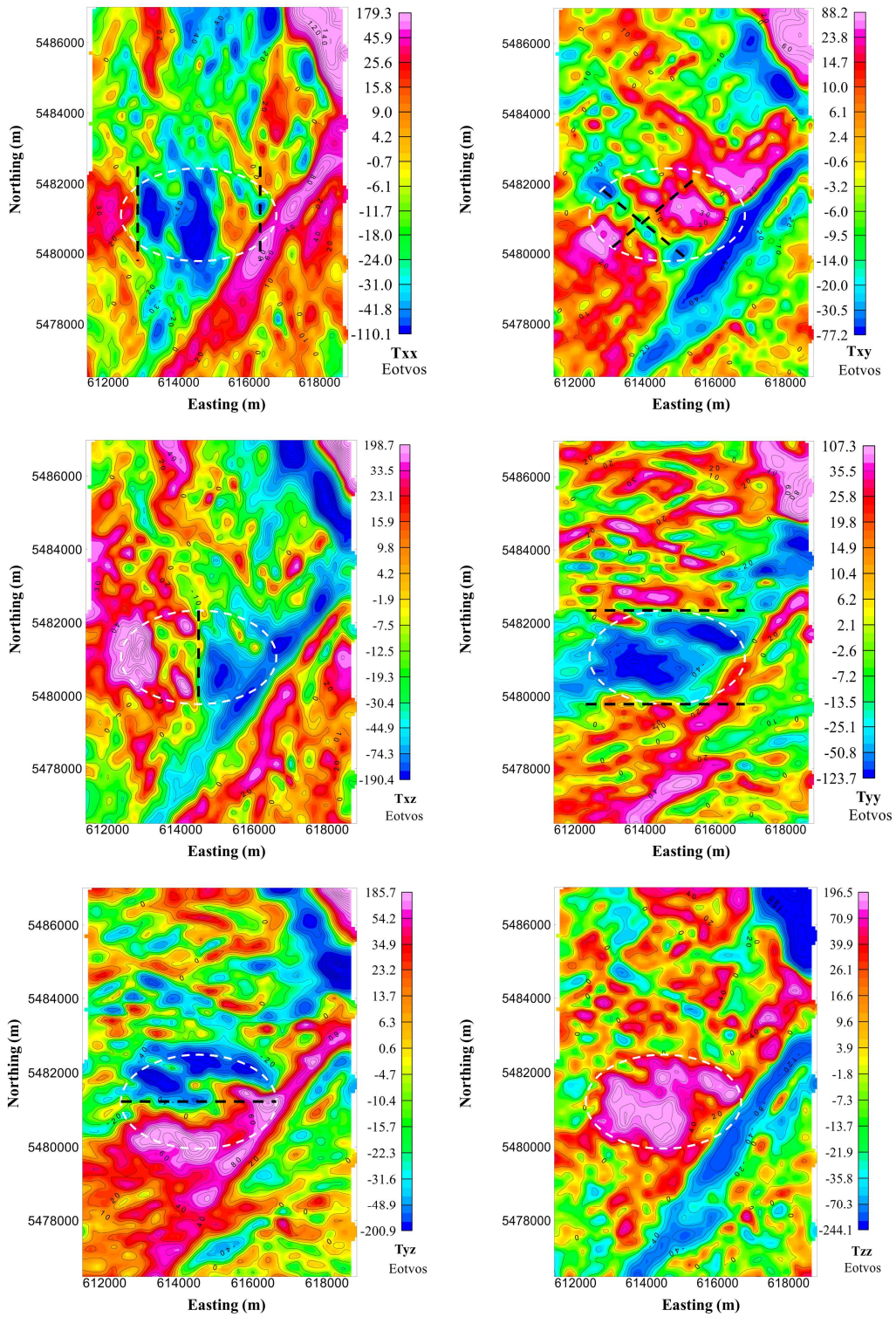
Figure 5.3: The observed airborne gravity gradiometry data with different attributes of the

Budgell Harbour Stock indicated by the white and black dash lines.

5.2 Initial model building for inversion

As previously discussed (Section 4.4), a number of steps are required for an inversion, such as determining the data area and generating a tetrahedral mesh with which to parameterize the Earth model. The core volume of interest (COI) was determined by the location and size of the highest observed *Tzz* gravity gradient anomalies from the survey area in which the BHS intrusion is located (Figure 5.4), with the COI arranged so that the BHS is roughly at its centre. The subset data in the COI was selected to perform inversions (Figure 5.5).
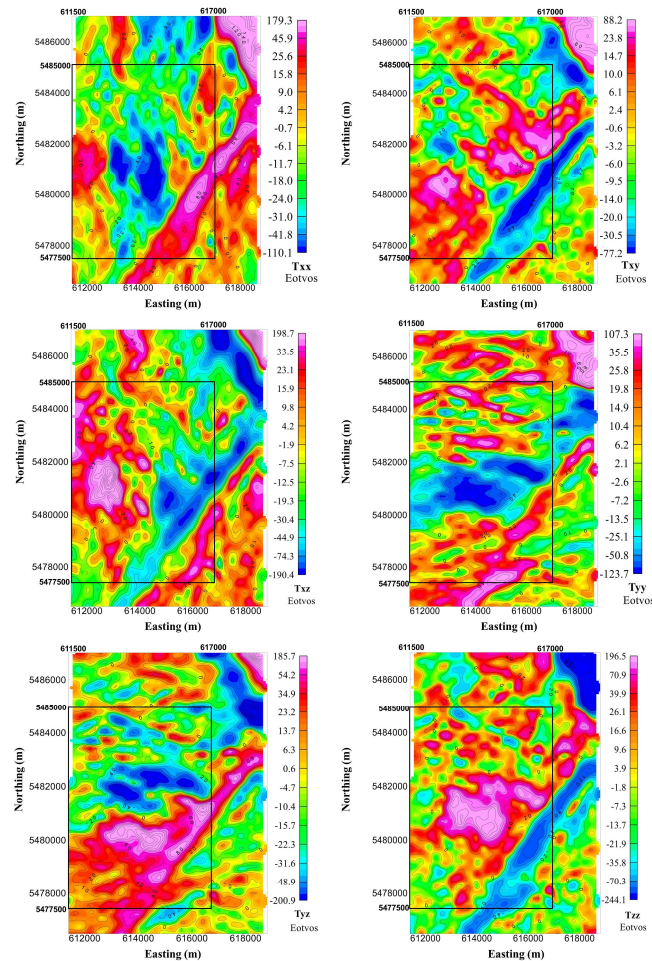
Figure 5.4: The observed airborne gravity gradiometry data above the Budgell Harbour Stock property and the black rectangular boxes showing the COI area.
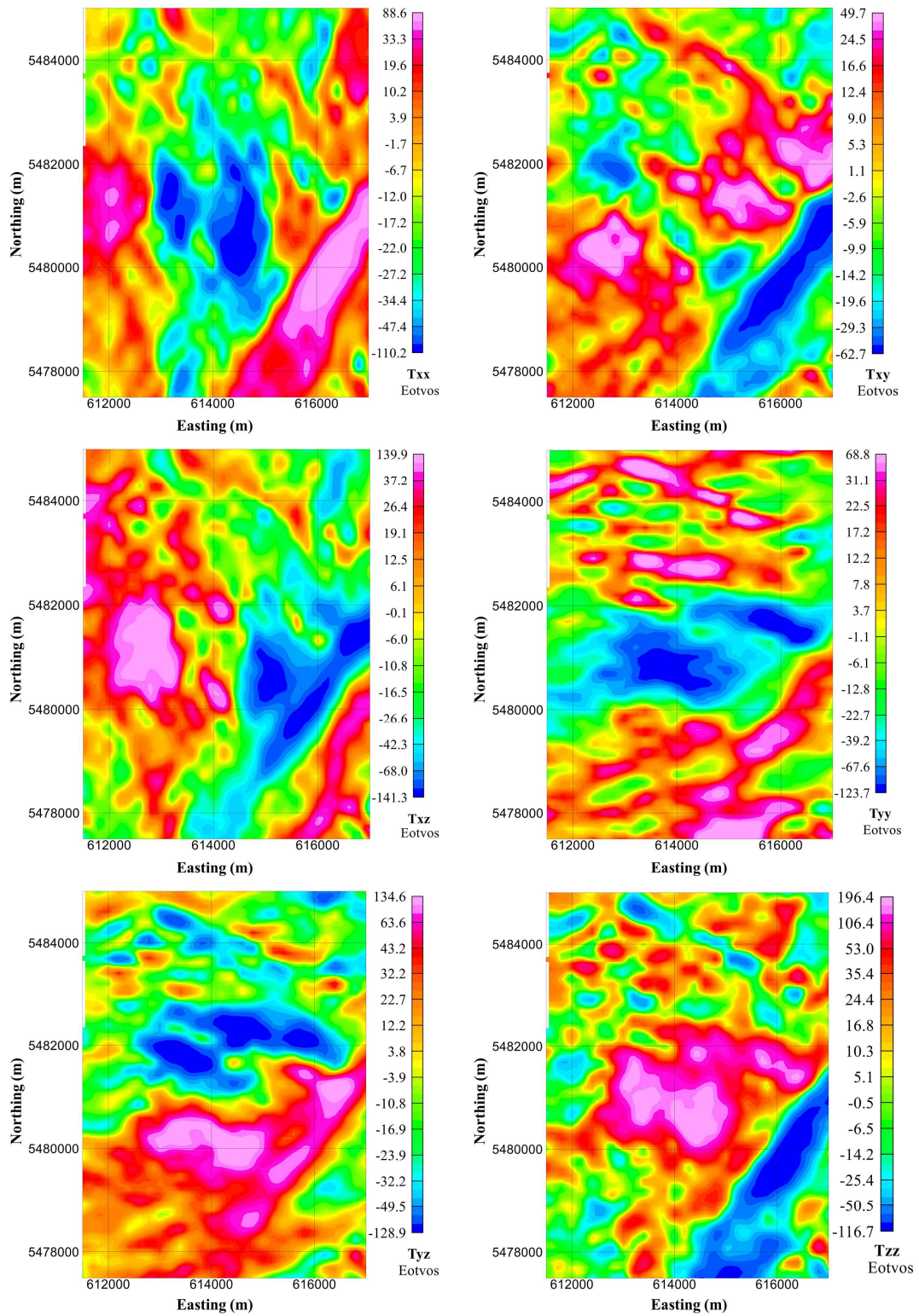
Figure 5.5: Maps (gridded using Oasis Montaj) of the subset of airborne gravity gradiometry data that were used for the inversions.

The *PODIUM* software was used for generating the mesh to be used for the inversions (see Appendix A). The mesh had dimensions of 10,500 m by 12,500 m by 13,000 m (Easting by Northing by depth); and the COI area was 5500 m by 7500 m by 5000 m. The topography information (Figure 2.4) was incorporated into the mesh, resulting in 58711 nodes and 117,269 triangles. A quality unstructured mesh (see Section 4.1) was generated using *TetGen* ($q = 2$ and $a = 2,250,000$). The total number of tetrahedral cells was 226,696, with 186,042 going into the COI modeling area. Several different views of the mesh are shown in Figure 5.6 to Figure 5.9.
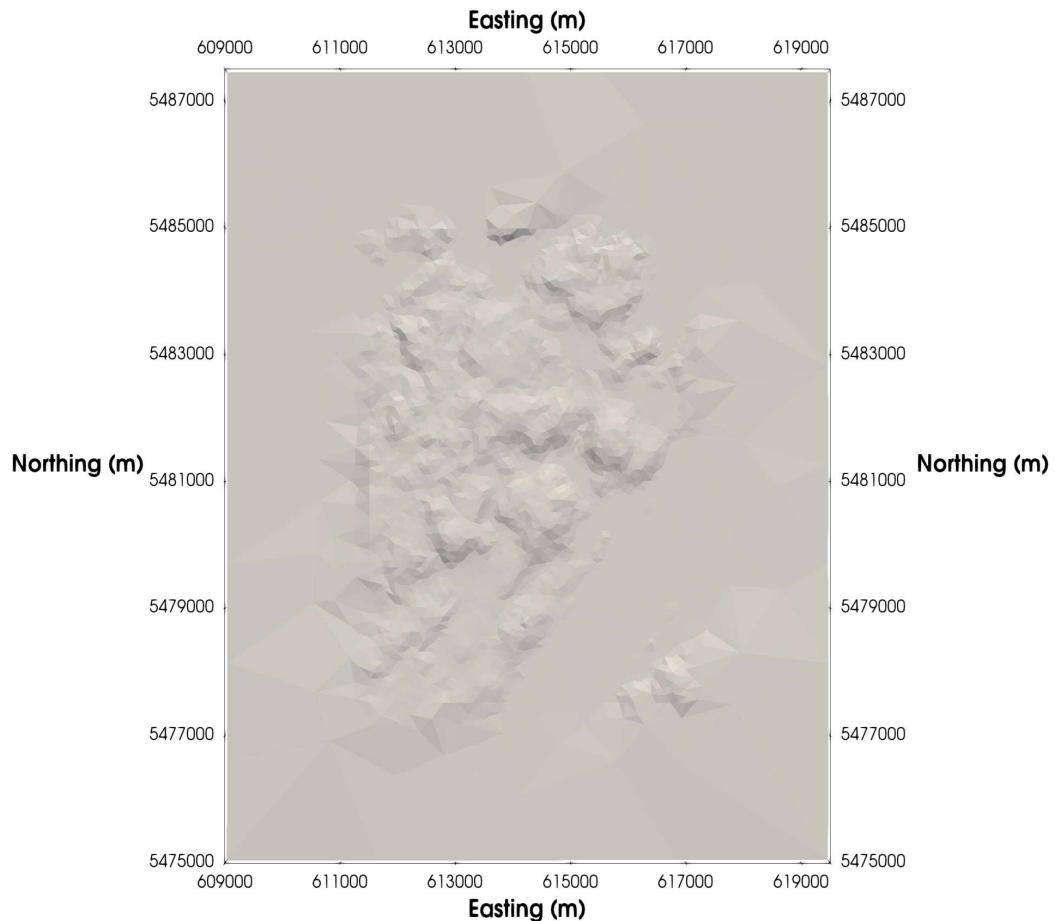
Figure 5.6: A top view of the whole mesh used for the inversions. The topography, which can be seen by the shading used in this image, was included in the COI.
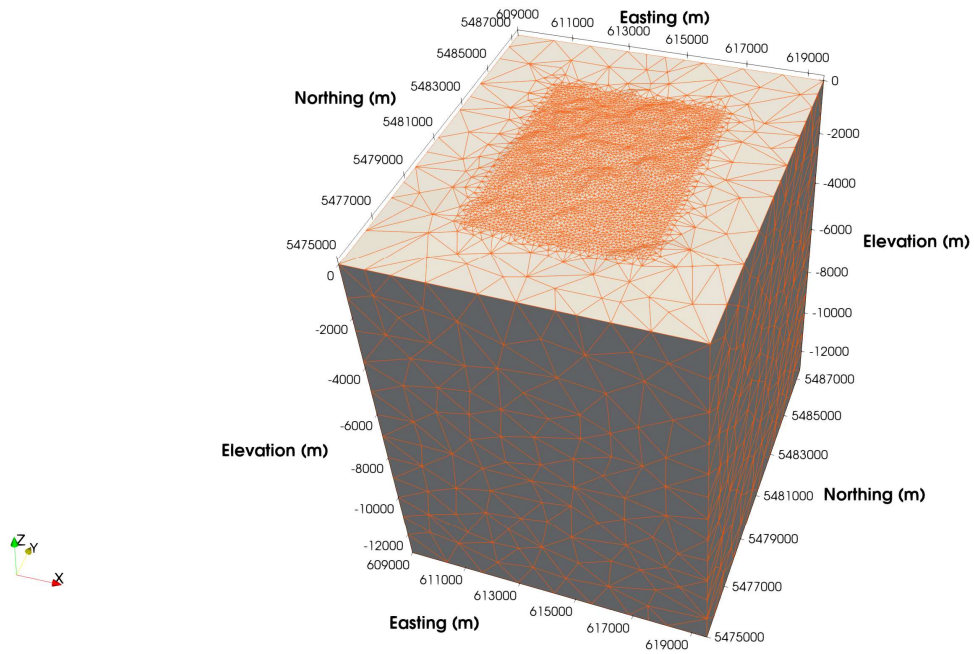
Figure 5.7: A view of the whole mesh showing the edges of the tetrahedral cells on the outer boundaries of the mesh.
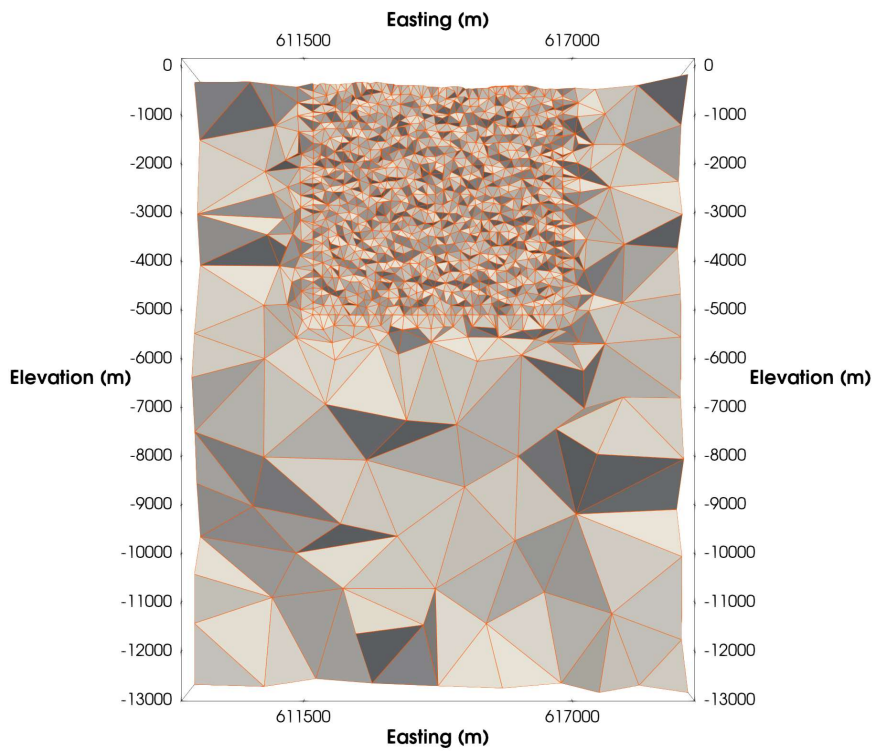
Figure 5.8: An inside view of the mesh showing the COI area (where the mesh is refined).
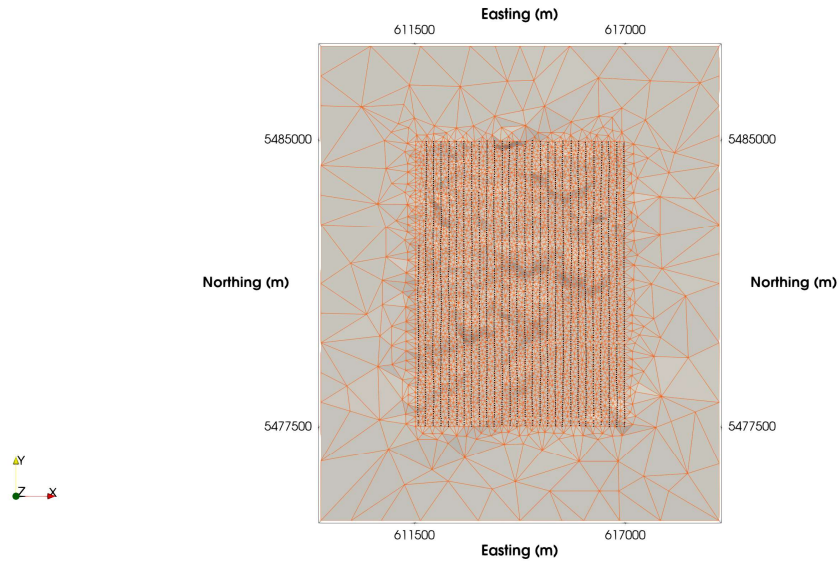
Figure 5.9: A top view of the mesh showing the edges of the tetrahedral cells on the top of the mesh and the observation locations (black dots).

5.3 Inversion results

The commonly discussed *Tzz* component inversion is enough to produce geologically interpretable results; however, including additional components can increase the resolution of the recovered density model (Martinez et al., 2013). Inverting different components, individually and in combinations, was therefore investigated here. A number of tests were carried out to select the ideal *chifact* values for the inversions. Values of 1.0 for the single-component inversions (see Appendix C) and 2.0 for all the combined components inversions were found to give the best results because of the match between the observed and predicted data, as shown in the following sections. The number of data that went into each inversion was equal to the number of components considered times 3510 (the number of observation locations). The default measurement uncertainty (2%) was used for all inversions. The data that went into the inversion were the processed data at the actual

observation locations along the flight lines (see Section 5.1 and Figure 5.1). The reference density in the inversions was 0 g/cm^3; therefore, no assumptions were made about the geologic features in the model, and the inversions were thus unconstrained. The distance weighting was used for all inversions with $\beta = 2.0$ and $r_0 = 22.0$ (Equation 4.7).

5.3.1 Single-component *Tzz* inversion

The single-component *Tzz* inversion is considered as a base model to compare to, with the addition of more components possibly increasing the quality of the model (Martinez and Li, 2011). As mentioned above, the *chifact* value was set to 1.0. The value of *omega* (the achieved misfit normalized by the target misfit; see Equation 4.9) was 1.01 when the inversion completed (see Section 4.3.1). The inversion took 6 hours using 24 cores on one node of the Torngat computer cluster, corresponding to a total of 155 CPU hours. The calculated values of *Tzz* for the constructed model are shown in Figure 5.10(a). The normalized data residuals are shown in Figure 5.10(b). The average normalized data residual was 3.15 x 10^{-5}, and the standard deviation of the normalized residuals was 1.008.

Cross-section and threshold views of the recovered model are shown in Figure 5.11. The recovered model density contrast ranges from -1.214 to $+1.404$ g/cm^3. As anticipated, the large, deep, centrally located dense anomaly, which dips slightly to the north, corresponds to the Budgell Harbour Stock (BHS). The foot-like density anomaly at the base of the main density anomaly is possibly an artefact that is trying to fit a regional trend in the data.

In addition to the single-component inversion of *Tzz*, the other five components were inverted independently (see Appendix C).
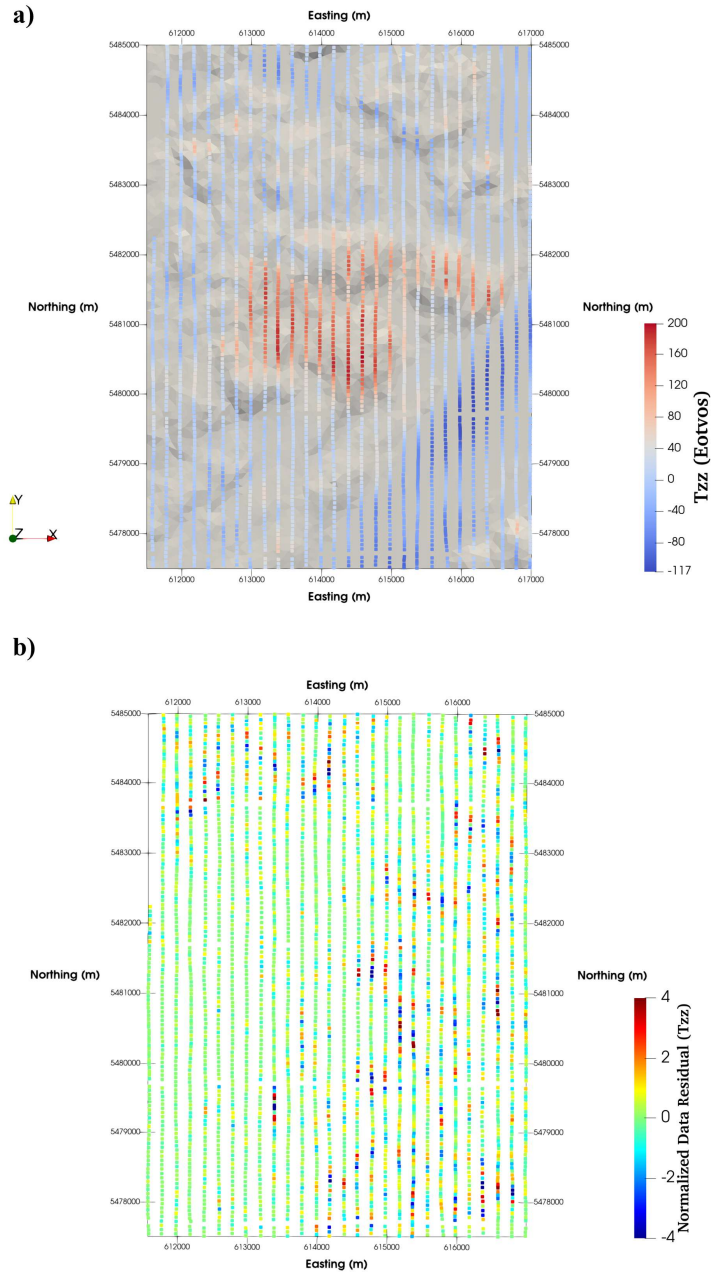
Figure 5.10: a) The calculated data of the Tzz component (displayed as data-points along the survey lines over the shaded-relief topography). b) The normalized data residuals for the *Tzz* component. (Paraview software was used for plotting.)

Figure 5.11: a) A view of the central part of the recovered model for the *Tzz* single-component inversion result looking from southwest to north. b) A view from southeast to north. c) A threshold view of the recovered model with all cells with densities below 0.40 g/cc removed for clarity.

5.3.2 Three components *Txz, Tyz & Tzz* inversion

From the inversion of the *Tzz* component, it can be seen that this component of the gravity gradient data with the given acquisition parameters can image the presence and general structure of the BHS. However, combining additional gradient data components with *Tzz* in an inversion can provide more lateral resolution of the inverted density contrast model (Martinez et al., 2013).

A *chifact* value of 2.0 was provided to the inversion. An *omega* value of 1.03 had been reached when the inversion terminated. The inversion was completed in 7 hours. The total number of data points for this inversion was 10,530. The average normalized data residual was -2.47 x 10^{-5}, and the standard deviation calculated from the normalized residuals were 1.456 for the *Txz* component, 1.334 for the *Tyz* component, and 1.524 for the *Tzz* component.

Two cross-section views and a threshold view of the recovered model are shown in Figure 5.12. The recovered model density contrast ranges from -1.308 to $+1.295$ g/cm^3. As with the single-component *Tzz* inversion, the model shows a similarly large, deep, dense body dipping in the same direction as for the *Tzz* single-component inversion. The lateral boundaries of the dense body are slightly better defined as the density anomaly is narrowed, and the dip is more pronounced compared to the model constructed by the *Tzz* single-component inversion (Figure 5.11).

Figure 5.12: a) A view of the central part of the recovered model for the *Txz,Tyz,Tzz* combined-components inversion looking from southwest to north. b) A view of from southeast to north. c) A threshold view of the recovered model with all cells below 0.40 g/cc removed for clarity.

5.3.3 Curvature components *Txx, Txy & Tyy* inversion

As discussed previously (Section 5.1), the *Txx* and *Tyy* components delineate the edges of the intrusion in the east-west and north-south directions respectively, and *Txy* outlines features that are oriented at an angle to the north-south direction. The combined inversion of curvature gradient components (*Txx, Txy, Tyy*) has been found to provide better results than the combined inversion of horizontal (*Txz* and *Tyz*) and vertical gradient (*Tzz*) components (Geng et al., 2014). An inversion only using the curvature gradient components was therefore considered here. As in the previous sub-section, the inversion had 10,530 data points. The *chifact* value was 2 and the final value of *omega* reached was 1.04. The inversion was completed in 6 hours. The average normalized residual was -9.281 x 10^{-5}, and the standard deviation calculated from the normalized residuals were 1.272 for the *Txx* component, 1.291 for the *Txy* component, and 1.719 for the *Tyy* component. The cross-section views and threshold view of the recovered model are shown in Figure 5.13. The recovered density contrast ranges from -1.349 to $+1.225$ g/cm^3.

The features have a lower maximum density contrast when compared to the *Tzz* inversion result. The centrally located dense feature that corresponds to the BHS intrusion is more compact, being significantly narrower compared to the *Tzz* model. Thus, the combined inversion of the curvature gradient components (*Txx, Txy, Tyy*) can be effective at delineating the edges of a body. However, in contrast to Geng et al. (2014), the combined inversion of curvature gradient components (*Txx, Txy, Tyy*) does not give a better result than the combined inversion of inverting the three *Txz, Tyz, Tzz* gravity gradient components.
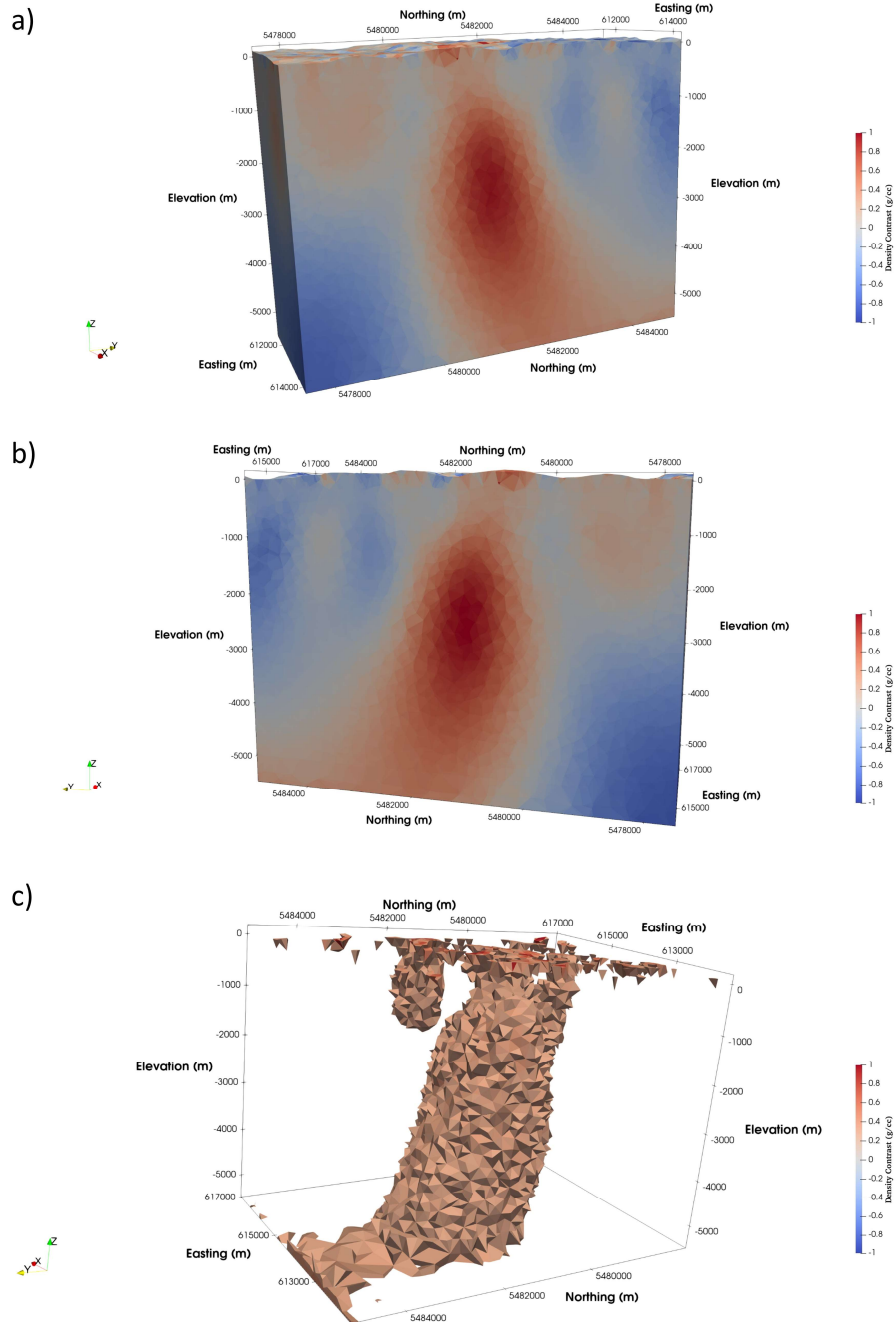
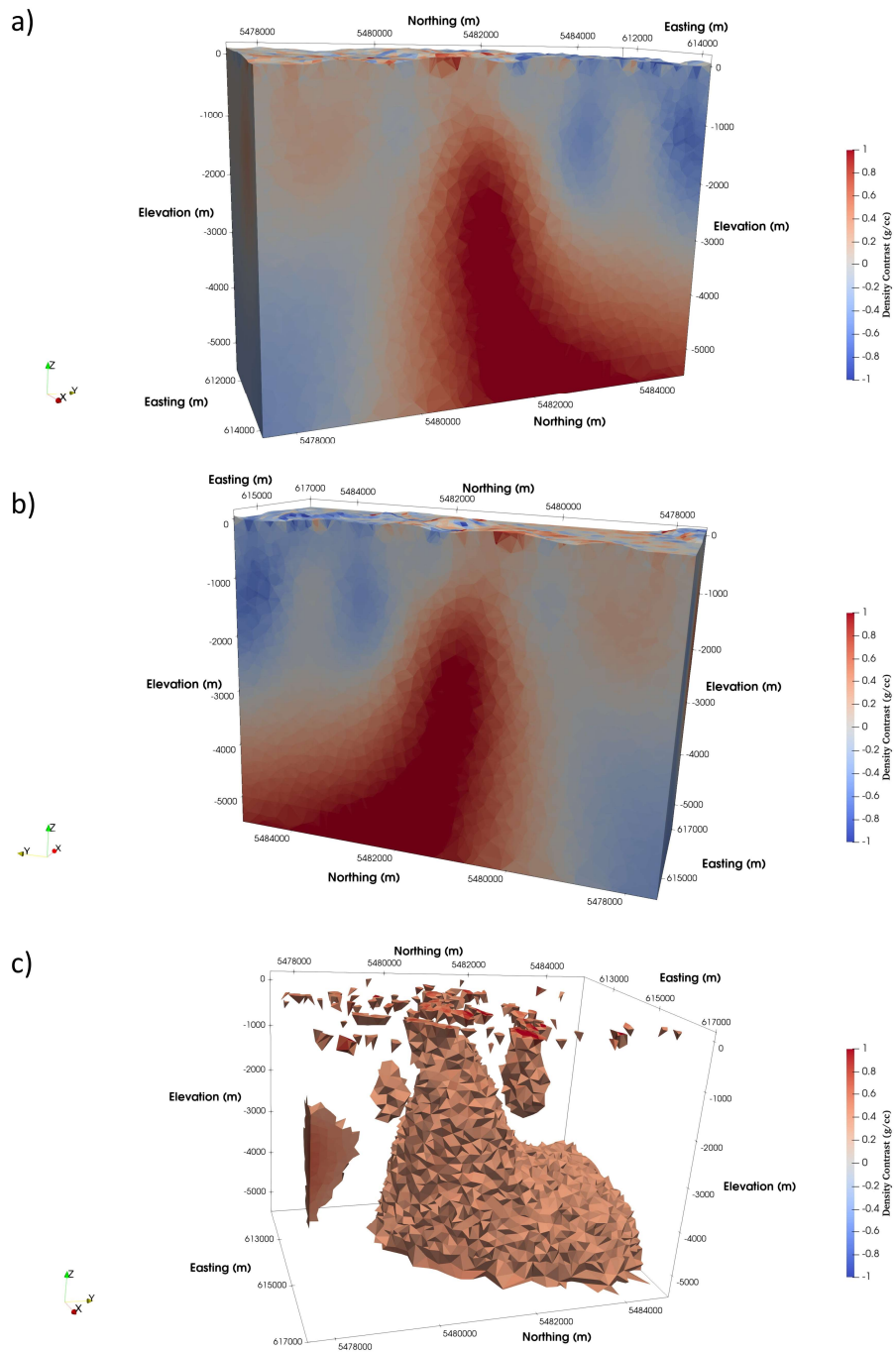Figure 5.13: a) A view of the central part of the recovered model for the *Txx,Txy,Tyy* combined-components inversion results looking from southwest to north. b) A view from southeast to north. c) A threshold view of the recovered model with all cells below 0.40 g/cc removed for clarity.

5.3.4 Five components *Txx, Txy, Txz, Tyy, Tyz* inversion

Five components were combined to evaluate the utility of inverting all independent components. It was thought that the overall density model will be improved with all available information at each observation location included in the inversion. The inversion had 17,550 data points. The inversion took 27 hours. The final value of *omega* was 1.02 for this inversion. The average normalized data residual was 5.41 x 10^{-5}, and the standard deviation calculated from the normalized reisudals were 1.337 for the *Txx* component, 1.056 for the *Txy* component, 1.585 for the *Tyy* component, 1.493 for the *Tyy* component, 1.620 for the *Tyz* component.

The cross-section views and threshold view of the recovered model are shown in Figure 5.14. The recovered density contrast ranges from -1.180 to $+1.302$ g/cm^3. The resulting model is most similar to the *Txz*, *Tyz*, *Tzz* model but has a higher maximum density contrast. There is a clear second dense feature that is smaller and shallower, and a third dense feature in the south-west corner that is similar in size compared to the *Txz, Tyz, Tzz* model. Also, the result of the combined five components inversion reinforces the idea that the BHS is approximately 4 km wide (Mataragio and Kieley, 2009). Furthermore, the deep density anomaly resembling a foot at the bottom of the main anomaly is present again (see Figure 5.11). This feature is probably an artefact rather than real deep structure. Although the time required to wait for the combined five-components inversion result was approximately 4 times that for the single-component and three-component inversions, the combined five-components inversion increased the interpretable quality of the resulting model compared to the single and three-component inversion results (Figures 5.15 and 5.16).
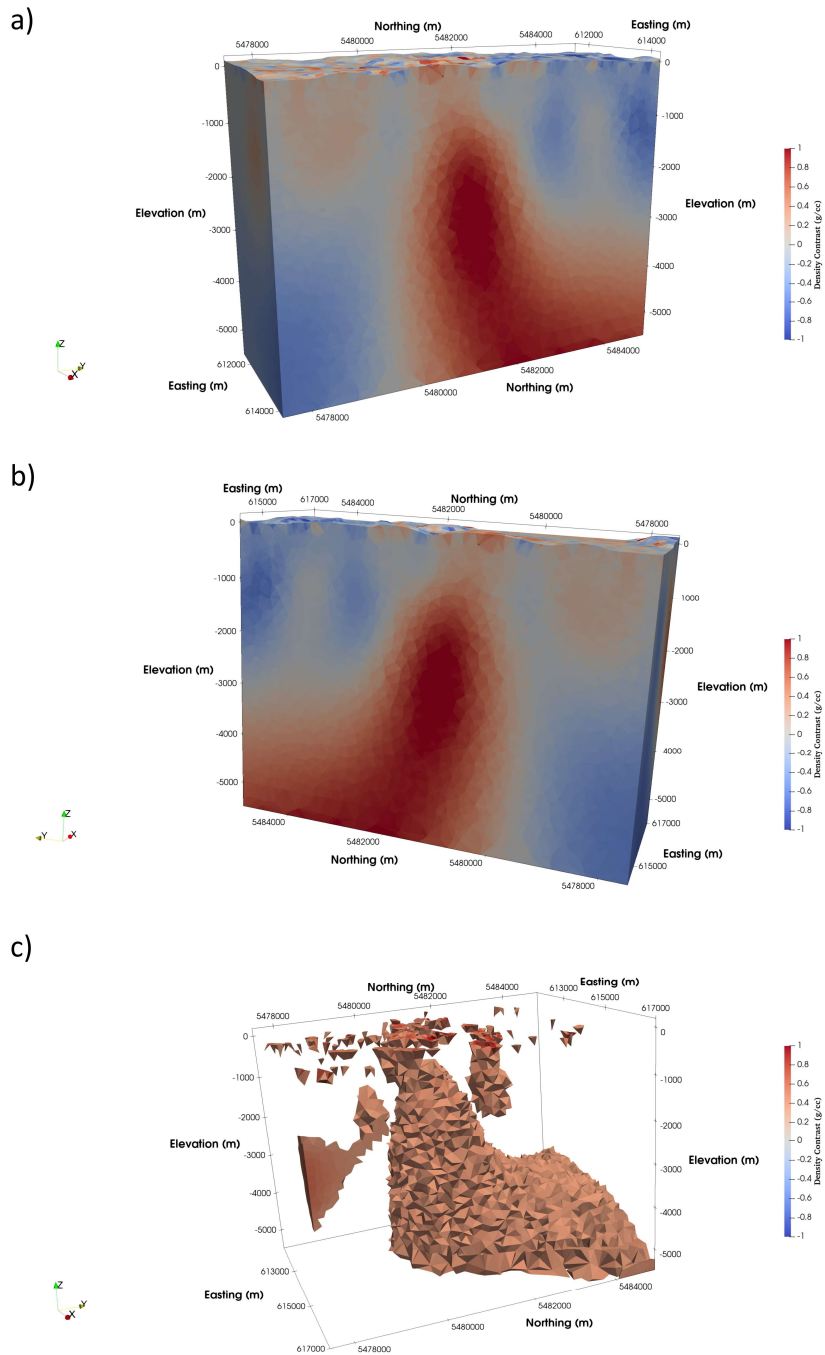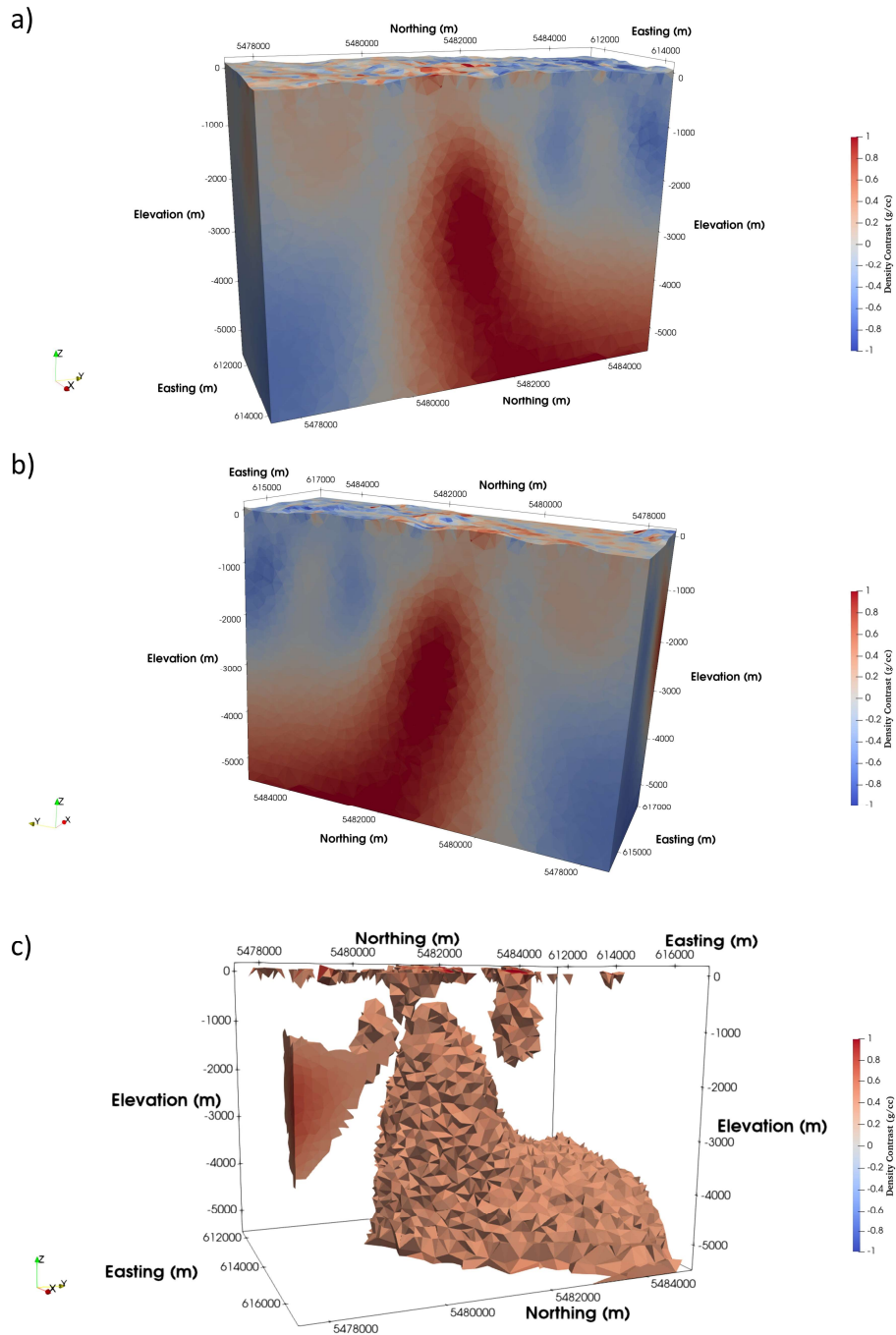
Figure 5.14: a) A view of the central part of the recovered model for the *Txx,Txy,Tyy,Txz,Tyz* combined-components inversion looking from southwest to north. b) A view from southeast to north. c) A threshold view of the recovered model with all cells below 0.40 g/cc removed for clarity.
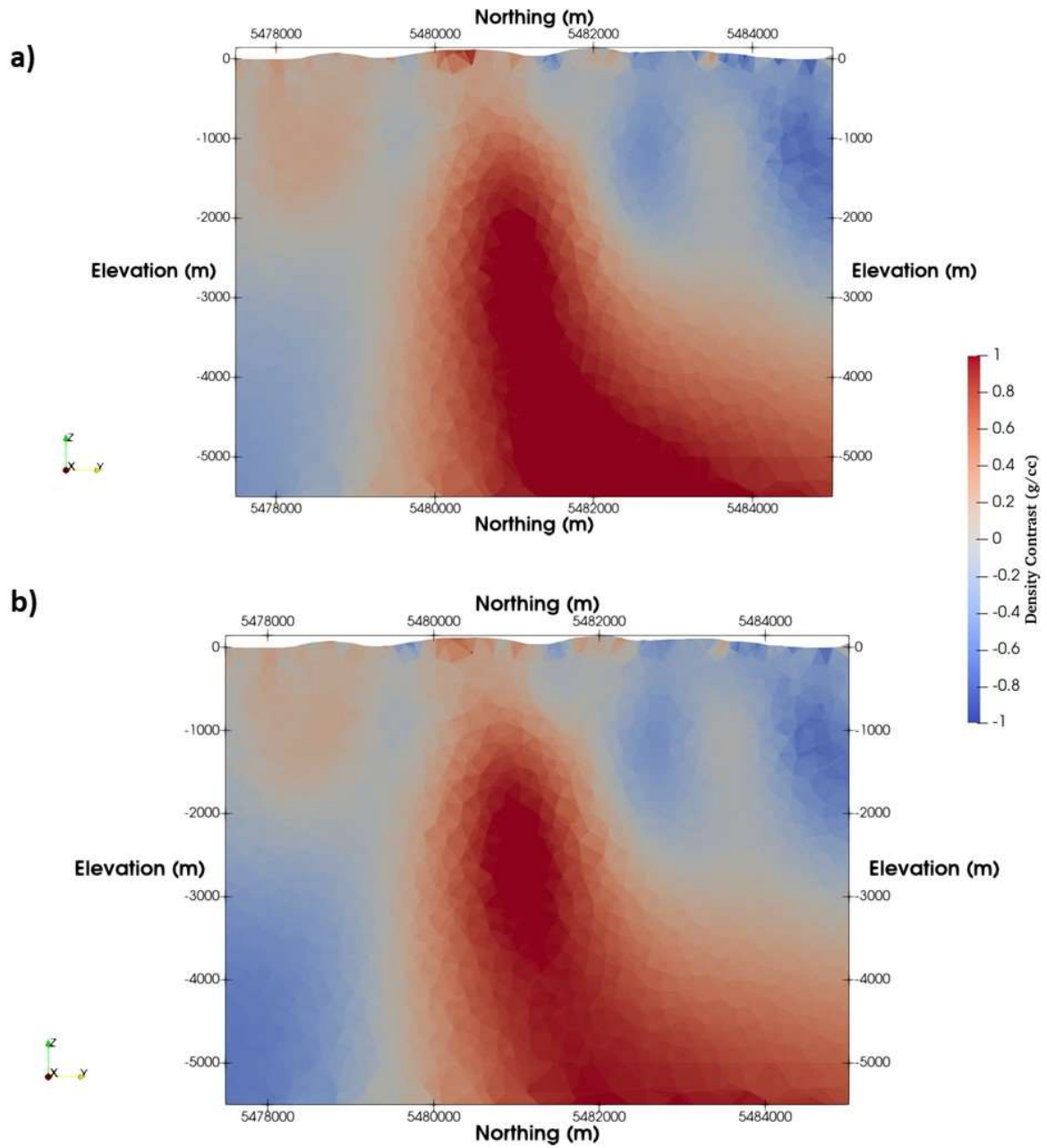
Figure 5.15: a) Cross section view of single-component inversion (*Tzz*) through the BHS (Easting 614250 m). b) Cross section view of three components inversion (*Txz, Tyz, Tzz*) through the BHS (Easting 614250 m).
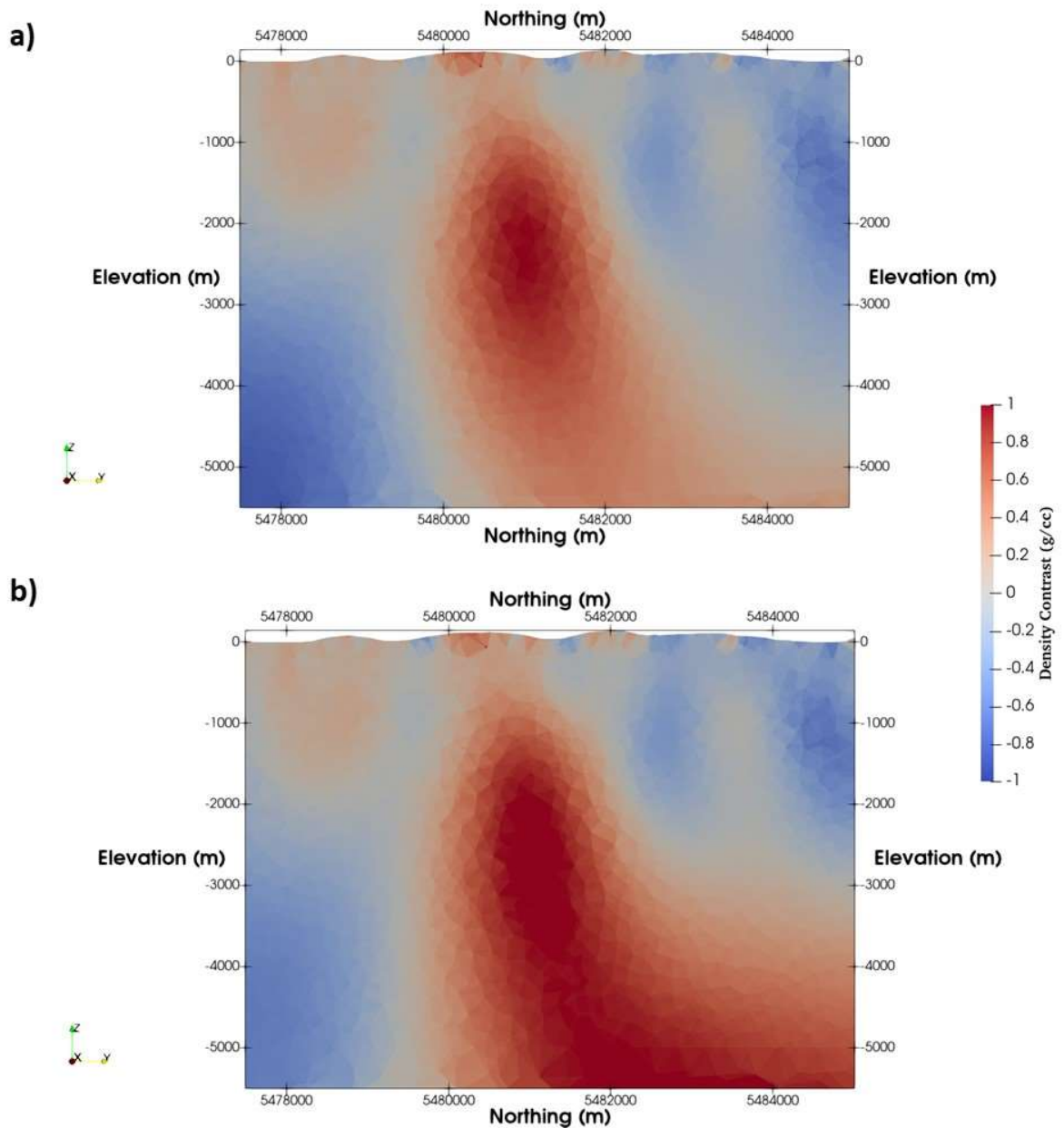
Figure 5.16: a) Cross section view of inversion utilizing curvature components (*Txx, Txy, Tyy*) through the BHS (Easting 614250 m). b) Cross section view of five components inversion (*Txx, Txy, Txz, Tyy, Tyz*) through the BHS (Easting 614250 m).

5.3.5 Six-components *Txx, Txy, Txz, Tyy, Tyz, Tzz* inversion

As the full-tensor gravity gradient data were provided for this study, the combination of all independent components (*Txx, Txy, Txz, Tyy, Tyz*) and the vertical gradient component (*Tzz*) were inverted. It is common to utilize all available information for the inversion even though the combined five component inversion model can be sufficient to obtain information about the subsurface structure (Martinez et al., 2013).

The density model was created using 21,060 data points. While the five-components inversion took 27 hours to be completed, the six-components inversion only took 14 hours. This means that combining the vertical gradient component (*Tzz*) with the five independent components assisted the inversion code to more efficiently construct a model that fits the data. The final value of *omega* was 1.03. The maps of the predicted gradiometry data for each component are shown in Figure 5.17. The maps of the normalized data residual for each component are shown in Figure 5.18.The average normalized data residual was 2.91 x 10^{-5}, and the standard deviation calculated from the normalized residuals were 1.134 for the *Txx* component, 1.103 for the *Txy* component, 1.712 for the *Txz* component, 1.390 for the *Tyy* component, 1.477 for the *Tyz* component, and 1.708 for the *Tzz* component.

Cross-section views and threshold view of the recovered model are shown in Figure 5.19. The recovered density contrast ranges from -1.230 to $+1.278$ g/cm^3. The resulting model is similar to the *Txz, Tyz, Tzz* model but has a lower maximum density contrast. The resulting model is also similar to the five-components (*Txx, Txy, Txz, Tyy, Tyz*) model but

again has a lower minimum density contrast. Overall, the inversion results using combined five and six components, respectively, are highly consistent.
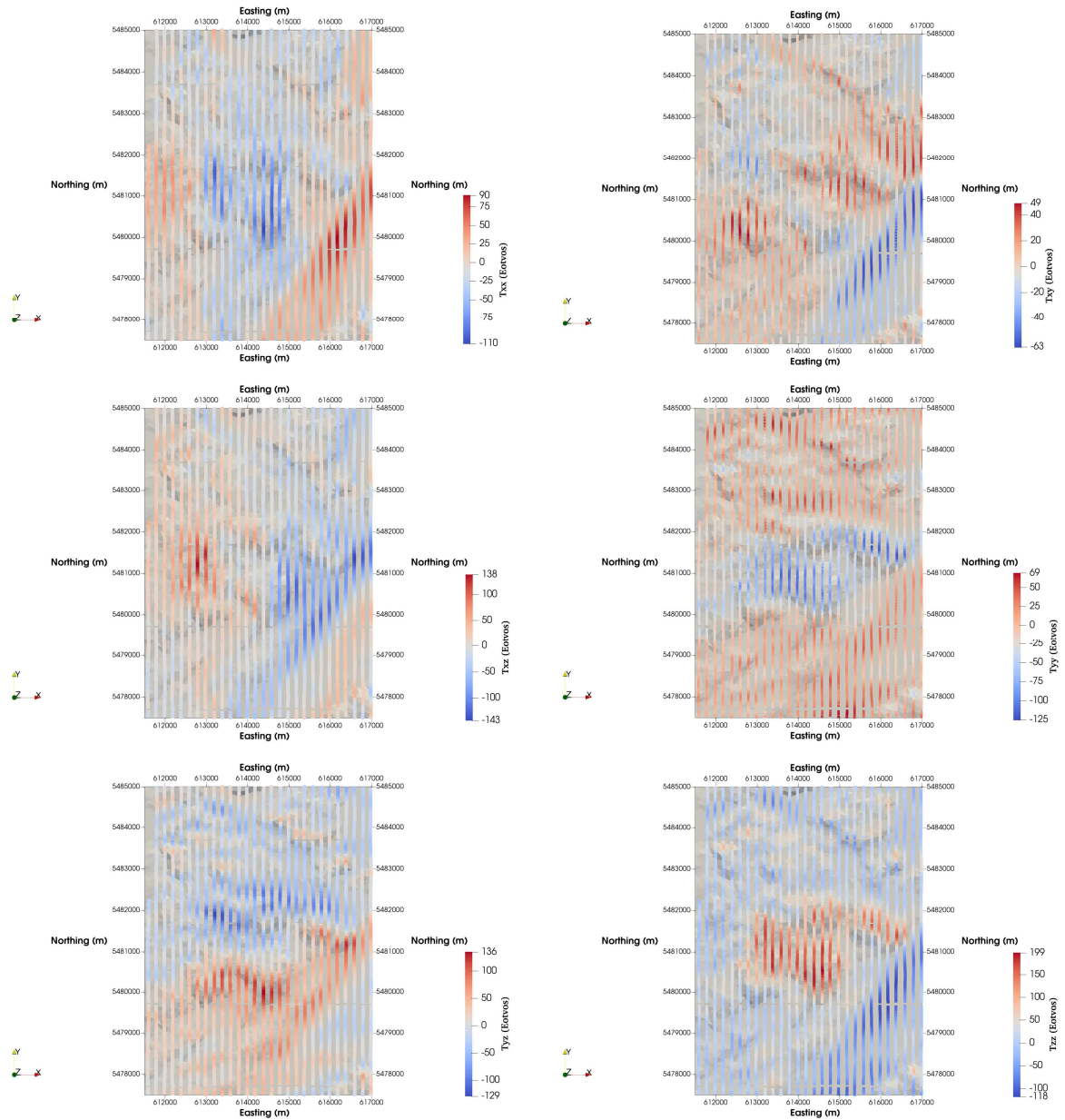
Figure 5.17: The predicted gravity gradient data for the inversion result of the six-components inversion.
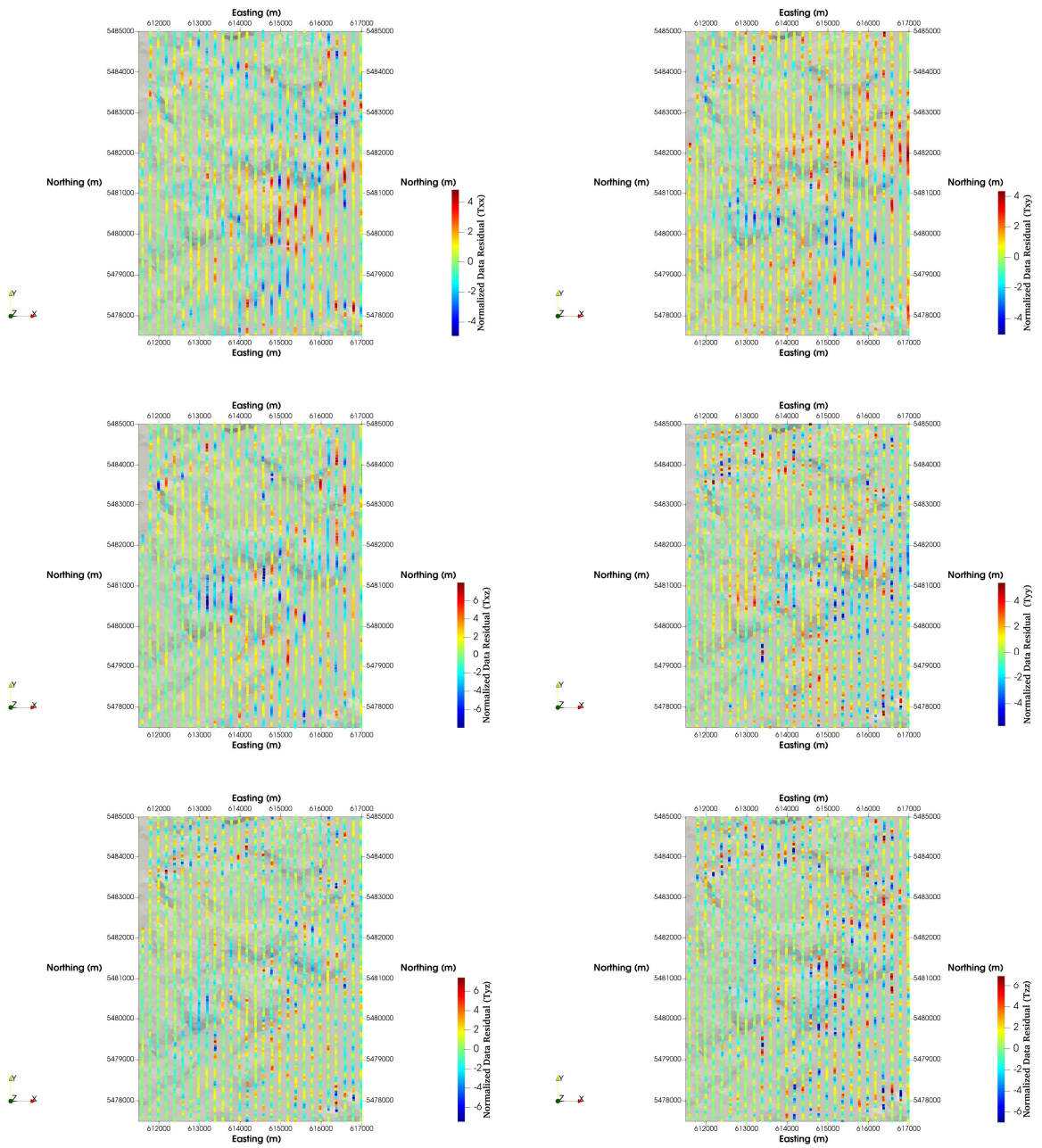
Figure 5.18 : The normalized data residuals for the result of the six-components inversion.
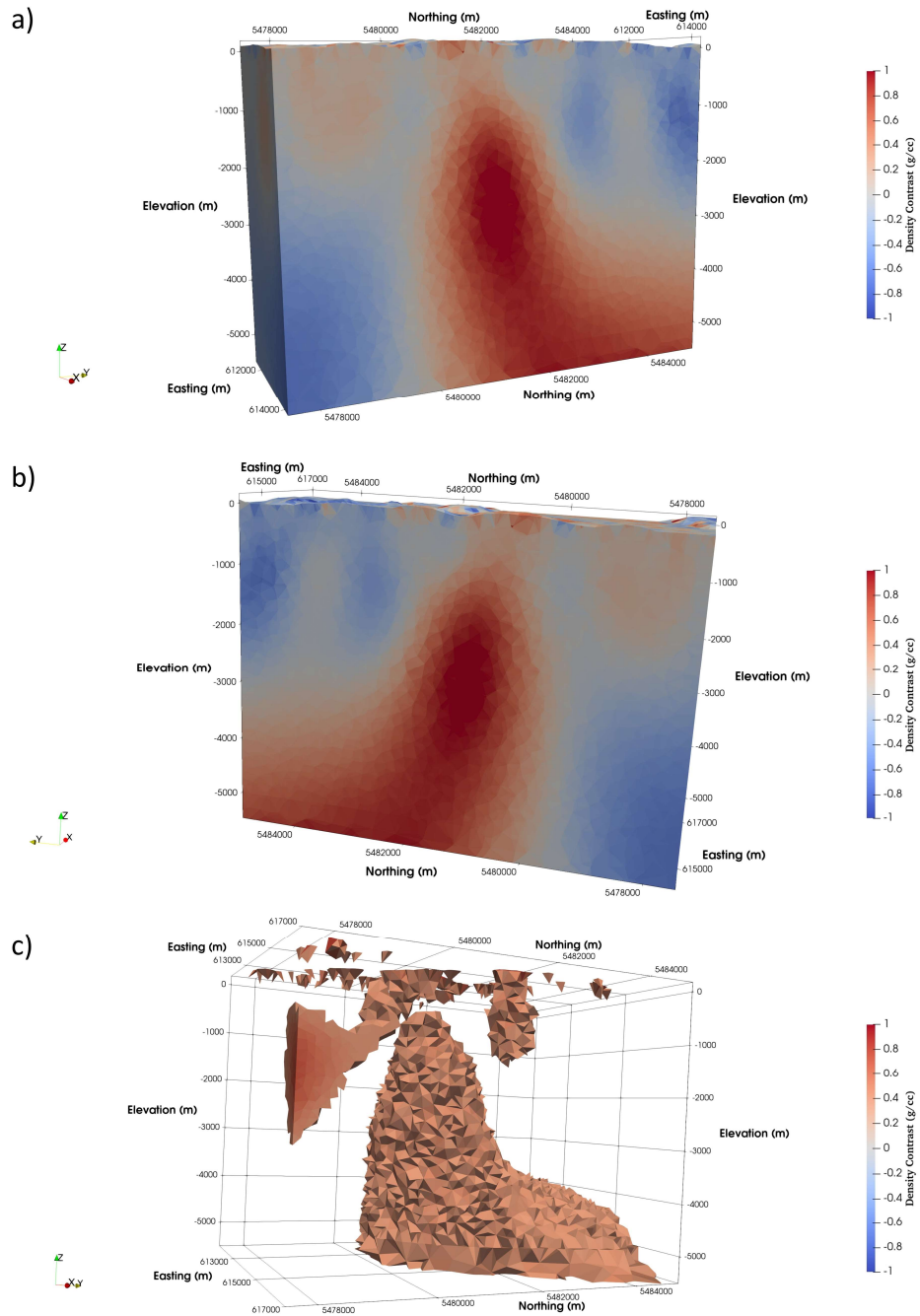
Figure 5.19: a) A view of the central part of the recovered model for the *Txx,Txy,Tyy,Txz,Tyz,Tzz* combined-components inversion result looking from southwest to north. b) A view from southeast to north. c) A threshold view of the recovered model with all cells below 0.40 g/cc removed for clarity.

5.3.6 Summary of airborne gravity gradient inversion results

All the single-component inversion results and the four different combinations of tensor components inversion results were compared. (See Appendix C for all but the *Tzz* single-component inversion results.) From the *Tzz* single-component inversion result, the structure of the BHS was resolved. Moreover, when the two components *Txz, Tyz* where included in addition to *Tzz*, improvements were seen in the overall placement and boundaries of the dense gabbro intrusion. The combination of curvature components (*Txx, Txy, Tyy*) were also inverted, and the model results provided information in the north-south and east-west directions about the edges of the BHS. When the five components *Txx, Txy, Txz, Tyy, Tyz* were inverted, the resulting model was similar to the *Txz, Tyz, Tzz* model but with a higher maximum density contrast and boundaries that were more compact. The result of the six-components combined inversion was similar to the five-components model. However, the most important difference between these two results was the time taken for the inversion code to complete. In fact, providing all available information (six components) to the inversion was beneficial for the efficiency of the inversion. Table 5.1 shows the details about all the inversion results that were demonstrated in the previous sections.

Table 5.1: The details of the inversion results for the airborne gravity gradient data.

Inversion Components	Chifact	Omega	Data Points	Density Contrast(g/cc)
Tzz	1.0	1.01	3510	-1.214, +1.404
Txz, Tyz, Tzz	2.0	1.03	10530	-1.308, +1.295
Txx, Txy, Tyy	2.0	1.04	10530	-1.349, +1.225
Txx, Txy, Txz, Tyy, Tyz	2.0	1.02	17550	-1.180, +1.302
Txx, Txy, Txz, Tyy, Tyz, Tzz	2.0	1.03	21060	-1.230, +1.278

6. Airborne Magnetic Data Inversion

The inversion of the aeromagnetic data-set is now considered (see Section 2.3) The data were obtained from *the Government of Canada GEOSCAN* open file website (Geological Survey of Canada, 1989). The airborne total-field magnetic data-set over the Budgell Harbour area (see Figure 6.1) was inverted to compare with the inversion results of the airborne gravity gradiometry inversions.
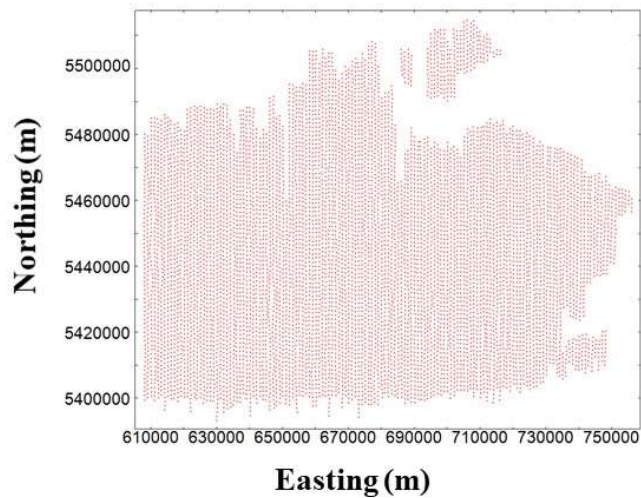
Figure 6.1: a) The map of the locations of the survey areas are shown with yellow pin marks. b) The observation points from the aeromagnetic data over the survey area.

6.1 The airborne magnetic data over Budgell Harbour

The total magnetic intensity data from the Gander-Botwood survey is shown in Figure 6.2.

The line spacing was nominally 1000 m, and the average flight height was 120 m. Figure

6.3 shows the flight lines and data points over the Budgell Harbour property. For generating

the total magnetic anomaly map; the Earth's magnetic field strength for the survey area for

the time of the survey, which was equal to 53,981 nT according to Natural Resources

Canada Magnetic Calculator (the declination was -24.90 and the inclination was 70.89),

was subtracted (Figure 6.4). The magnetic map of the Budgell Harbour area clearly shows

the dipolar-type anomaly (positive peak to the south, and negative lobe towards magnetic

north) that is characteristic of a single magnetic body magnetized by a field dipping to the

north. Also, this anomaly suggests that the body is approximately 4 km in diameter.
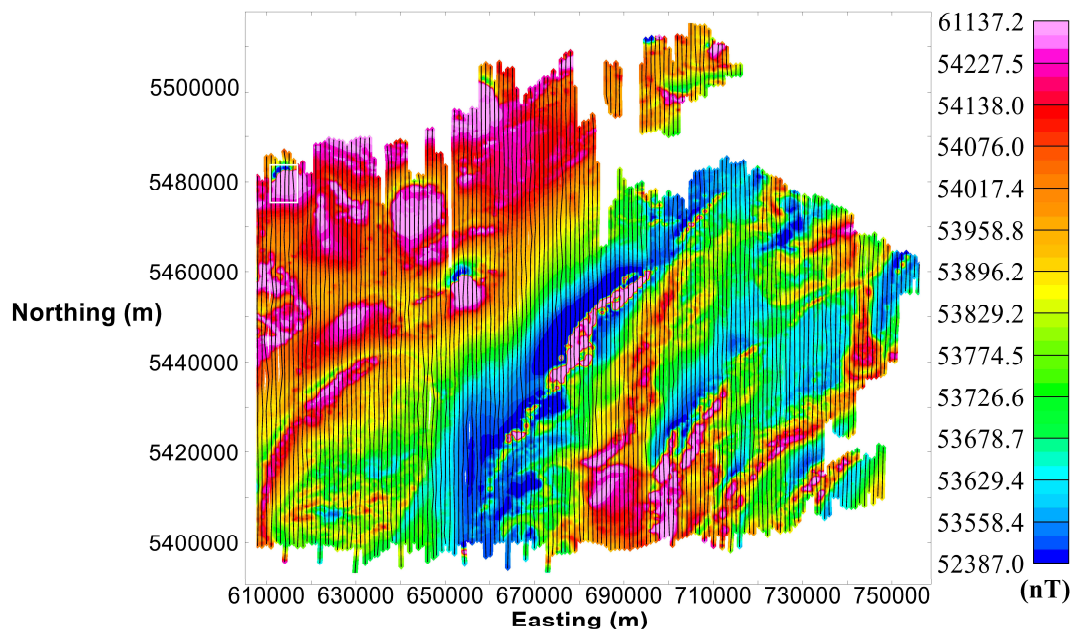
Figure 6.2: The total magnetic field intensity map of the Gander-Botwood block. The white

rectangular box on the left top indicates the location of the BHS. The black solid lines show

the flight lines. These data-sets have not been reduced to the pole.
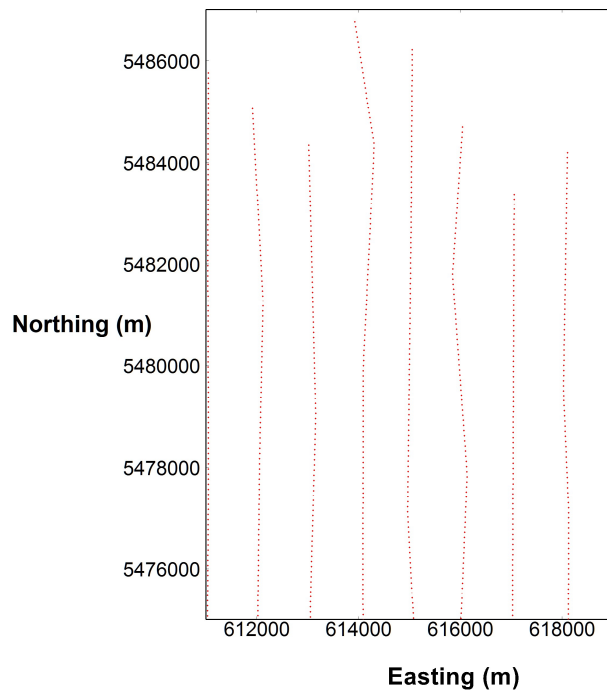
Figure 6.3: The flight lines and observation locations actually above the Budgell Harbour property. The red dots show the observation points.
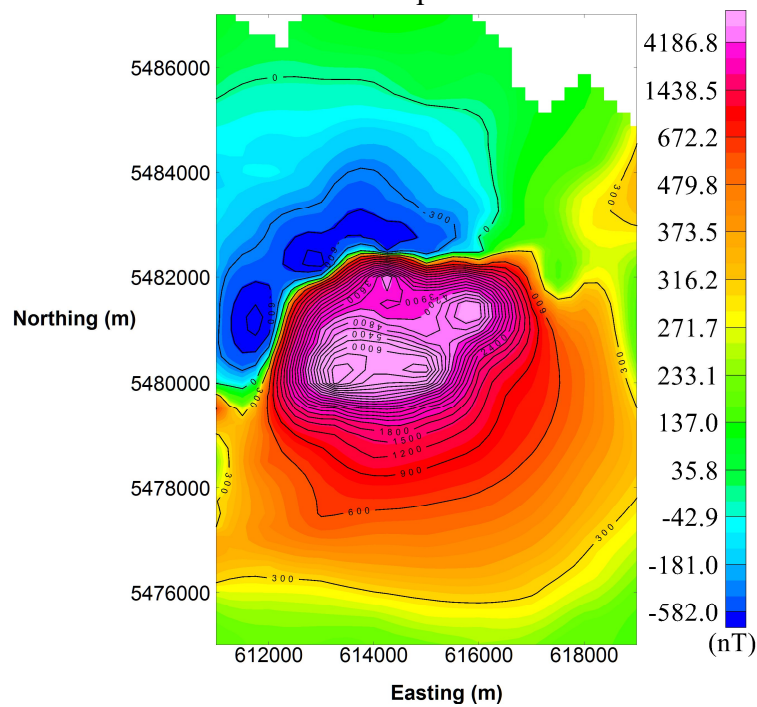
Figure 6.4: Gridded map of the Budgell Harbour property total field magnetic anomaly.

Grid cell size is 250 m. Contour interval is 300 nT.

81

6.2 Inversion of the Budgell Harbour aeromagnetic data

The inversion of the magnetic anomaly data from Budgell Harbour simply used the same mesh as was used for the inversion of the airborne gravity gradiometry data (see Figures 5.6 to 5.9). The core area of interest (COI) and the total magnetic field anomaly data points are shown in Figure 6.5. The actual observed total magnetic anomaly data above the COI are shown in Figure 6.6.

A total of 728 data points were used for the inversion. The default value of 2% was used for the measurement uncertainties. A series of different inversions were carried out to select the best *chifact* value. A chifact value of 4.0 was found to give the best combination of match to the data and reasonable structure in the model (see Appendix D). The final value of *omega* reached by the inversion was 1.03. The inversion took 4 hours (on the same computer as used for the gravity gradiometry inversions). The predicted data for the model constructed by the inversion are shown in Figure 6.7. The normalized data residuals are shown in Figure 6.8. The average normalized data residual was 1.63×10^{-1}, and the standard deviation calculated from the normalized residuals was 2.023.

The cross-section views and threshold view of the recovered susceptibility model are shown in Figure 6.9. The recovered susceptibility model ranges from 0 to +1.103 SI unitless. The resulting model clearly shows a large magnetic anomalous region, presumably the BHS, that extends to about 4 to 5 km depth and which is consistent with the model that was constructed by Miller (1976). This susceptibility anomaly is very similar in size and location to the density anomaly generated from the inversion of the gravity gradiometry data. In contrast to the gravity models, the model has few features aside from the BHS,

especially up near the surface. This is actually reasonable given that the line spacing for the data is considerably larger than for the gravity gradiometry dataset. Moreover, there is no indication of the deep dense "foot" anomaly at the bottom that there was in some of the gravity gradiometry inversions.
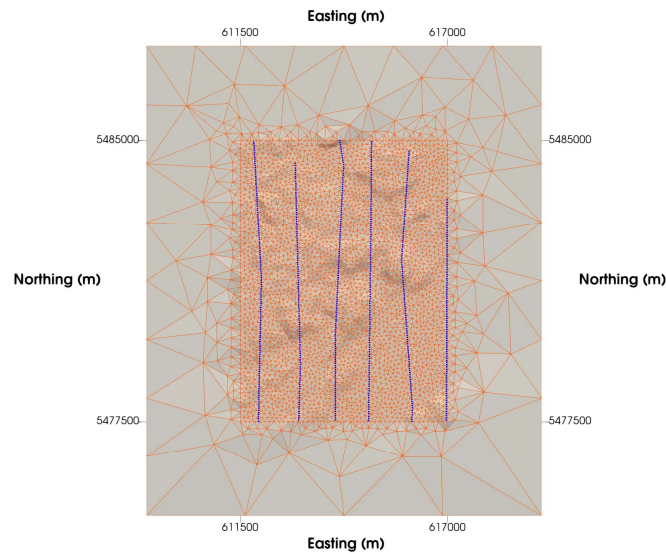
Figure 6.5: The top view of the mesh for the Budgell Harbour property. The blue dots show the observation points for the airborne total magnetic field data. The shading indicates the topography.
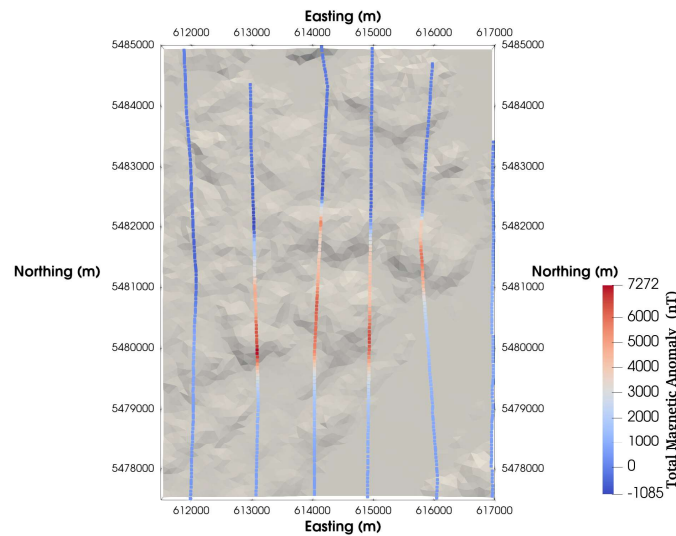
Figure 6.6: The observed total magnetic anomaly data over the core area of interest.
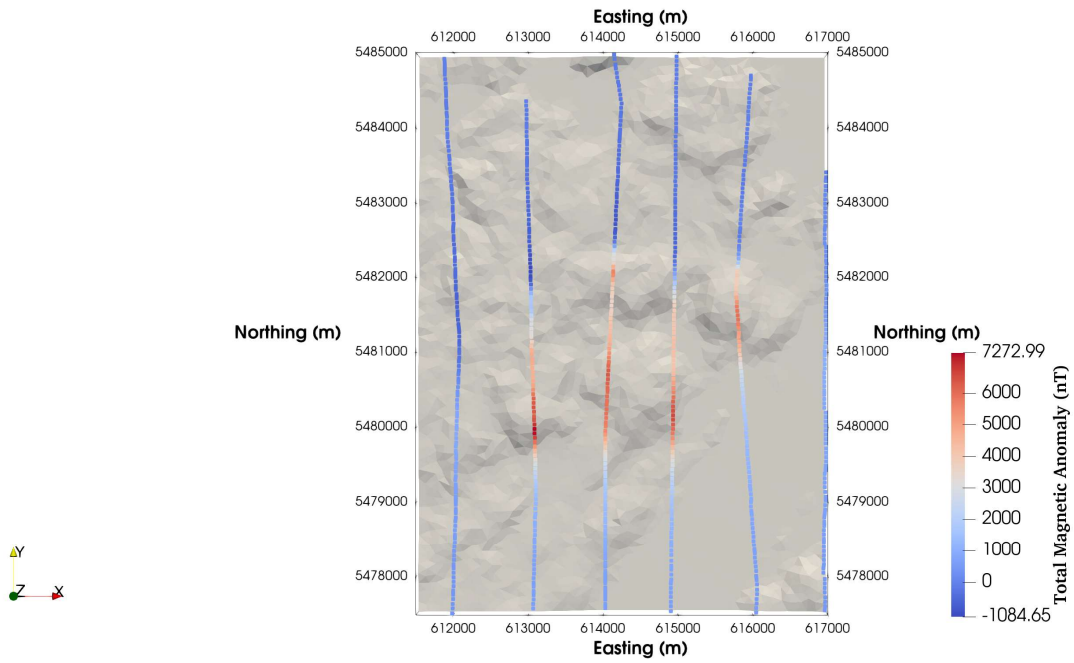
Figure 6.7: The predicted data for the result of the magnetic inversion.
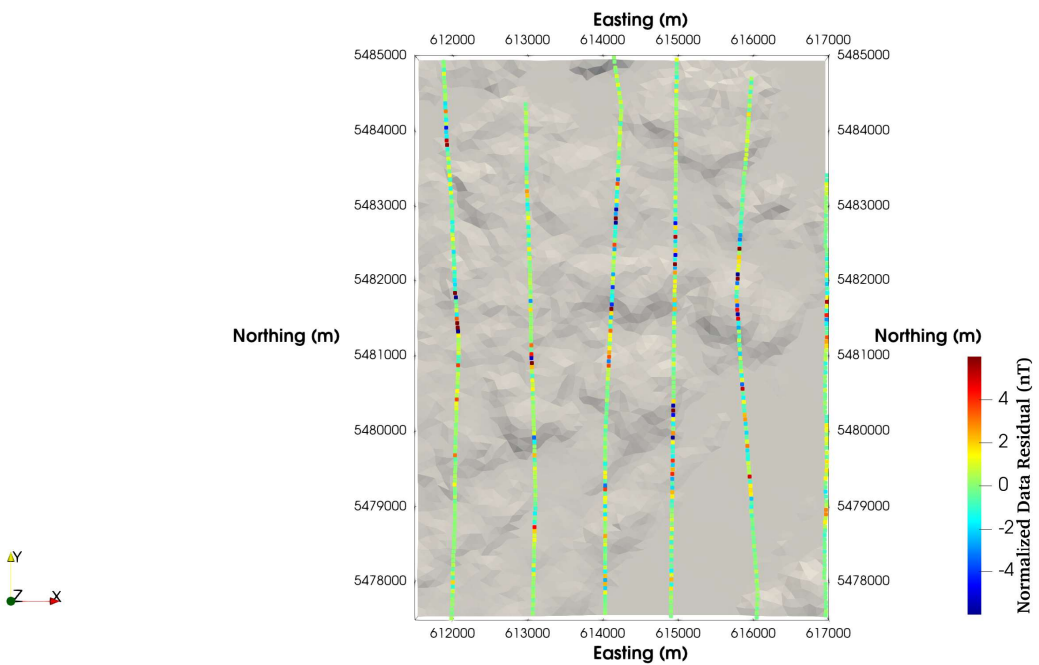
Figure 6.8: The normalized data residuals for the inversion of the magnetic anomaly data over the core area of interest.
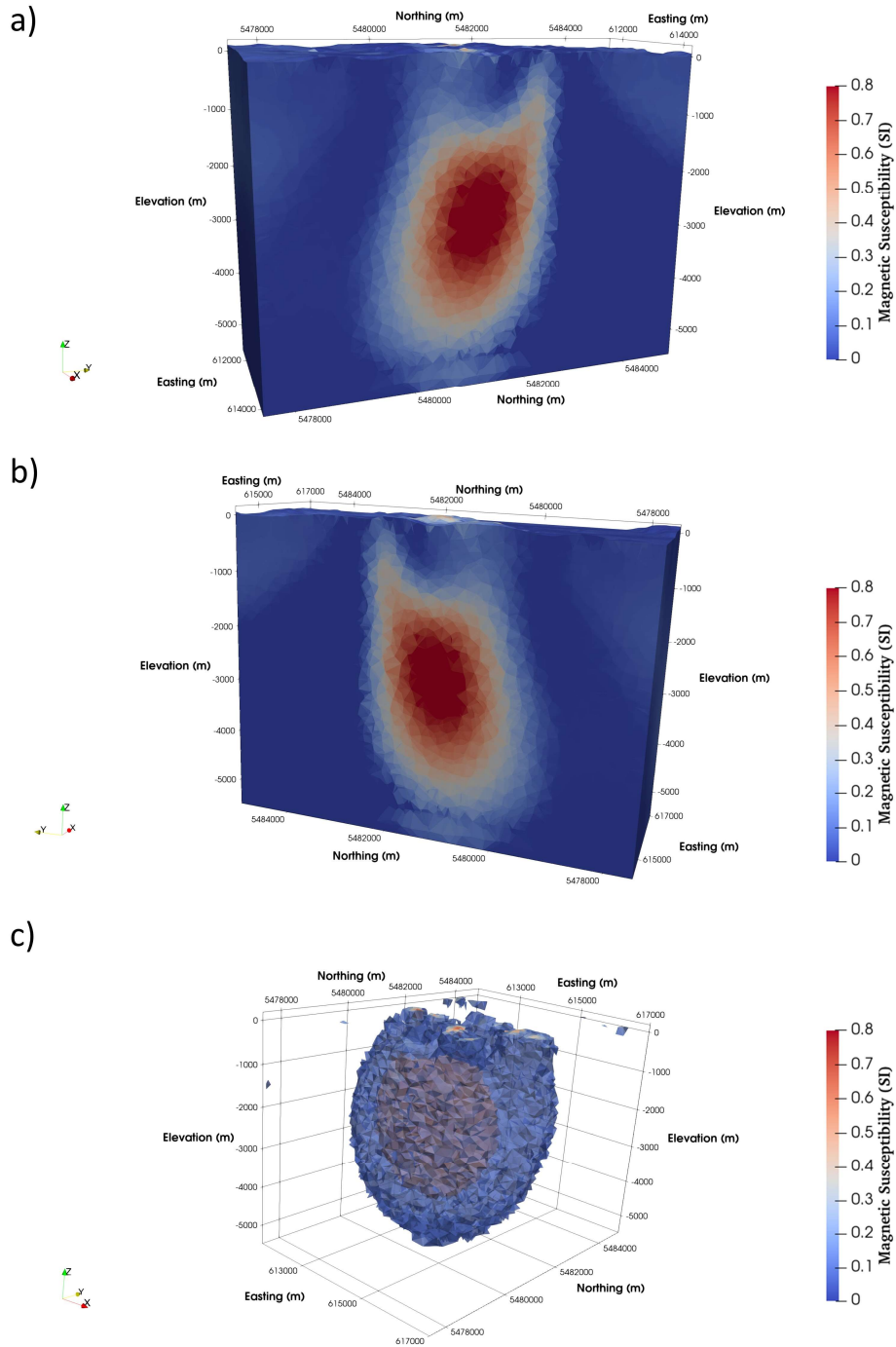
Figure 6.9: a) A view of the central part of the recovered susceptibility model for the total magnetic inversion looking from southwest to north. b) A view from southeast to north. c) A threshold view with all cells below 0.15 SI removed for clarity. The red surface within the blue surface shows all cells above 0.6 SI.

7. Joint Inversion of Gravity Gradiometry and Magnetic Data

As discussed previously (Section 4.4), jointly inverting two different data types can produce more plausible models than inversions of a single data type. Since two different geophysical data-sets are available for the Budgell Harbour area (airborne gravity gradiometry and total field magnetic data), joint inversion was considered here. The same mesh as for the individual gravity gradient and magnetic inversions was used for the joint inversion. Two types of coupling for joint inversion, correlation and fuzzy coupling, were considered (see Section 4.4; Lelièvre et al., 2012).

7.1 The joint inversion results for correlation coupling

The inversion was completed in 78 hours, and it took 26 iterations. The best *chifact* value for the six components of the gravity gradiometry data (*Txx, Txy, Txz, Tyy, Tyz, Tzz*) was found to be 1.0 after experimenting with different values. For the total magnetic data, after experimenting with different values the *chifact* value was assigned 4.0, which is the same as was used for the individual magnetic field data inversion. The value of *omega* was 0.97 when the inversion finished. In total, 728 magnetic anomaly data and 21,060 gravity gradiometry data were used for the inversion. Default measurement uncertainties (of 2%*)* were used for both gravity gradiometry and magnetic data in the inversion.

The recovered density model ranges from -1.389 to $+1.839$ g/cm^3, and the recovered susceptibility model ranges from 0 to $+1.103$ SI. The average normalized data residual

was 6.51×10^{-1}. The predicted data and normalized residuals are omitted for brevity: they are essentially equivalent to those shown previously for the six-components gravity gradiometry inversion (Figures 5.15 and 5.16) and the magnetic inversion (Figures 6.8 and 6.9).

Threshold views for the recovered models are shown in Figure 7.1. The joint inversion using the correlation coupling successfully constructed a big, deep, dense and susceptible anomaly that is presumably the BHS. Comparing the result of the joint inversion with the individual gravity gradiometry and magnetic inversions, the location and size of the Budgell Harbour gabbro intrusion can be seen more clearly in the joint inversion result (see Figures 5.11 and 6.9). Moreover, the range of susceptibility values for the susceptible body produced by the joint inversion using the correlation coupling are consistent with the individual magnetic inversion result. However, the range of anomalous densities in the joint inversion result is somewhat greater than for the six-component gravity gradiometry inversion.

Additional bodies can be seen in the joint inversion results for the correlation coupling that are thought to be artefacts (the dense and susceptible bodies in the south-west corner, and the dense body in the north-west). Interestingly, the northward-pointing foot-like anomaly at the bottom of the main density anomaly for the individual gravity gradiometry inversion, which is thought be an artefact, was not seen in the joint inversion results. Therefore, the correlation coupling for the joint inversion is judged to provided a more reasonable result than the individual gravity gradiometry inversion (see Figures 5.11)
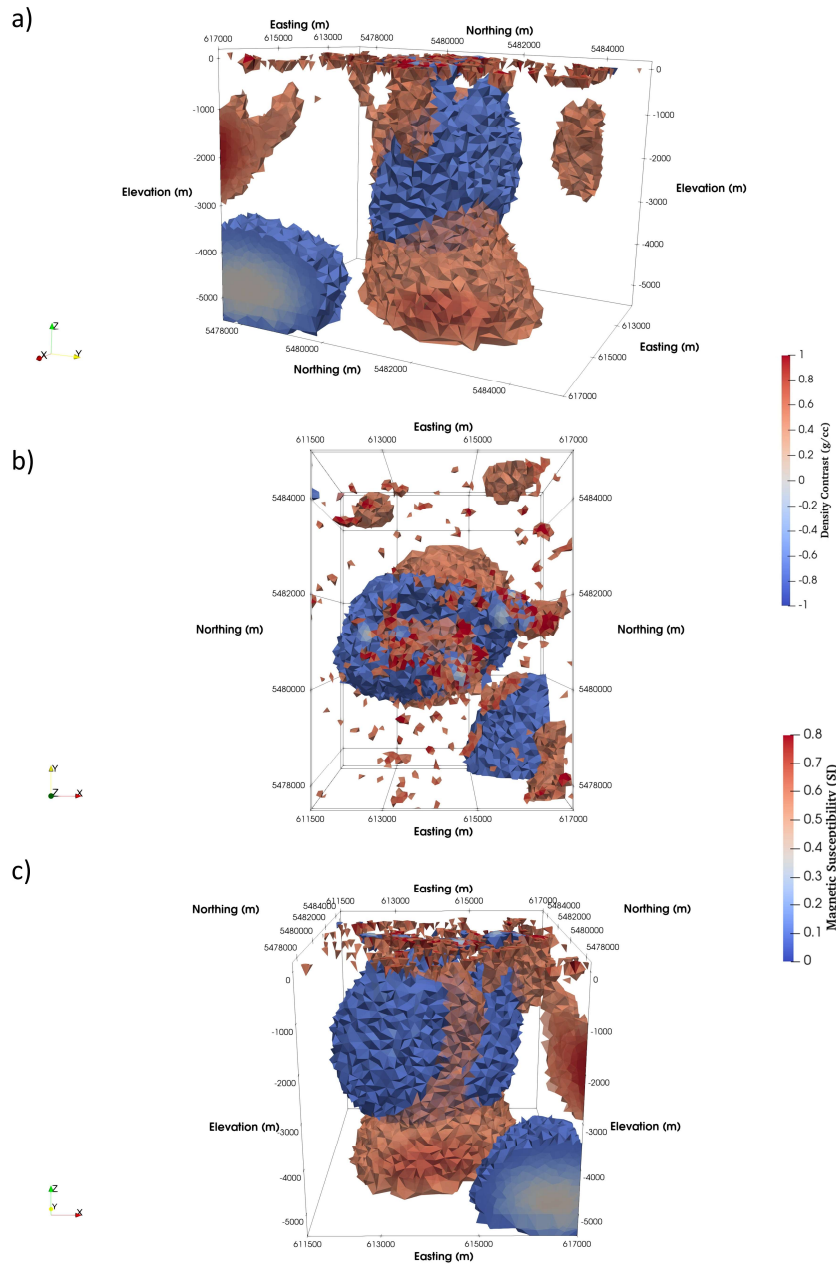
Figure 7.1: a) A threshold view of the model constructed by the correlation coupling joint inversion looking from northeast to southwest. b) A top threshold view of the joint inversion recovered model. c) A perspective threshold view. Blue structures represent the susceptibility model, and red structures represent the density model. For clarity, all the cells below 0.45 g/cc and 0.25 SI have been removed.

88

7.2 The joint inversion results for fuzzy coupling

The inversion was completed in 58 hours, and it took 33 iterations. There were two different clusters that assigned in the joint inversion for fuzzy coupling. For the first cluster centre values of density and susceptibility were respectively 0.8 g/cm^3 and 0.5 SI, and the second cluster values of density and susceptibility were 1.5 g/cm^3 and 1.0 SI. The best *chifact* value for the six components of the gravity gradiometry data (*Txx, Txy, Txz, Tyy, Tyz, Tzz*) was found to be 1.0 after experimenting with different values. For the total magnetic data, the *chifact* value was assigned 4.0 after experimenting with different values. This was the same as for the individual magnetic field data inversion.

The value of *omega* was 0.98 when the inversion finished. In total, 728 magnetic anomaly data and 21,060 gravity gradiometry data were used for the inversion. Default measurement uncertainties (of 2%*)* were used in the inversion. Threshold views for the recovered models are shown in Figure 7.2. The recovered density model ranges from −0.971 to +1.296 g/cm^3, and the recovered susceptibility model ranges from 0 to +0.89 SI.

The joint inversion results using fuzzy coupling support the idea that the additional bodies in the joint inversion results using the correlation coupling are artefacts. Also, it is assumed that the deep, centrally located, dense and susceptible body is most likely the BHS. The foot-like anomaly from the individual gravity gradiometry inversion is not seen in the fuzzy coupling joint inversion results. The similarity in the shapes of the dense and susceptible bodies showed that the joint inversion results using fuzzy coupling give the most reliable indication of the structure of the BHS. Moreover, the surfaces in Figure 7.2 are broader than the previous inversions.
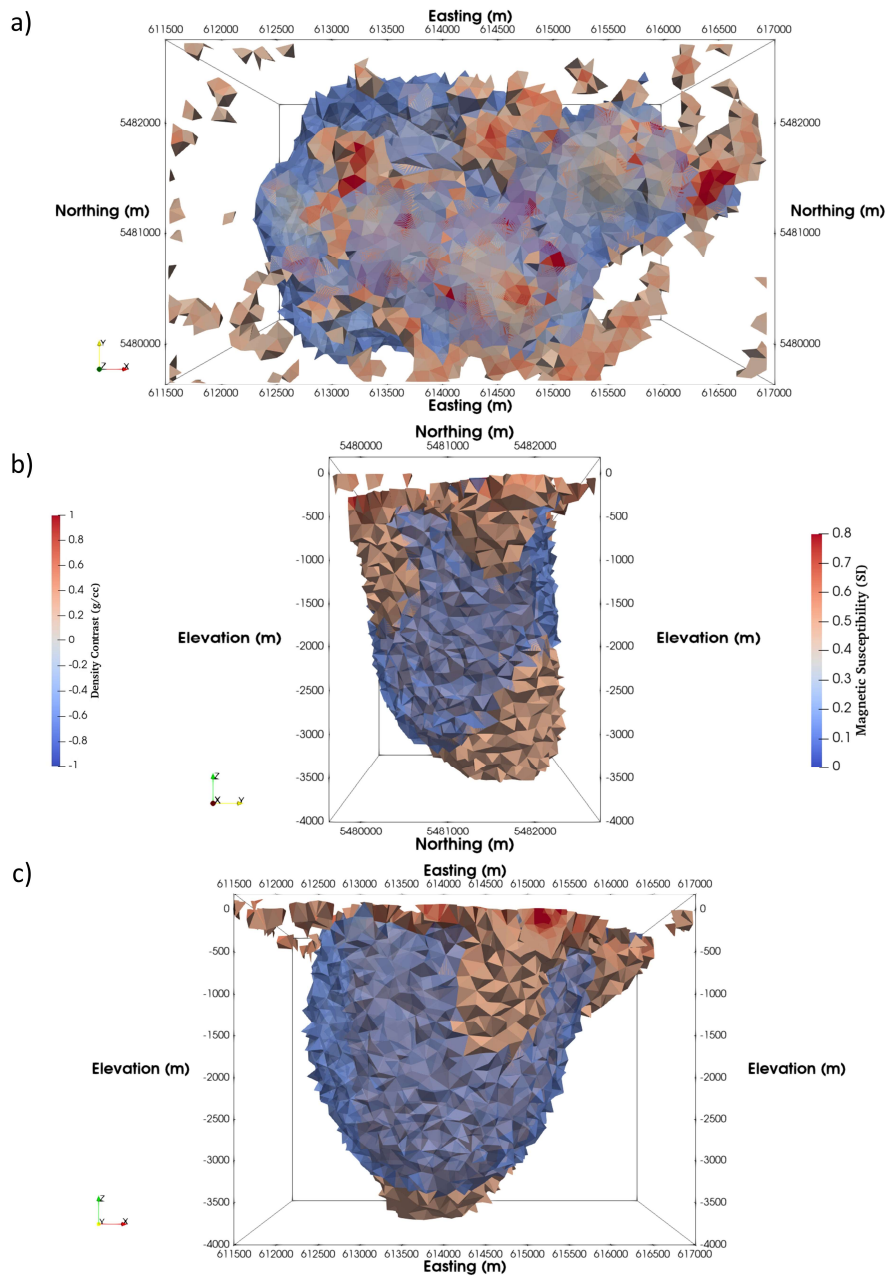
Figure 7.2: a) A top threshold view of the model constructed by joint inversion using fuzzy coupling. b) A top threshold view of the joint inversion recovered model looking from northeast to northwest. c) A perspective threshold view. Blue structures represent the susceptibility model, and red structures represent the density model. For clarity, all the cells below 0.1 g/cc and 0.15 SI have been removed.

8. Conclusions

In this project, inversion was first applied to airborne gravity gradiometry data from the Budgell Harbour area on the north coast of Newfoundland. This was then followed by inversion of the airborne magnetic data that exist for the area. Finally, joint inversion of both the gravity gradiometry and magnetic data was done.

The goals of this study were fourfold:

1. Generate an Earth model using unstructured tetrahedral meshes, specifically taking into account topography of the Budgell Harbour property.
2. Examine the single and combined component inversions of the airborne gravity gradiometry data.
3. Investigate how the inversion of the airborne total magnetic field data can also be used for the interpretation of the Budgell Harbour area.
4. Demonstrate the advantages of doing a joint inversion.

The major advantage of utilizing unstructured tetrahedral meshes for three-dimensional Earth modeling is that the tessellated surfaces in terms of triangles in geological models can precisely conform within the geophysical modeling. Thus, the combination of the geological and geophysical data will be able to go into the inversion and a common Earth model can be obtained. By using unstructured tetrahedral meshes for the inversions, the topography information of the Budgell Harbour area was included accurately, with the data considered to be at their true observation locations.

The airborne gravity gradiometry data over the Budgell Harbour Gabbro intrusion, which was acquired in 2007 (Stuckless, 2008), was examined. From the result of *Tzz* single component inversion, the subsurface geology of the BHS was delineated. Incorporating the additional gravity gradient components into the inversion enhanced the results by better defining the size, dip and depth of the gabbro intrusion. In fact, using all the information from the data-set (six-components inversion) also assisted with the inversion being able to fit the data more quickly and easily. The airborne gravity gradiometry inversion results demonstrated that the estimate of the depth to the bottom of the BHS was approximately 5.5 km, which was consistent with the depth of the airborne total field magnetic data inversion result. However, this might be caused from the mesh extensions as the regional trend was not removed from the airborne gravity gradiometry data.

Inversion of the airborne magnetic data-set from over the Budgell Harbour area, which was collected in 1987 by the Geological Survey of Canada (Geological Survey of Canada, 1989) was also done. The recovered susceptibility range was higher than expected, which was also remarked on by Miller (1976) who found that the value of the susceptibility of the intrusion body in the model was more than twice as large as measured susceptibility values from the area. Although the data points were sparsely distributed and from an old survey, the inversion result of the airborne total field magnetic anomaly data was able to outline the BHS, with an approximate depth extent of 5.5 km.

The need to learn more about the Earth or other physical systems has been the driving force for different experiments on the same object. In geophysics, it is common to collect magnetic and gravity data in exploration surveys from mineral exploration. These multiple

sets of data are significant since the additional information reduces the ambiguity or uniqueness of the interpretation (Moorkamp et al., 2016). Two types of joint inversion couplings were performed on the airborne gravity gradiometry and total field magnetic data. Although the model was generated without any prior information about the geology of the survey area for the joint inversion of correlation coupling, incorporating the data-sets of two different physical properties from the BHS yielded confidence about the shape, size, and location of the main intrusion. Also, joint inversion using fuzzy coupling for the BHS showed its efficiency in that assigning cluster values for each physical property (i.e., density and susceptibility values) can avoid the introduction of additional bodies that might actually be artifacts.

Overall, the inversions of the airborne gravity gradiometry and the airborne magnetic data provided an opportunity to see and delineate the potential of the Budgell Harbour property and its subsurface geology. Inverting the two geophysical data-sets individually and unconstrainedly was useful for seeing plausible geological structures in the subsurface, however, the joint inversion of these data-sets provided directly the location of the main body which was the BHS intrusion.

References

Ansari, S., & Farquharson, C. G. (2011). 3D finite-element simulation of electromagnetic data for inductive and galvanic components. In SEG Technical Program Expanded Abstracts 2011 (pp. 766-770). Society of Exploration Geophysicists.

Blakely, R. J. (1996). Potential theory in gravity and magnetic applications. Cambridge university press.

Bobrowsky, P. T., & Marker, B. (Eds.). (2018). Encyclopedia of Engineering Geology. Cham: Springer.

Bonvalot, S., Balmino, G., Briais, A., Kuhn, M., Peyrefitte, A., Vales, N., & Sarrailh, M. (2012). World Gravity Map., Bureau Gravimetrique International (BGI), map. CGMW-BGI-CNES-IRD Ed., Paris.

Canadian Airborne Geophysical Data Base (2020), Airborne Geophysics Section, Geological Survey of Canada, Lands and Minerals Sector, Natural Resources Canada

Carlos, D. U., Braga, M. A., Galbiatti, H. F., & Pereira, W. R. (2013). Airborne gravity gradiometry–Data processing and interpretation. Revista Brasileira de Geofísica, 31(3), 427-453.

Castonguay, S., Skulski, T., van Staal, C., & Currie, M. (2009). New insights on the structural geology of the Pacquet Harbour group and Point Rousse complex, Baie Verte peninsula, Newfoundland. Current Res Newfoundland and Labrador Dept of Natural Resources. Geol Surv Rep, 09-1.

Chapin, D. A. (1996). The theory of the Bouguer gravity anomaly: A tutorial. The Leading Edge, 15(5), 361-363.

Colman-Sadd, S.P., Hayes, J.P., and Knight, I. (1990): "Geology of the Island of Newfoundland", Government of Newfoundland and Labrador, Department of Mines and Energy, Geological Survey Branch, Map 90-001.

Cooper, M., Weissenberger, J., Knight, I., Hostad, D., Gillespie, D., Williams, H., & Clark, E. (2001). Basin evolution in western Newfoundland: new insights from hydrocarbon exploration. AAPG bulletin, 85(3), 393-418.

Dransfield, M., & Milkereit, B. (2007, September). Airborne gravity gradiometry in the search for mineral deposits. In Proceedings of exploration (Vol. 7, pp. 341-354).

Dickson, W. L. (1993). Geology of the Mount Peyton map area (NTS 2D/14), central Newfoundland. Current Research. Government of Newfoundland and Labrador, Department of Mines and Energy, Geological Survey Branch, Report, 93(1), 209-220.

Evans, D. T. (1996). Epigenetic gold occurrences, eastern and central Dunnage Zone, Newfoundland. Department of Mines & Energy, Geological Survey.

Fairhead, J. D., Cooper, G. R. J., & Sander, S. (2017). Advances in Airborne Gravity and Magnetics. In Proceedings of Exploration (Vol. 17, pp. 113-127).

Farquharson, C. G., & Oldenburg, D. W. (1998). Non-linear inversion using general measures of data misfit and model structure. Geophysical Journal International, 134(1), 213-227.

Farquharson, C. G., & Oldenburg, D. W. (2003, January). Constructing piece-wise-constant models using general measures in non-linear, minimum-structure inversion algorithms. In 6th International Symposium of the Society of Exploration Geophysicists of Japan, Tokyo, January (Vol. 2224).

Farquharson, C. G. (2008). Constructing piecewise-constant models in multidimensional minimum-structure inversions. Geophysics, 73(1), K1-K9.

Farquharson, C. G., & Lelièvre, P. G. (2017). Modelling and inversion for mineral exploration geophysics: a review of recent progress, the current state-of-the-art, and future directions. In Proceedings of Exploration 17: Sixth Decennial International Conference on Mineral Exploration. DMEC.

Geng, M., Huang, D., Yang, Q., & Liu, Y. (2014). 3D inversion of airborne gravity-gradiometry data using cokriging. Geophysics, 79(4), G37-G47.

Geng, M., Welford, J. K., Farquharson, C. G., & Peace, A. L. (2019). 3-D inversion of airborne gravity gradiometry data for the Budgell Harbour Stock, Newfoundland: A case history using a probabilistic approach. Geophysics, 84(4), 1-62.

Geng, M., Welford, J. K., Farquharson, C. G., Peace, A. L., & Hu, X. (2020). 3-D joint inversion of airborne gravity gradiometry and magnetic data using a probabilistic method. Geophysical Journal International, 223(1), 301-322.

Geological Survey of Canada, Geophysical Series Map 35502(02)G, 1989, 42 page (7sheets); https://doi.org/10.4095/125875.

Haber, E., & Oldenburg, D. (1997). Joint inversion: a structural approach. Inverse problems, 13(1), 63.

Helwig, J., Aronson, J., & Day, D. S. (1974). A Late Jurassic mafic pluton in Newfoundland. *Canadian Journal of Earth Sciences*, *11*(9), 1314-1319.

Hinze, W. J., Von Frese, R. R., & Saad, A. H. (2013). Gravity and magnetic exploration: Principles, practices, and applications. Cambridge University Press.

Jahandari, H., & Farquharson, C. G. (2011). Forward modelling of gravity data for unstructured grids using the finite-volume method. In SEG Technical Program Expanded Abstracts 2011 (pp. 877-881). Society of Exploration Geophysicists.

Jekeli, C. (2006). Airborne gradiometry error analysis. Surveys in geophysics, 27(2), 257-275.

Kearey, P., Brooks, M., & Hill, I. (2013). An introduction to geophysical exploration.

LaFehr, T. R., & Nabighian, M. N. (2012). Fundamentals of gravity exploration. Society of Exploration Geophysicists.

Lelièvre, P. G., Farquharson, C. G., & Hurich, C. A. (2011). Computing first-arrival seismic traveltimes on unstructured 3-D tetrahedral grids using the fast marching method. Geophysical Journal International, 184(2), 885-896.

Lelièvre, P. G., Farquharson, C. G., & Hurich, C. A. (2012). Joint inversion of seismic traveltimes and gravity data on unstructured grids with application to mineral exploration. Geophysics, 77(1), K1-K15.

Lelièvre, P., Carter-McAuslan, A., Farquharson, C., & Hurich, C. (2012). Unified geophysical and geological 3D Earth models. The Leading Edge, 31(3), 322-328.

Lelièvre, P. G., & Farquharson, C. G. (2013). Gradient and smoothness regularization operators for geophysical inversion on unstructured meshes. Geophysical Journal International, 195(1), 330-341.

Lelièvre P. G. and Farquharson C. G., 2015, PODIUM: a suite of software utilities for Preparation Of Data for Inversion on Unstructured Meshes.

Lelièvre, P. G., Carter-McAuslan, A. E., Dunham, M. W., Jones, D. J., Nalepa, M., Squires, C. L., ... & Farquharson, C. G. (2018). FacetModeller: Software for manual creation, manipulation and analysis of 3D surface-based models. SoftwareX, 7, 41-46.

Li, Y., & Oldenburg, D. W. (1996). 3-D inversion of magnetic data. Geophysics, 61(2), 394-408.

Li, X., & Chouteau, M. (1998). Three-dimensional gravity modeling in all space. Surveys in Geophysics, 19(4), 339-368.

Martinez, C., & Li, Y. (2011). Inversion of regional gravity gradient data over the Vredefort Impact Structure, South Africa. In SEG Technical Program Expanded Abstracts 2011 (pp. 841-845). Society of Exploration Geophysicists.

Martinez, C., Li, Y., Krahenbuhl, R., & Braga, M. A. (2013). 3D inversion of airborne gravity gradiometry data in mineral exploration: A case study in the Quadrilátero Ferrífero, Brazil. Geophysics, 78(1), B1-B11.

Mataragio, J., & Kieley, J. (2009). Application of full tensor gradient invariants in detection of intrusion-hosted sulphide mineralization: Implications for deposition mechanisms. First Break, 27(7).

Miller, H. G. (1976). A magnetic model for the Budgell Harbour Stock, Newfoundland. Canadian Journal of Earth Sciences, 13(2), 231-236.

Miller, H. G., & Singh, V. (1994). Potential field tilt—a new concept for location of potential field sources. Journal of Applied Geophysics, 32(2-3), 213-217.

Moorkamp, M., Lelièvre, P. G., Linde, N., & Khan, A. (Eds.). (2016). *Integrated imaging of the earth: Theory and applications* (Vol. 218). John Wiley & Sons.

Murphy, C.A. (2004). The Air-FTG airborne gravity gradiometer system. In Airborne Gravity 2004 - Abstracts from the ASEF-PESA Airborne Gravity 2004 Workshop, R.J. Lane (Ed). Geoscience Australia Record: 2004/18, 7-14

Nabighian, M. N., Ander, M. E., Grauch, V. J. S., Hansen, R. O., LaFehr, T. R., Li, Y., ... & Ruder, M. E. (2005). Historical development of the gravity method in exploration Historical Development of Gravity Method. Geophysics, 70(6), 63ND-89ND.

Okabe, M. (1979). Analytical expressions for gravity anomalies due to homogeneous polyhedral bodies and translations into magnetic anomalies. Geophysics, 44(4), 730-741.

Oruç, B., & Keskinsezer, A. (2008). Structural setting of the northeastern Biga Peninsula (Turkey) from tilt derivatives of gravity gradient tensors and magnitude of horizontal gravity components. Pure and Applied geophysics, 165(9-10), 1913-1927.

Peace, A. L., Welford, J. K., Geng, M., Sandeman, H., Gaetz, B. D., & Ryan, S. S. (2018). Rift-related magmatism on magma-poor margins: Structural and potential-field analyses of the Mesozoic Notre Dame Bay intrusions, Newfoundland, Canada and their link to North Atlantic Opening. Tectonophysics, 745, 24-45.

Peace, A. L., Welford, J. K., Geng, M., Sandeman, H., Gaetz, B. D., & Ryan, S. S. (2018). Structural geology data and 3-D subsurface models of the Budgell Harbour Stock and associated dykes, Newfoundland, Canada. Data in brief, 21, 1690-1696.

Reynolds, J. M. (2011). An introduction to applied and environmental geophysics. John Wiley & Sons.

Rücker, C., Günther, T., & Spitzer, K. (2006). Three-dimensional modelling and inversion of dc resistivity data incorporating topography—I. Modelling. Geophysical Journal International, 166(2), 495-505.

Saad, A. H. (2006). Understanding gravity gradients—A tutorial. The Leading Edge, 25(8), 942-949.

Schofield, D. I., & D'Lemos, R. S. (2000). Granite petrogenesis in the Gander Zone, NE Newfoundland: mixing of melts from multiple sources and the role of lithospheric delamination. Canadian Journal of Earth Sciences, 37(4), 535-547.

Shewchuk, J. R. (1996, May). Triangle: Engineering a 2D quality mesh generator and Delaunay triangulator. In Workshop on Applied Computational Geometry (pp. 203-222). Springer, Berlin, Heidelberg.

Shewchuk, J. R. (2002). Delaunay refinement algorithms for triangular mesh generation. Computational geometry, 22(1-3), 21-74.

Si, H. (2015). TetGen, a Delaunay-based quality tetrahedral mesh generator. ACM Transactions on Mathematical Software (TOMS), 41(2), 11.

Strong, D. F., & Harris, A. (1974). The petrology of Mesozoic alkaline intrusives of central Newfoundland. Canadian Journal of Earth Sciences, 11(9), 1208-1219.

Stuckless, E. (2008). Celtic minerals assessment report discussing Geochemistry. Geophysics, and Diamond Drilling on the Budgell's Harbour Property, Central Newfoundland.

Telford, W. M., Telford, W. M., Geldart, L. P., Sheriff, R. E., & Sheriff, R. E. (1990). Applied geophysics (Vol. 1). Cambridge university press.

Walter, C., Braun, A., & Fotopoulos, G. (2020). High-resolution unmanned aerial vehicle aeromagnetic surveys for mineral exploration targets. Geophysical Prospecting, 68(1-Cost-Effective and Innovative Mineral Exploration Solutions), 334-349.

Williams, N. C. (2008). Geologically-constrained UBC–GIF gravity and magnetic inversions with examples from the Agnew-Wiluna greenstone belt, Western Australia (Doctoral dissertation, University of British Columbia).

Zhdanov, M. S. (2002). Geophysical inverse theory and regularization problems (Vol. 36). Elsevier.

Appendices

A – *PODIUM* Software

PODIUM is a software package of utilities for Preparation Of Data for Inversion on Unstructured Meshes (Lelièvre and Farquharson, 2015). The package also has many utilities for working with rectilinear meshes. However, it does not include any forward or inverse modelling programs (see Appendix B). Following are some programs in this package, and files that they use, that I have used for generating PLCs, meshes and models:

block_COI.txt: The file consisting of the coordinate information for the core area of interest in the model.

block_POI.txt: The file containing the coordinate information for the padded volume of interest area in the model.

blocks2vtu: The program that generates a .vtu file from blocks files (see above), and writes the facet information to a .vtu file.

combine_files: The program that combines information from .node, .ele, .poly files.

conform_topography: The program that incorporates topography information with the blocks files.

interpolate_data: The program that reads topography or geophysical data from a file and interpolates it to specified points.

make_obs: The program to generate gridded observation locations and write them to a .node or .ele file.

mesh2poly: The program to convert an unstructured mesh defined by .node and .ele files are converted to a .poly file for use with the TetGen and Triangle meshing programs.

mesh2vtu: The program that converts a pair of .node and .ele files to .vtu file for visualization in the ParaView software.

node2d: Changes a 3D .node file to a 2D .node file.

node3d: Changes a 2D .node file to a 3D .node file.

node2vtu: Converts a .node file to a .vtu file for visualizing in the ParaView software.

poly2mesh: Converts a .poly file to a .node and .ele files.

remove_duplicates: The program that removes duplicates or closely spaced observation points from a .node file.

remove_range: It removes nodes from a specified range in a .node file.

In addition to PODIUM, the Triangle and Tetgen software were used for generating 2D and 3D meshes respectively. These software are publicly available:

- Triangle:

  http://www.cs.cmu.edu/~quake/triangle.html

- TetGen:

  http://wiasberlin.de/software/tetgen/1.5/doc/manual/manual006.html#sec69 .

B – *MAGNUM* Software

MAGNUM is comprised of three programs (FOGO, VIDI, and DYNO) for Multi-modal Applied Geophysical Numerical modeling on Unstructured Meshes. Rectilinear meshes are also supported by this package. Forward and inversion modeling programs are included in MAGNUM (Lelièvre and Farquharson, 2015).

B.1 - *FOGO*

FOGO is a program for FOrward Modeling of GeOphysical data, and it supports the following data types:

- scalar gravity data (gz)
- gradiometry gravity data (gg)
- total magnetic field data (mag)
- first-arrival seismic traveltimes (fat).

The models can be built on a rectilinear or unstructured mesh. There are four main input files that need to be provided by the user:

- meshinp – a model discretization file,
- propinp – a physical property specification file,
- datainp – a data input file,
- outroot – the names of the output files.

The contents of the input files for the program *FOGO* are shown in Table B.1.

Table B.1: The *FOGO* input files used for forward modeling in this project.

datatype	"gg"	Gravity gradiometry data
comps	"tttttt"	Specifies which tensor components to use
obsfile	"obs.node"	File containing the observation locations
meshtype	"unstructured"	The type of mesh
mehsfile	"meshfile.node"	File containing mesh information
modelfile	"modelfile.ele"	File containing model information
neighfile	"meshfile.neigh"	File containing unstructured meshes only
zdir	"1"	Specifies the coordinate system
prototype	"den"	Determine the physical property

B.2 – *VIDI*

VIDI (**V**oxel**I**zed **DI**scretization) is a mesh-based inversion program that constructs the physical property values inside the mesh cells. It is a flexible and highly functional program. The following are the supported geophysical data types:

- scalar gravity data (gz)
- gradiometry gravity data (gg)
- total magnetic field data (mag)
- magnetic amplitude data (amp)
- first-arrival seismic traveltimes (fat)

Moreover, the multiple data types can be jointly inverted. Table B.2 shows the parameters and files for the use of both single and joint inversion.

Table B.2: The *VIDI* input files and parameters that are used for single and joint inversion in this project.

datatype	"gg,mag"	Gravity gradiometry data
comps	"tttttt"	Specifies which tensor components to use
obsfile	"obs.node"	File containing the observation locations
meshtype	"unstructured"	The type of mesh
mehsfile	"meshfile.node"	File containing mesh information
modelfile	"modelfile.ele"	File containing model information
neighfile	"meshfile.neigh"	File containing unstructured meshes only
zdir	"1 or -1"	Specifies the coordinate system
prototype	"den, sus"	Determine the physical property
form	"sus"	Specifies the magnetics formulation
igeo	"value"	Geomagnetic field inclination in degrees
dgeo	"value"	Geomagnetic field declination in degrees
sgeo	"value"	Geomagnetic field strength in nT
idir	"value"	measurement inclination in degrees
ddir	"value"	measurement declination in degrees
lambdainit	"value"	Initial trade-off parameter values
chifact	"value"	Normalized target misfit
chitol	"value"	Relative tolerance on the target misfit
alphaj	"value"	Multiplier on the sum of joint measures
jointinp	"files"	Input files for the joint inversion
stageinit	"value"	The joint inversion will start at this stage
jchitol	"value"	Relative tolerance on the joint pareto misfit
rho	"0"	Final multiplier value for the joint measure
nstepts	"1"	Number of lambda steps over heating the rho value
coupling	"null"	Correlation, Linear grad, Equal, Equal grad, Fuzzy
issqr	"t"	Set to false (f) to specify positive or negative correlation
pn	"0"	Only used if issqr is false

C – Independent components inversion results

In addition to the vertical gradient component (Tzz) of the airborne gravity gradient data, other independent components were individually inverted. As discussed in Section 5.1, it is expected that Txx and Tyy delineate the edges of the intrusion in the east-west and north-south directions. Txy indicates all the other features around the gabbro intrusion in the north-south direction. Txz and Tyz demonstrate the central axes of the Budgell Harbour Gabbro intrusion in the north-south and east-west directions. Table C.1 gives the details of the inversion results for each individual component. Moreover, threshold views of the models constructed for the independent component inversions are shown in Figure C.1. A series of values of *chifact* were investigated to find the ideal *chifact* value for the inversion of each single component. The ideal *chifact* value produces a data misfit value which equals the total number of data points multiplied by the *chifact* value to within a 2% error margin. The ideal *chifact* value for the inversions of the individual components was found to be 1.0. Figure C.2 shows the values of data misfit and measure of model structure for the six different values of *chifact* tried for the *Tzz* component, with the value of *chifact* = *1* corresponding to the preferred location on the main bend in the misfit-model norm curve.

Table C.1: The details of the inversion results for independent components.

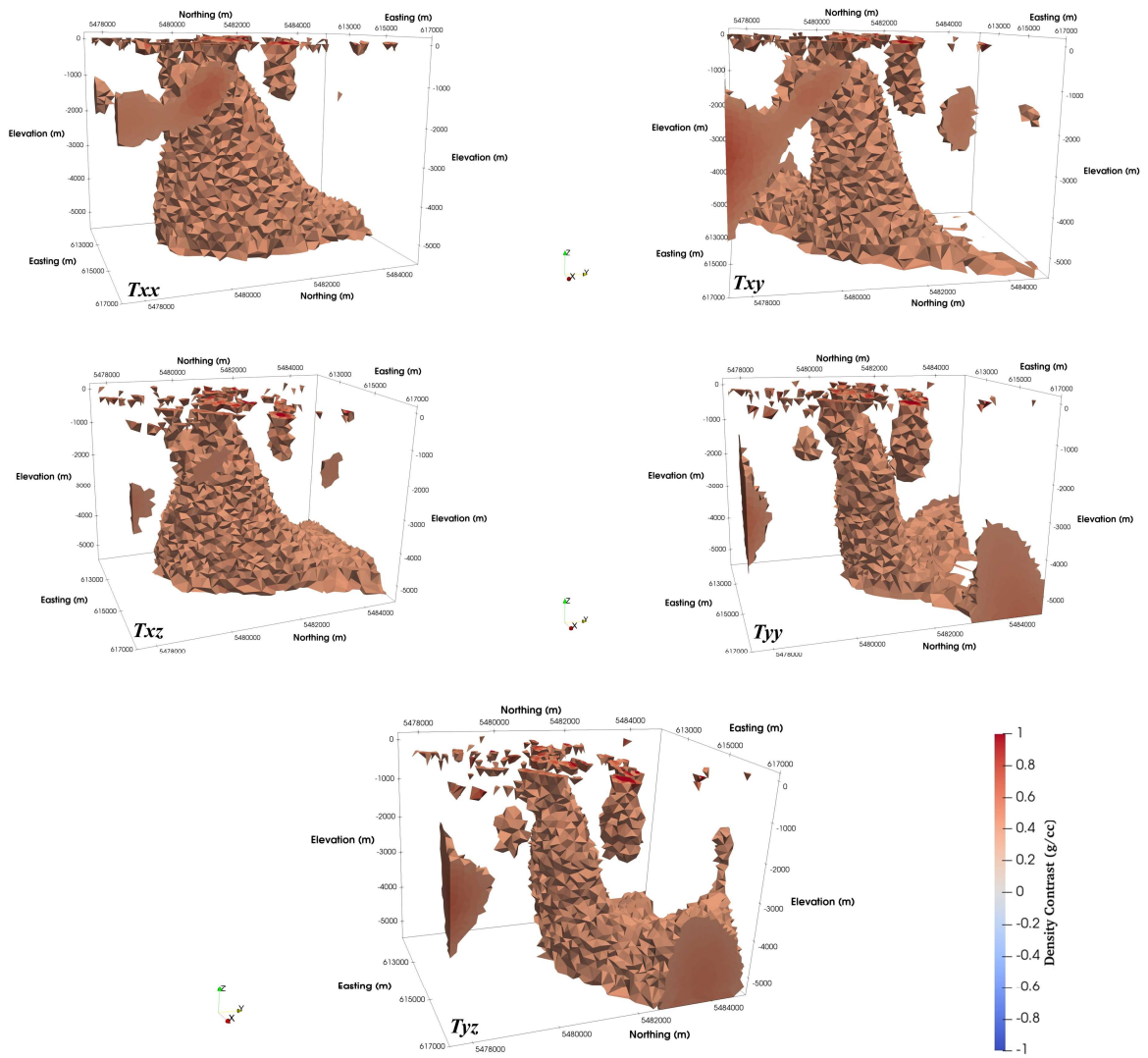| Components	Chifact	Omega	Data Points	Density Contrast (g/cc)	Average Normalized Data Residual
Txx	1.0	0.987	3510	-1.152, +1.089	-3.857 x 10^{-5}
Txy	1.0	1.008	3510	-1.076, +1.213	-4.126 x 10^{-5}
Txz	1.0	0.995	3510	-1.046, +1.230	-2.324 x 10^{-5}
Tyy	1.0	1.011	3510	-1.296, +1.268	6.407 x 10^{-6}
Tyz	1.0	1.004	3510	-1.278, +1.334	3.789 x 10^{-5}

Figure C.1: A threshold view of the recovered models for each independent-component inversion (from top-left to bottom *Txx, Txy, Txz, Tyy, Tyz* respectively). For clarity, all cells with a density below 0.40 g/cc have been removed.
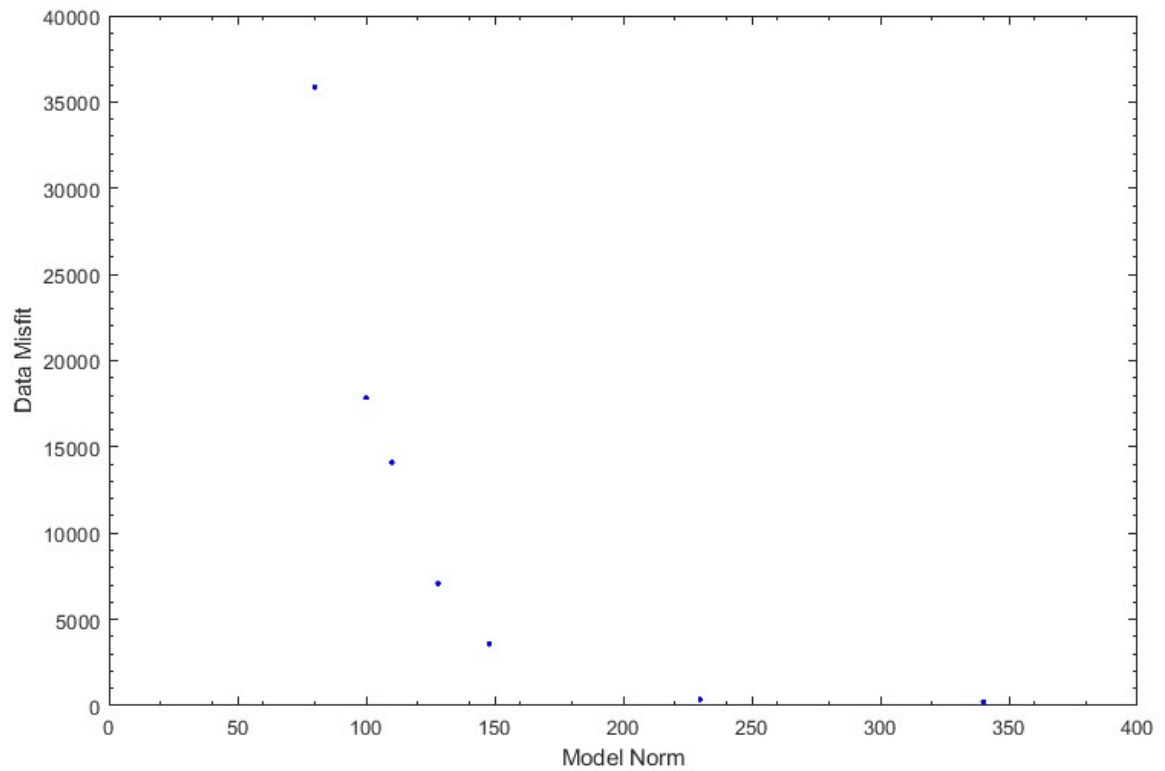
Figure C.2: Trade-off curve for the inversion of the *Tzz* component of the airborne gravity gradient data for Budgell Harbour gabbro intrusion for *chifact* = 10, 5, 4, 2, 1, 0.1, 0.01 (left to right).

D – The trade-off parameter experiment for the airborne total magnetic field data inversion

The ideal *chifact* value for the inversions of the airborne total magnetic field data was found to be 4.0. Figure D.1 shows the values of data misfit and measure of model structure for the six different values of *chifact* tried for the total magnetic field, with the value of *chifact* = *4* corresponding to the preferred location on the main bend in the misfit-model norm curve.
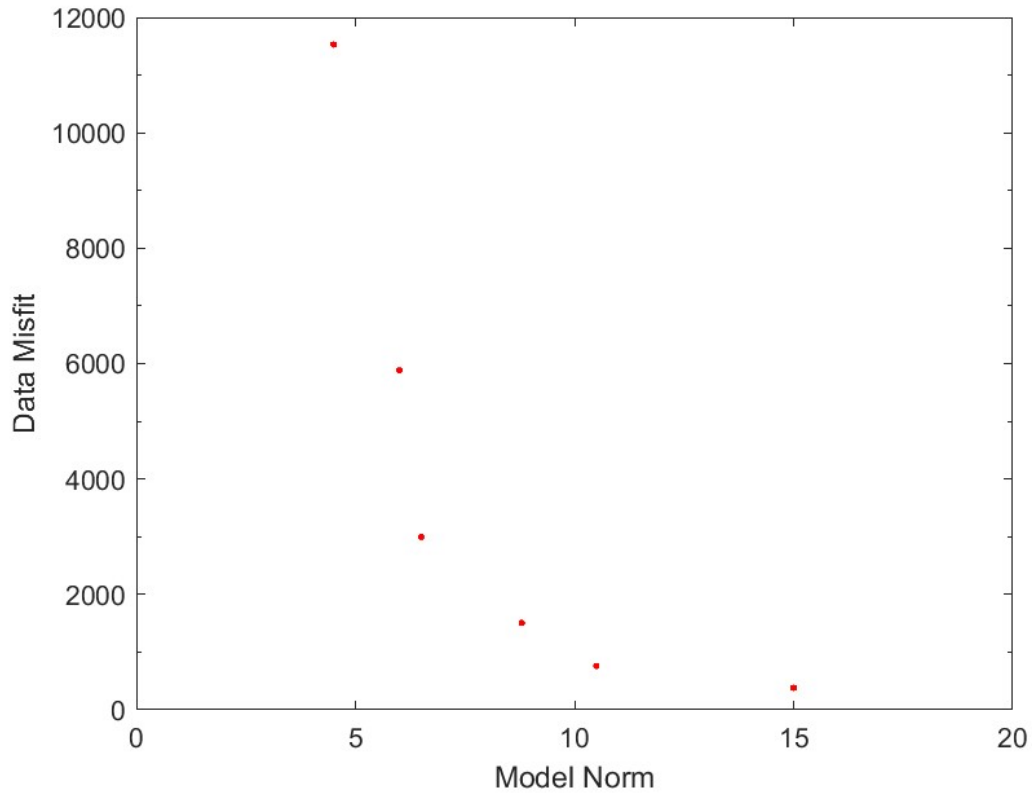

Figure D.1: Trade-off curve for the inversion of the airborne total magnetic field data for Budgell Harbour gabbro intrusion for *chifact* = 16, 8, 4, 2, 1, 0.5 (left to right).